Applications of Nonlinear Optics in 3D Direct Laser Writing and Integrated Nanophotonics

Applications of Nonlinear Optics in 3D Direct Laser Writing and Integrated Nanophotonics

A thesis presented

by

Michael Moebius

to

The John A. Paulson School of Engineering and Applied Sciences

in partial fulfillment of the requirements

for the degree of

Doctor of Philosophy

in the subject of

Applied Physics

Harvard University

Cambridge, Massachusetts

May 2016

Thesis advisor

Eric Mazur

Author

Michael Moebius

Applications of Nonlinear Optics in 3D Direct Laser Writing and Integrated Nanophotonics

Abstract

This thesis presents novel applications of nonlinear optics in laser fabrication and sources of entangled photons for quantum optics. Femtosecond direct laser writing in transparent media enables mask-less fabrication of sub-micrometer scale features with flexibility in feature shape and position in the x, y, and z-directions. Different applications in optics can be enabled by working in a variety of material platforms. We explore direct laser writing of metal structures in polymer matrices for applications in diffraction optics and modification of hydrogenated amorphous silicon (a-Si:H) for integrated optical devices. These topics explore how nonlinear optical interactions are applied to alter material properties using light. Conversely, nonlinear interactions can be used for wavelength conversion. Nonlinear interactions in nanoscale waveguides can be leveraged to produce efficient sources of entangled photons for applications in quantum optics. We explore using a novel photonic platform, titanium dioxide (TiO_2), to realize third-order spontaneous parametric down-conversion (TOSPDC) for direct generation of entangled photon triplets.

There is a need for new fabrication techniques that enable true 3D fabrication on the sub-micrometer scale. Diffraction optical elements have many potential applications in imaging, wavelength selection, and dispersion compensation. Multi-layer

diffraction optical elements could be used to integrate imaging systems on-chip for lab-on-chip devices, such as microfluidic systems. We explore using 3D laser-written metal structures in polymer matrices for 3D gratings and diffractive elements, such as zone plates and pinholes. We demonstrate diffraction from 3D gratings and imaging using zone plates.

3D fabrication of waveguides has enabled fabrication of complex optical systems within optical fibers and bulk glasses. We explore using femtosecond laser interactions with hydrogenated amorphous silicon to introduce refractive index changes. a-Si:H could be directly integrated with CMOS devices and has the potential for much higher index contrast than bulk glasses, enabling dense, multi-layer optical devices.

Efficient sources of three or more entangled photons are necessary for advances in quantum photonics. Current techniques are highly limited because they rely on cascaded second order down-conversion processes to produce entangled photon triplets and often are based in bulk optics. We leverage the high transparency, high linear refractive index, and high $\chi^{(3)}$ nonlinearity in TiO_2 to develop integrated, on-chip nano-scale waveguide sources of entangled photon triplets via TOSPDC. We present the phase-matching and nonlinear overlap conditions necessary and explore important experimental design considerations.

Contents

Citations to previously published work

Parts of this dissertation cover research reported in the following publications:

1. M. G. Moebius, K. Vora, P. A. Muñoz, S. Kang, G. Deng, & E. Mazur (2016). Direct laser writing of 3D gratings and diffraction optical structures. *manuscript under preparation.*

2. M. G. Moebius, K. Vora, S. Kang, P. A. Muñoz, G. Deng, & E. Mazur (2015). Direct Laser Writing of 3D Gratings and Diffraction Optics. *CLEO: 2015, OSA Technical Digest (online)* (Optical Society of America, 2015), paper SW1K.6.

3. M. G. Moebius & E. Mazur (2015). Femtosecond Laser Micromachining of a-Si:H In B. Di Bartolo,*Nano-Structures for Optics and Photonics* (pp. 537-538). Springer Netherlands.

4. Moebius, M. G., Herrera, F., Griesse-Nascimento, S., Reshef, O., Evans, C., Guerreschi, G. G., Aspuru-Guzik, A., & Mazur, E. (2016). Efficient photon triplet generation in integrated nanophotonic waveguides. Optics Express, 24(9), 9932-9954.

5. S. Kang, E. Mazur, M. G. Moebius, K. Vora (November 2012). Crystal growth through irradiation with short laser pulses. U.S. Patent No.: WO2014085324 A1.

6. G. Deng, S. Kang, E. Mazur, M. G. Moebius, K. Vora (December 2014). Direct laser writing of 3-D gratings and diffraction optics. U.S. Provisional Application No.: 62087097.

7. C. C. Evans, S. E. Griesse-Nascimento, E. Mazur, M. G. Moebius, O. Reshef (October 2013). Direct Entangled Triplet-Photon Sources and Methods for their Design and Fabrication. U.S. Provisional Application No. 14/529,906.

Acknowledgments

I would like to thank everyone who has supported me intellectually and emotionally throughout the past six and a half years during my PhD. I owe a great deal of gratitude and thanks to a wonderful group of co-workers, classmates, collaborators, friends, and family.

The Mazur Group has been an amazing family away from home during the course of my PhD studies. As I move on to the next steps of my career I will miss the amazing amount of community and support that members of the group provide each other. Special thanks have to go to my advisor, Eric Mazur, for being supportive of our many ideas for new research directions and providing us with encouragement to pursue projects that extended past the traditional expertise of the research group. The experience I have gained through these pursuits will be valuable throughout my career. I would like to thank Sally Seungyeon Kang, Kevin Vora, Philip Munoz, Yang Li, Shobha Shukla, and Guoliang Deng for their contributions and collaboration on laser fabrication projects. Without you these projects would not have succeeded. Orad Reshef, Sarah Griesse-Nascimento, and Christopher Evans have been part of an amazing team of peers to work with on titanium dioxide nanophotonic devices. Several visitors to the nanophotonics group greatly enriched our experience. Ausrine Bartasyte provided invaluable advice and Mei Yin brought a wealth of new project ideas during their brief visits to the group. Dario Rosenstock, Jenny Park, Kevin Mazige, and Zach Gault were wonderful students to help mentor during their projects in the group.

Many other former and current group members have provided mentorship, advice and their expertise, even when not involved directly in my projects. This will-

ingness to help and contribute to other projects helps build the vibrant research community we have the pleasure to work in. Renee Sher, Yu-Ting Lin, Paul Peng, Eric Diebold, Valeria Nuzzo, Jason Dowd, Mark Winkler, Jessica Watkins, Benjamin Franta, Kasey Philips, and Kelly Miller, thank you for being constant resources to everyone in the group. I hope to have contributed similarly to the group in the last couple years. I have had the pleasure to see Nabiha Saklayan, Alexander Raymond, Daryl Vulis, Marinna Madrid, Hemi Ghandi, and Olivia Mello join the group and become steadily more-amazing researchers. I feel confident that they will provide the same kind of mentorship and supportive environment to the next generation of incoming Mazur Group members.

I also thank my peers in the Mazur Group and the applied physics department for the comradery, especially at the start of my graduate studies. Kasey Philips and I started in the Mazur Group within a week of each other and struggled through several tough optics classes together during our first year at Harvard. Shanying Cui, AJ Kumar, Lauren Hartle, Justin Song, and I spent what seemed like endless hours on AP 282. I would not have learned nearly as much or enjoyed the coursework as much without working with such talented classmates and co-workers.

I have had the pleasure to work with an amazing and diverse group of collaborators. Prof. Alán Aspuru-Guzik, Felipe Herrera, and Gian Giaccomo-Guerreschi have helped us understand the theoretical side of quantum optics. Matthew Grein, Ryan Murphy, and Eric Dauler at MIT Lincoln Lab have invested much personal time into giving us the opportunity to conduct experiments in their lab and use equipment we would otherwise not have access to for our research. Discussions with Howard

Branz at NREL led to fascinating experiments with a-Si:H. I also greatly appreciate the time my thesis committee members, Prof. Eric Mazur, Prof. Mike Aziz, Prof. Marko Loncar, and Prof. Alán Aspuru-Guzik, have put into providing advice and feedback. The opportunity to work with and learn from such highly knowledgeable and respected members of the scientific community has left a lasting impression on me.

I could not have completed my time in graduate school without the support of friends, family, and community outside of research. My family has not only provided emotional support during stressful times, but has also often renewed my enthusiasm for my research with their curiosity about my work. Special thanks go to my ballroom dance partners on the Harvard Ballroom Team and at Firebeat Dancesport over the years who have reminded me that there is more to life than work and have made it possible for me to dance and compete in ballroom during my time in graduate school. Boston's vibrant ballroom, salsa, and bachata dance community has given me the creative and physical outlet I needed.

Acknowledgements of Financial Support This thesis is based on work funded by the Air Force Office of Scientific Research under contracts FA9550-09-1-0546-DOD35CAP and FA9550-10-1-0402-DOD35CAP, ÂňÂňthe Harvard University Center for the Environment (HUCE) Graduate Consortium fellowship, the Harvard Quantum Optics Center graduate student fellowship program, and the National Science Foundation under contract PHY-1415236.

To my family.

Chapter 1

Introduction

1.1 Overview

Since its discovery and early development, nonlinear optics has progressed significantly, enabling a large host of game-changing technologies and research. These include the nonlinear interactions that form the basis of the research presented in this dissertation. Processes related to femtosecond direct laser writing include multiphoton absorption and dielectric breakdown. Our applications in integrated nonlinear nanophotonics rely on nonlinear wavelength conversion, such as higher harmonic generation, four-wave mixing, nonlinear refractive index, and parametric down-conversion. Though these phenomena have been studied for decades, exciting new applications continue to be developed which have the potential to disrupt the norm in a variety of technological fields, ranging from 3D micro- and nano-fabrication to quantum information technology.

The aim of the research presented in this dissertation is to provide a foundation

for applications in 3D direct laser writing and quantum information technology.

1.2 Organization of this dissertation

This thesis covers two unique applications of nonlinear optics in the sciences and engineering. The first half of the thesis describes new developments in direct laser writing. The second half of the thesis focuses on integrated waveguide sources of entangled photon triplets.

Chapter 2 provides motivation for our work in direct laser writing. This includes a background of state-of-the-art fabrication methods, their limitations, and how direct laser writing seeks to overcome them. We cover physical mechanisms behind femtosecond direct laser writing. We finish by summarizing the aim of our work in direct laser writing.

Chapter 3 reports our work on direct laser writing of diffractive elements, including 3D gratings and multi-layer diffractive optical elements. We have demonstrated fabrication of gratings consisting of up to 20 layers of silver voxels in a gelatin matrix, spanning millimeters in-plane and 200 micrometers on the z-direction. We compare experimental diffraction patterns at 633 nm with diffraction patterns predicted by Laue theory. We also fabricate and test zone plates, demonstrating their dispersive properties, focusing light, and imaging. These demonstrations show significant potential for applications of laser-written diffractive elements in lab-on-a-chip devices.

Chapter 4 discusses work on direct laser modification of amorphous silicon. Hydrogenated amorphous silicon has many desirable properties for photonic devices, including transparency below the band edge of crystalline silicon, a high nonlinearity,

and CMOS compatibility. Additionally, the refractive index and band gap can be controlled by altering the hydrogen concentration, offering an index contrast as high as one. We explore altering the hydrogen content of a-Si:H as a method of altering the hydrogen content in 3D for applications in integrated 3D photonic devices.

Chapter 5 provides motivation for our work in integrated TiO_2 nanophotonics devices. The Mazur Group has pioneered the development of TiO_2 as a platform for nonlinear optics due to its high transparency for wavelengths as low as $\lambda = 400$ nm, high linear refractive index, and high $\chi^{(3)}$ nonlinearity. We now explore TiO_2 nanoscale waveguides as a source for entangled photon triplets.

Chapter 6 reports our work on the theory of generating entangled photon triplets via third-order spontaneous parametric down-conversion (TOSPDC) in nanoscale waveguides, where a single visible pump photon splits into three entangled infrared signal photons. We develop the phase matching and modal overlap conditions that must be met for high conversion efficiency, present design considerations for devices, and provide an experimental verification of the theory using the reverse nonlinear process, third-harmonic generation (THG). We present TiO_2 as one promising material platform for this application.

Chapter 7 discusses our efforts toward an experimental demonstration of TOSPDC in integrated nanoscale TiO_2 waveguides. Many important considerations impact device performance and experimental measurements of TOSPDC. We discuss methods of characterizing devices efficiently and quickly. Issues of fluorescence and detection efficiency are also taken into account when setting up measurements.

Chapter 8 summarizes the work presented and provides insights into future

directions for the research.

Appendix A describes our efforts to measure the electrical properties of laser-fabricated silver structures and provides a potential experimental plan for future work. This chapter describes some of the experimental and theoretical challenges that will need to be overcome in order to make a successful measurement of material properties.

Chapter 2

Introduction to direct laser writing

2.1 Overview

Current cutting-edge micro- and nano-fabrication techniques are either 2D processes or rely on producing layers in order to fabricate 3D structures or devices. Fast and relatively cheap processes include photolithography, which is limited in resolution to the diffraction limit of light used. Photolithography requires use of a mask, making it inflexible for rapid prototyping but more cost-effective for mass production when the mask is reused. Slower and more expensive processes include electron beam lithography, which can achieve resolution on the order of 10 nm but requires long write times for larger structures. Both processes are limited in the z-direction by alignment between stacked layers and the maximum number of layers that can be reliably fabricated on top of one another. A truly 3D process with resolution below the diffraction limit of light would revolutionize micro- and nano-fabrication [1–4].

Laser micromachining is a 3D fabrication technique that can be used to directly

write optical devices within bulk materials, such as glasses. Laser wavelengths at which glass is transparent are chosen for this application (800 nm Ti:Sapphire or frequency doubled Nd:YAG at 532 nm, for example), eliminating single-photon interactions between the laser and material. Lasers with ultra-short pulse durations (on the order of 100 fs, 100×10^{-15} s) are generally used for micromachining and direct laser writing because high peak intensities increase the impact of nonlinear interactions. A microscope objective is used to focus the beam inside the bulk of the material. At the focal point, tight light confinement combined with the short pulse duration lead to very high intensities, leading to nonlinear interactions between the laser and material. This enables introducing modifications confined to the laser focal volume in a variety of different materials for a broad range of applications in photonics [5–7]. With proper exposure conditions, features below the diffraction limit of light can be produced when only regions exposed to the most intense light at the center of the focal volume are altered. Feature sizes as small as $\lambda/20$ have been demonstrated [8]. Controlling the shape and material properties of the altered region enables applications for this technique.

Laser micromachining has several other important advantages over using stacked 2D structures. Laser writing is an inherently mask-less process, allowing rapid prototyping of different structures. Two methods are commonly used to define the shape of fabricated structures. Scanning mirrors can be used to shift the focus of the beam spot across the sample. This method introduces aberrations in the beam spot, limiting its applications in cases where feature size and resolution are critical. Alternatively, the sample is translated with respect to the laser focus. Using stage translation tends to

be slower than using scanning mirrors. By using combinations of these methods, complex 3D structures can be fabricated without requiring alignment between different fabrication steps. Features are also not restricted to the xy-plane. Lastly, direct laser writing can be used to introduce material changes into a variety of different material systems.

Micromachining in glasses is often done with the goal of altering the refractive index in order to define optical structures, such as waveguides. Multiphoton absorption leads to melting and re-solidification of the glass. For some glasses, this leads to an increase in refractive index in the laser-modified regions. Index changes in glasses are usually limited on the order of 10^{-2}. This low index contrast puts limitations on the minimum bend radii of and separation between waveguides.

Direct laser writing has also been used to produce complex, high-resolution 3D structures via multi-photon polymerization [5,8–11]. A solution of polymer monomers is exposed to femtosecond pulses, which are selectively polymerized at the focal point. The remaining monomers are washed away after fabrication. The 3D polymer structures can also be coated with metal to produce free-standing 3D metal structures on the micrometer scale. However, disconnected metal structures cannot be easily produced with this technique.

Our work presented in Chapters 3 and 4 seeks to address the limitations of fabricating disconnected metal structures in 3D and the low index contrast inherent in glass micromachining, respectively, by expanding work in direct laser writing to new material systems.

2.2 Physics of femtosecond laser micromachining

In the following section we discuss some of the basic physics involved in direct laser writing, with the goal of providing the understanding necessary to the related works presented in this dissertation. The basic mechanisms that lead to laser damage in materials will be presented, including multiphoton absorption, avalanche ionization, and thermal damage.

Several factors are critical to understanding which processes dominate in interactions between ultrafast pulses and materials. Multiphoton absorption refers to the nearly simultaneous absorption of two or more photons, which promotes an electron to the conduction band. The number of photons required for multiphoton absorption to take place depends on the wavelength of light used and the optical band gap of the material. Typical glasses have optical band gaps ranging from 3–8 eV, requiring 2–6 photons at 800 nm. Avalanche ionization or breakdown involves the acceleration of a small number of free electrons by an intense field, which produce more free electrons through interactions with bound electrons in the medium. Finally, thermal effects become more significant as the total amount of energy deposited in the medium increases or if additional energy is deposited before thermal diffusion brings the medium back to equilibrium. Multiphoton absorption and avalanche ionization depend highly on very strong fields, with intensities ranging from 10^9 – 10^{12} W/cm^2 for avalanche ionization and 10^{12} – 10^{16} W/cm^2 for multiphoton ionization [12]. Generating such high intensities often requires a tightly focus laser pulse with short pulse duration.

2.2.1 Multiphoton absorption

A medium is defined as transparent when the linear coefficient of absorption is low enough to be insignificant. In the absence of significant concentrations of impurities and defects, insufficient free carriers will be present to absorb laser energy from single photons and nonlinear photoionization will be the primary mechanism to initiate optical damage [6]. Nonlinear or multi-photon ionization refers to the direct ionization or excitation of an electron to the conduction band through nearly simultaneous interaction with multiple photons.

Two regimes of interactions exist depending on laser frequency and intensity: the tunneling ionization regime and multiphoton ionization regime. Mathematical representations of photoionization rates exist. The Keldysh equations are widely used to model these interactions and have been shown to provide a good fit to many experimental results.

At very low photon wavelengths and high laser field intensities, photoionization occurs by tunneling. Rather than photons interacting with electrons via absorption mechanisms and exciting them, the incident electromagnetic (EM) field suppresses the Coulomb well binding the valence electrons to their atoms. Fields with sufficient intensity will suppress the potential well significantly enough to greatly increase the probability of electrons tunneling into the conduction band (left section of Figure 2.1).

As the incident laser frequency is increased (while maintaining the condition $E_{\text{photon}} < E_{\text{g}}$ where E_{g} is the band gap energy of the material), multiphoton ionization becomes more prevalent. This is the condition where multiple photons are absorbed nearly simultaneously by a single electron to promote it to the conduction band

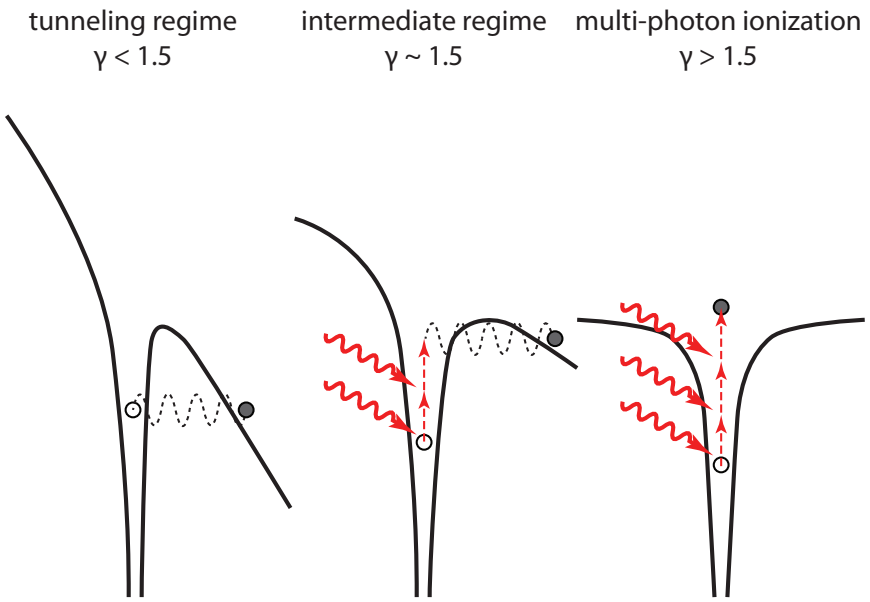

Figure 2.1: Schematic showing *(left)* tunneling ionization, *(middle)* a mixed regime with a combination of tunneling and multi-photon ionization, and *(right)* multi-photon ionization. The Keldysh parameter γ (given by Equation 2.6) can be used to estimate which effect is dominant.

(right section of Figure 2.1). The number of photons required, n, is the minimum integer that satisfies the relation $n\hbar\omega > E_g$, where ω is the frequency of the incident irradiation.

Two-photon absorption is a third order nonlinear process and is related to nonlinear index of refraction. Subsequently, higher-order photon absorption will be higher-order nonlinear processes. For the two-photon processes the nonlinear polarization is given by $P^{NL} = \epsilon_0 \chi^{(3)} E E^* E$, leading to an intensity dependence without a change in frequency as a result of the nonlinear interaction. The real portion of the third-order nonlinear susceptibility $\chi^{(3)}$ gives rise to the nonlinear refractive index, while the imaginary portion leads to two-photon absorption. Similar to the nonlinear

index, which is represented by n_2 in the equation $n = n_0 + n_2 I$, we can take into account two-photon absorption in the equation [12]:

$$\alpha = \alpha_0 + \beta I \tag{2.1}$$

β is the two-photon absorption coefficient and can be represented by the equation:

$$\beta = \frac{K\sqrt{E_p}}{n_0^2 E_\mathrm{g}^3} F_2(2\hbar\omega/E_\mathrm{g}) \tag{2.2}$$

where $E_p = 21$ eV and $K = 3.1 \times 10^3$ is determined empirically with units cm s $\mathrm{eV}^{3/2}$ (such that E_p and E_g are in eV and β is in cm/W). F_2 is the function

$$F_2(2x) = \begin{cases} \frac{(2x-1)^{3/2}}{(2x)^5} & \text{for } \ 2x > 1 \\ 0 & \text{otherwise} \end{cases} \tag{2.3}$$

We can give a general expression describing the probability or rate of multi-photon ionization. There is very strong intensity dependence, as exemplified by the rate equation:

$$P(I)_\mathrm{MPI} = \sigma_n \left(\frac{I}{\hbar\omega}\right)^n N_\mathrm{s} \tag{2.4}$$

where σ_n is the multi-photon absorption cross-section of the material, n is the number of photons involved in the process, and N_s is the density of atoms in the material. The total number of free carriers generated by multi-photon absorption is given by integrating Equation 2.4 over the pulse duration:

$$n_\mathrm{e} = N_\mathrm{s} \int_{-\inf}^{\inf} \sigma_n \left(\frac{I}{\hbar\omega}\right)^n \mathrm{d}t = \sigma_4 N_\mathrm{s} \left(\frac{I_0}{\hbar\omega}\right)^n \left(\frac{\pi}{\ln 2}\right)^{1/2} \frac{\tau}{n} \tag{2.5}$$

assuming a Gaussian pulse. Multi-photon absorption cross-sections tend to be very small. Thus high intensities are required to initiate a significant rate of multi-photon

ionization. Additionally, as more photons are required for the process, the intensity dependence becomes more significant.

The transition between the tunneling ionization and multi-photon ionization regimes (middle of Figure 2.1) can be quantified by the Keldysh parameter, γ [13,14]. Experimentally, $\gamma < 1.5$ is indicative of tunneling ionization and $\gamma > 1.5$ is indicative of multi-photon ionization. The Keldysh parameter is defined as follows:

$$\gamma = \frac{\omega}{e}\sqrt{\frac{mcn\epsilon_0 E_\mathrm{g}}{I}} \tag{2.6}$$

where ω is the incident laser frequency, e and m are the reduced charge and mass of electrons in the material, n is the material refractive index, and E_g is the material band gap. Full equations describing the rates of both tunneling ionization and multi-photon ionization can be found in Keldysh, 1965 [14].

2.2.2 Avalanche ionization

Avalanche ionization can take place if free carriers are present in the material. These free carriers can be the result of impurities, defects (particularly in crystalline materials), thermal excitation, or multi-photon ionization, as described in Section 2.2.1. Free electrons can absorb single photons with $E_\mathrm{photon} < E_\mathrm{g}$. A single electron can absorb multiple individual photons. Momentum conservation requires emission or absorption of a phonon or scattering of the electron each time a photon is absorbed [15]. After the absorption of n photons, such that $n\hbar\omega > E_\mathrm{g}$, the electron has enough excess energy that it can promote a second electron to the conduction by impact ionization (Figure 2.2). With a sufficient incident photon flux, this process repeats and sets off a cascade which doubles the number of free electrons in each

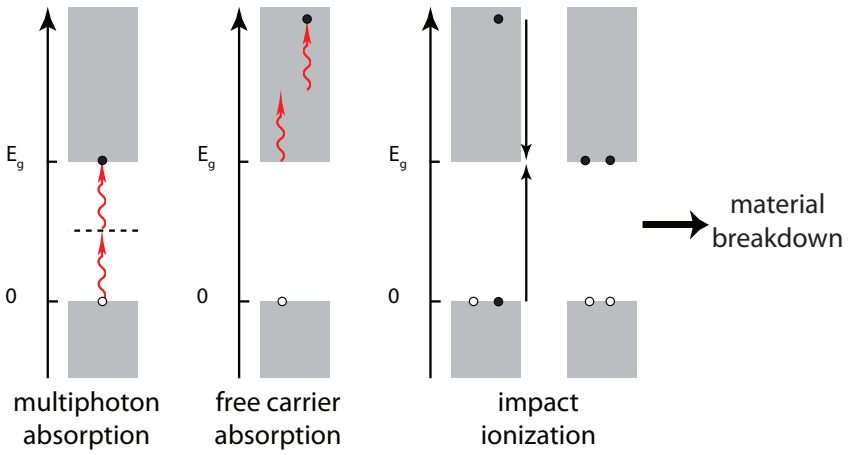

Figure 2.2: Schematic showing one process that can lead to material breakdown through avalanche ionization. Free carriers either need to be present in the material to begin with or be produced by another process, such as multiphoton ionization. Free carrier absorption then can enable impact ionization, where one electron with excess energy promotes a second electron to the conduction band. This raises the probability of further free carrier absorption and impact ionization events occurring, leading to avalanche ionization and eventual material damage with sufficient energy deposited in the material.

cycle. Some of the energy involved in the process is deposited in the material as heat, which can lead to permanent damage to the material.

The ionization rate depends on the rate at which free electrons absorb energy from incident laser pulses and the average scattering time for free electrons in the material, which determines how soon after attaining sufficient energy an electron will undergo impact ionization. A simplifying assumption made by Stuart et al 1996 [16] is that each electron in the conduction band ionizes a valence band electron as soon as it attains enough energy. As a result, no electron in the conduction band will have energy in excess of E_g until the material is fully ionized. The proposed impact

ionization rate is linear with laser intensity:

$$\nu(I) = \alpha_{\text{av}} I \tag{2.7}$$

where α_{av} is the avalanche ionization coefficient and I is the laser intensity. The rate at which the number of free electrons in the conduction band changes is given by:

$$\frac{\mathrm{d}n_{\text{e}}(t)}{dt} = \nu(I) n_{\text{e}}(t) + \left(\frac{\mathrm{d}n_{\text{e}}(t)}{\mathrm{d}t}\right)_{\text{PI}} - \left(\frac{\mathrm{d}n_{\text{e}}(t)}{\mathrm{d}t}\right)_{\text{loss}} \tag{2.8}$$

The first term accounts for avalanche ionization. The middle term accounts for photoionization (Section 2.2.1). This effect is significant at the beginning and peak of short pulses and can provide the initial seed electrons required for avalanche ionization. The last term accounts for electrons lost due to diffusion out of the laser focal volume and electron-hole recombination. These effects are insignificant for pulses shorter than 1 ps [17]. In the limit where avalanche ionization dominates in Equation 2.8, the total number of free electrons follows an exponential curve with respect to incident pulse intensity:

$$n_{\text{e}}(t) = n_0 \text{exp}\left[\int_0^{\text{inf}} \nu(I)\mathrm{d}t\right] = n_0 \text{exp}\left[\frac{\alpha_{\text{av}} I_0 \tau}{4}\sqrt{\frac{\pi}{\ln 2}}\right] \tag{2.9}$$

I_0 is the peak pulse intensity, τ is the pulse duration, and we assume a Gaussian pulse represented by $I(t) = I_0 \text{exp}\left[-4\text{exp}2t^2/\tau^2\right]$.

2.2.3 Material breakdown and damage

Two regimes for optical damage in materials exist, depending on the duration of laser pulses used to produce damage. "Long" pulses, on the order of 10 ps (10×10^{-12} s) or longer, interact with the material long enough for electrons to thermalize

and transfer heat to the lattice during the laser interaction with the material. "Short" pulses, often with durations on the order of 100 fs (100×10^{-15} s) have such a short interaction with the material that the laser pulse is no longer present when electrons thermalize and transfer energy to the lattice of atoms.

Defining the damage threshold becomes important for laser micromachining and laser fabrication methods. As a rough estimate, many optical materials will undergo permanent damage when the free electron density exceeds 10^{18} cm^{-3}. For context, many glasses have a typical initial free carrier density of 10^{8} cm^{-3} and a density on the order of 10^{22} atoms/cm^{3} [17]. Another approach to defining the damage threshold is to calculate the free electron density required to lead to efficient absorption of the laser pulse in the material. With high absorption, free electrons will have more energy to deposit into the material. We can treat the free electrons produced by multi-photon ionization and avalanche ionization as a plasma, which will absorb incident light based on the Drude model. Absorption will increase as the plasma frequency approaches the laser frequency with increasing free electron density:

$$\omega_{\mathrm{p}} = \sqrt{\frac{Ne^2}{\epsilon_0 m}} \tag{2.10}$$

where N is the free electron density and m is the mass of the electron. The absorption coefficient is then given by:

$$\kappa = \frac{\omega_{\mathrm{p}}^2 \tau}{c(1+\omega^2\tau^2} \tag{2.11}$$

where τ is the Drude scattering time (typically on the order of 0.2 fs) and ω is the laser frequency.

We can then define a skin- or absorption depth based on the absorption coefficient κ in Equation 2.11 over which the incident laser intensity will drop to $1/e$.

Absorption will be significant when the skin depth is on the same order of magnitude as the length of the focal region of the laser beam along the propagation direction. At 800 nm, the absorption depth drops to approximately 1 μm when the plasma density reaches approximately 10^{21} cm^{-3}, which is comparable to the focal length of a high numerical-aperture objective.

We can calculate the required pulse energy to produce damage in materials by using the number of free carriers generated by multi-photon ionization (Equation 2.5) and avalanche ionization (Equation 2.9) to determine the minimum pulse energy needed to reach the thresholds of free carrier density defined above. For Equation 2.9, we either use the equilibrium free carrier density or calculate the number of free carriers which can be generated by multi-photon ionization, assuming the laser pulse is intense enough. This model does assume that avalanche ionization is the dominant mechanism, which may not be true for very short, intense pulses.

It is also worth noting that the damage threshold varies depending on the location on the sample. Surface damage requires roughly one-half the energy of bulk material damage. In the bulk, all atoms and molecules will form bonds with all surrounding atoms or molecules. These bonds must be broken in order to melt, crack, or ablate the material. Surface atoms and molecules have some dangling bonds and thus less energy is required to produce damage. Some materials, notably ones that can be produced as crystals with very low defect and impurity concentrations such as silicon, have a much greater disparity in damage threshold between the bulk and surface because contaminants on the surface can greatly reduce the damage threshold. These factors must be taken into consideration when choosing laser exposure

parameters for applications and can impose a minimum depth at which bulk damage can be produced while avoiding surface modification.

Long pulses interact with the material long enough to allow for excited carriers to transfer energy to the material lattice during the laser interaction. In some cases, the pulse will still be interacting with the material as ablation and thermal diffusion take place. Because I wide variety of processes occur in the material during the laser interaction, long pulse interactions can be harder to control. Often ablation will occur once the pulse energy is above the damage threshold. Additionally, because heat diffusion occurs within the pulse duration, damage spots cannot be limited to the focal volume of the laser, giving much less spatial control of laser machining or fabrication processes.

Determining the damage threshold also becomes more complicated. Thermal diffusion leads to loss of heat to the surrounding material during the laser interaction. Direct nonlinear photoionization becomes less significant because long pulses may not reach the required high intensities. Avalanche ionization becomes the dominant factor because many cycles of impact ionization can take place, greatly increasing the number of free carriers. However, this process does require the presence of free carriers to be initiated. As a result, the damage threshold can vary greatly across a sample because low defect concentrations may lead to less than a single free carrier on average being present within the laser focal volume. For example, a focal spot with a radius of 1 μm and confocal parameter of approximately 2 μm has a volume of only approximately 10^{-11} cm^3. With a defect concentration of 10^{11} cm^{-3}, this would lead to an average of only one defect per focal volume. Variations in defect concentrations

across the material will thus lead to variations in damage threshold.

As pulse duration is decreased, the damage threshold decrease with the relationship $\sqrt{\tau}$, where τ is the pulse duration. This trend becomes flat for pulse durations below approximately 10 ps [18, 19].

In the short pulse duration regime, the laser-material interaction and processes such as thermalization, ablation, and thermal diffusion become decoupled. This means that electrons become excited and the laser pulse deposits energy into the electron plasma. After the laser pulse has ended its interaction, the electron plasma deposits energy into the material lattice. The energy is thus transferred from the electrons to the lattice within a very small time frame and in a limited volume within the material. Material changes can thus be limited to regions smaller than the focal volume of the laser because the strong intensity dependence of multiphoton ionization processes can be exploited.

In this regime, intensities are high enough that multiphoton ionization can seed avalanche ionization. However, due to the short pulse duration, the impact of multiphoton ionization becomes more significant relative to avalanche ionization because fewer impact ionization cycles can take place within shorter pulse durations.

We can consider several important factors in short pulse interactions with materials. The mechanisms which produce optical damage no longer depend on the presence of intrinsic or thermally excited free carriers. Multiphoton ionization seeds free electrons necessary for avalanche ionization. Damage thresholds are thus generally more deterministic and consistent across a sample. Short pulses also produce very high intensities with relatively low pulse energies. Material damage can be pro-

duced without leading to thermal damage in the surrounding material. Material modification can thus be controlled more easily than in the long pulse regime.

The numerical aperture of the objective used for laser micromachining can also impact the material modification produced. High numerical apertures produce a smaller focal volume in plane and along the propagation direction of the incident light. This can be exploited to greatly increase the maximum intensities produced and reduce the necessary pulse energies for material modification. Additionally, the morphology of the damage spot produced by the laser interaction is highly influenced by the numerical aperture (NA) of the focusing objective (Figure 2.3 [20]). High-

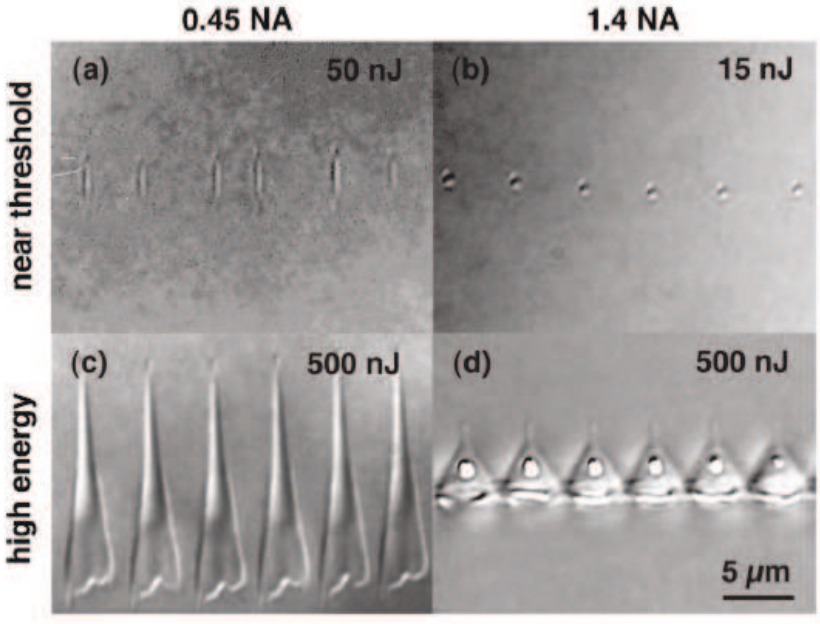

Figure 2.3: Images of damage spots produced by a single 110-fs laser pulse. Low pulse energies lead to damage localized within the focal volume of the laser. High pulse energies lead to larger damage spots due to thermal effects. As the numerical aperture of the focusing objective is increased, the length of the damage spot along the propagation direction of incident light is reduced. This figure is from Schaffer et al. 2004 [20].

NA objectives lead to less elongated damage spots. This can be explained by the shape of the focal volume. The minimum beam radius at the focus is given by $w_{0\text{min}} = 1.22\lambda/nNA$ where n is the refractive index of the material the objective is immersed in (1 for air and typically between 1.3–1.5 for oil immersion). The length of the focal volume is determined by the Rayleigh parameter $Z_{\text{R}} = \pi w_{0min}^2 n/\lambda$ (the confocal parameter is twice the Rayleigh parameter). The Rayleigh parameter give the distance from the focus at which the beam radius has increased by a factor $\sqrt{2}$. These parameters show that an elongated focal spot and damage spot are expected when using a low-NA objective to focus the incident laser pulses.

Laser repetition rate is one additional factor that can be taken into account for laser damage. For repetition rates below approximately 1 MHz, thermal diffusion brings the material back to equilibrium in between successive incident pulses. Higher repetition rates, however, lead to a condition where heat accumulates within the focal volume and the temperature of the material does not drop to the equilibrium value before additional pulses are incident on the material. In this regime, the damage threshold of the material can be further reduced due to thermal effects. Additionally, features produced by laser writing tend to become larger as more pulses are incident on the sample due to thermal effects impacting regions outside the laser focus.

The factors described in this section can be used to understand the laser-material interactions at play in material modifications described in the following two sections and chapters of this dissertation.

2.3 Direct laser writing of metal structures in a polymer matrix

Challenges in fabricating disconnected metal structures in 3D has been one of the major roadblocks in fabrication for structures such as metamaterials or 3D gratings and other diffractive elements on the nano- and micro-meter scale [1–4]. Other researches have addressed these challenges by coating laser-written 3D polymer structures with metal [21–24] and back-filling metal voids with metal [25]. These advances have been enabled by advances in micro- and nano-scale fabrication of polymer structures by direct laser writing [5, 8–11]. The Mazur Group has pioneered a fabrication method which addresses the limitation of fabricating 3D metal structures directly by enabling direct laser writing of metal structures within a polymer matrix [26–28]. Following fabrication, the polymer matrix is left in place, providing a transparent dielectric matrix for the metal structures. This provides added benefit of enabling the fabrication of disconnected metal structures. Many applications in metamaterials and diffractive optics require nano- and micro-scale metal structures in a transparent dielectric medium.

Sample preparation consists of several simple steps. A polymer, solvent, and metal salt are mixed. This solution can be drop cast or spin-coated on a substrate. The sample is cured in order to ensure that the polymer layer solidifies before laser fabrication. Our work has focused on systems involving silver nitrate in PVP or gelatin. Following sample preparation, silver structures are fabricated by focusing a femtosecond laser within the bulk of the polymer matrix. Pulsed lasers with wave-

lengths centered at 525, 780, and 1050 nm, repetition rates ranging from 11–80 MHz, and pulse durations ranging from 60–270 fs have been successfully used for fabrication. Typical pulse energies range from 0.1–20 nJ.

The complete mechanism of silver structure formation is not yet understood for this fabrication technique. Unlike laser micromachining in glasses, the goal is not to reach a threshold where the material in the focal volume is melted or damaged. Instead, electrons must be liberated within the polymer matrix so that the silver ions in solution can be reduced to form solid silver structures. To the best of our current understanding there are several mechanisms that can mediate this process. The first pulses incident on the sample must generate free electrons via multi-photon absorption. It is possible that other processes, such as avalanche ionization aid in producing additional free electrons before interacting with silver ions in solution. Although it is expected that functional groups in the polymer matrix may be providing electrons for the formation of silver structures through a chemical reaction, evidence of the resulting byproducts has not been found. The polymer matrix and its functional groups may still act as a catalyst for the formation of silver structures [29]. Once silver structures have begun forming, linear absorption and thermal effects are likely to influence further growth of silver structures. The lasers used for fabrication have sufficiently high repetition rates (11 and 80 MHz) to cause thermal buildup in the focal region.

Unanswered questions include on which time scale silver structures begin to form and on which time linear absorption and thermal effects begin impacting silver growth. Answering these questions would require further studies, including pump-

probe spectroscopy during laser fabrication.

Different chemistries have advantages for a variety of applications. The polymer used determines the range of wavelengths over which the final device is transparent. PVP has transparency in the range of approximately 0.4–2.5 μm and 3.5–5.5 μm while gelatin is transparent from 0.4–1.1 μm and around 1 THz [29]. Under specific laser exposure conditions and sample chemistries using PVP as the polymer matrix, we have observed the growth of single crystal silver structures. These structures could have applications in plasmonics. Direct laser writing offers advantages in rapid growth of single crystal silver structures compared to using solution chemistry and enables exact placement of the structures on a substrate [30]. Direct laser writing of silver structures in gelatin has yielded far superior feature size and resolution compared to silver structures in PVP, with minimum feature sizes below 100 nm [31]. Additionally, greater stability of the gelatin matrix over long time makes this platform preferable for 3D device applications. Chapter 3 will provide details on our recent work on direct laser writing of diffractive elements.

2.4 Femtosecond laser modification of hydrogenated amorphous silicon

Low index contrast (typically on the order of 10^{-2}) and compatibility of the platform put limitations on direct laser writing of optical devices in glasses. Index contrast determines confinement of the guiding mode in a waveguide. This impacts the minimum waveguide size while ensuring that there is a guiding mode at the

operating wavelength as well as the minimum band radius while avoiding significant losses. These factors impact device design because they determine the device density that can be achieved within a given area or volume, in the case of 3D devices. In modern technology, space is becoming more and more of a premium and thus dense device architecture is desirable.

In terms of compatibility, many devices rely on a silicon platform. Therefore, optical materials that can be integrated with a silicon platform are advantageous. This has led to a focus on silicon photonics. Direct laser writing in crystalline silicon is, however, challenging due to the high pulse energy required for damage in the bulk, low refractive index changes, and the sign of the refractive index change [32].

Hydrogenated amorphous silicon (a-Si:H) has a highly variable refractive index based on the hydrogen content [33, 34]. High index contrast waveguides can therefore be defined in a-Si:H by controlling the hydrogen content [35–37]. Films can be deposited at low temperatures which are CMOS compatible. Due to the high index of a-Si:H (2.5–3.5) and high index contrast possible for waveguides, very high light confinement could be achieved. Therefore device architecture would only require a thin (several 100 nm) SiO_2 cladding layer between an underlying silicon platform and a-Si:H layer to achieve low-loss waveguides. Due to these promising characteristics, we study laser modification of a-Si:H to control the hydrogen content and refractive index as a method of producing 2D and 3D optical devices. This work is discussed in more detail in Chapter 4.

Chapter 3

Direct laser writing of 3D gratings and diffraction optical structures

3.1 Preface

The following chapter contains material presented in the manuscript: Michael Moebius, Kevin Vora, Philip Muñoz, SeungYeon Kang, Guoliang Deng, and Eric Mazur, "Direct laser writing of 3D gratings and diffraction optical structures," *manuscript under preparation*, 2016.

3.2 Abstract

We fabricate 3D gratings and multi-layer diffraction optical elements consisting of disconnected silver structures in a gelatin matrix using a direct laser writing technique. 3D gratings achieve approximately 5% efficiency at 633 nm and experimental

diffraction patterns show good agreement with Laue diffraction theory. Zone plates are used to demonstrate imaging as well as wavelength selection in the visible. These demonstrations show that 3D direct laser writing of metal structures is promising for fabrication of vertically-integrated diffraction optics and lab-on-a-chip applications.

3.3 Introduction

Integrated diffractive optical elements have many applications, including beam shaping and control on the micrometer scale, imaging [38], improving high numerical aperture systems [39], dispersion-based devices [40], and maskless lithography [41]. 3D gratings allow manipulation of incident beams cannot be achieved using single-layer or 2D structures. Diffractive elements are becoming prevalent in cutting-edge macro-scale optical devices. Diffractive elements have the added advantage of functioning at a wider range of wavelengths than refractive elements.

Diffractive techniques have been used widely to investigate material properties. Similar to x-ray and electron diffraction from atomic lattices, Bragg scattering from optical scatterers exposed to light can be used to investigate the quality of photonic crystals [42–48]. This has been extended to 3D structures fabricated by two-photon polymerization (TPP) [49]. These structures can be used to create 3D optical diffraction devices in the high-energy regime, where the lattice constant is greater than the incident wavelength [45, 50, 51]. TPP cannot produce disconnected structures in 3D, limiting complexity. Since these structures must also support their own weight, large filling fractions are often necessary.

In the field of diffractive optical elements, multi-layer devices are desirable be-

cause this enables greater device complexity. Multi-layer fabrication will enable on-chip integrated imaging applications on the micrometer scale. These capabilities would be particularly useful for lab-on-a-chip applications [52,53]. Previous work has shown zone plates used for on-chip optical trapping [54] and fabrication on flexible substrates has also been shown to improve field of view and have applications in focus scanning [55]. Fabrication of multi-layer structures has been limited. Phase zone plates have been demonstrated in 3D within bulk glasses via femtosecond laser micromachining [56]. This requires exposure to high laser power. For CMOS integration, this would additionally require deposition or bonding of a thick glass layer. Other approaches to multi-layer structures require layer-by-layer lithographic fabrication. This requires multiple expensive cleanroom fabrication steps and individual layers and features are restricted to 2D.

We use a novel 3D laser fabrication technique that overcomes the limitations of TPP and layer-by-layer lithographic fabrication techniques to produce 3D metal structures [26]. We fabricate samples by focusing laser pulses within the bulk of a polymer layer doped with metal salts. Exposure to the laser pulses leads to growth of metal structures at the focal point. The process is initiated by multi-photon absorption, enabling sub-diffraction limited feature sizes. Minimum feature sizes of $< \lambda/8$ and diffraction-limited resolution have been achieved using a 0.8-NA objective [31]. Because the polymer layer is left in place after fabrication, disconnected metal structures of arbitrary shape and orientation can be written. Low laser powers can be used for fabrication, making scalability with parallel fabrication feasible. As with other direct laser writing techniques, this technique enables rapid prototyping of structures

without the need for masks or cleanroom use.

Direct laser writing of metal structures has been proposed as a fabrication method for a variety of different applications, including 3D circuits and metamaterials [1–4]. Rapid growth of single crystal silver structures has also been demonstrated [30]. We now show that this same technique can be used to fabricate 3D gratings and diffractive optical elements for operation at visible wavelengths. In this paper we present experimental diffraction patterns from laser-written 3D gratings and compare them to theoretical diffraction patterns. We then present the first results for laser-written diffractive optical elements and multi-layer diffractive optical elements. These results show that this fabrication technique has many potential applications for on-chip integrated imaging and beam control.

3.4 Fabrication methods

In this section we discuss details related to the sample fabrication methods.

Fabrication using this metal direct laser writing technique requires only two steps: sample preparation and laser exposure [27, 28]. The same sample preparation procedure is used for 3D gratings and diffractive optical elements. Laser-writing parameters are selected to optimize fabrication of different types of structures. In the following section we describe the sample preparation procedure and fabrication setup, laser exposure parameters, and sample test procedure for 3D gratings and diffractive optical elements.

We complete fabrication in approximately 200-μm thick gelatin films doped with silver nitrate. 800 mg of gelatin is dissolved in 4 mL of de-ionized water heated to

50 °C using a vortex mixer. Once gelatin is fully dissolved, 105 mg of $AgNO_3$ is added and fully dissolved. 1 mL of this mixture is drop-cast on a 25 by 25-mm glass slide. After setting for 12–24 hours this forms a 200-μm thick gelatin film. Further information about this chemistry is provided in [29,31]. The choice of polymer matrix determines the operable range of wavelengths of the device, based on the transparency window of the polymer.

We use the same setup to fabricate both 3D gratings and diffractive optical elements (Figure 3.1. An acousto-optic modulator (AOM) is used to determine the exposure time for each region of the sample, as well as turn the beam on and off for disconnected structures. The AOM can be modulated at up to 5 MHz, allowing a minimum on/off cycle of 100 nanoseconds. A half wave plate and polarizer control the pulse energy. We focus the beam into the sample using a 0.8-NA objective with 3-mm working distance. A long-travel, high-precision 3D translation stage moves the sample with respect to the laser focus, controlling where it is exposed. The stage and AOM are computer controlled, enabling fabrication of complex 3D patterns. The laser exposure parameters vary between the 3D gratings and diffractive optical elements.

We fabricate 3D grating samples by focusing 66-fs pulses from an 11-MHz repetition rate Ti:sapphire laser centered at 795 nm into the polymer layer. Analogs of atomic lattices are fabricated (simple cubic, body-centered cubic with single- and two-atom bases, and hexagonal lattices). We use an average laser power of 5–50 mW with exposure times of 0.1–1 millisecond per voxel, producing voxels ranging from $<$100 nm to 5 μm in size. The voxel size determines the scattering strength. Both the dose used during laser exposure and the fabrication depth below the polymer surface

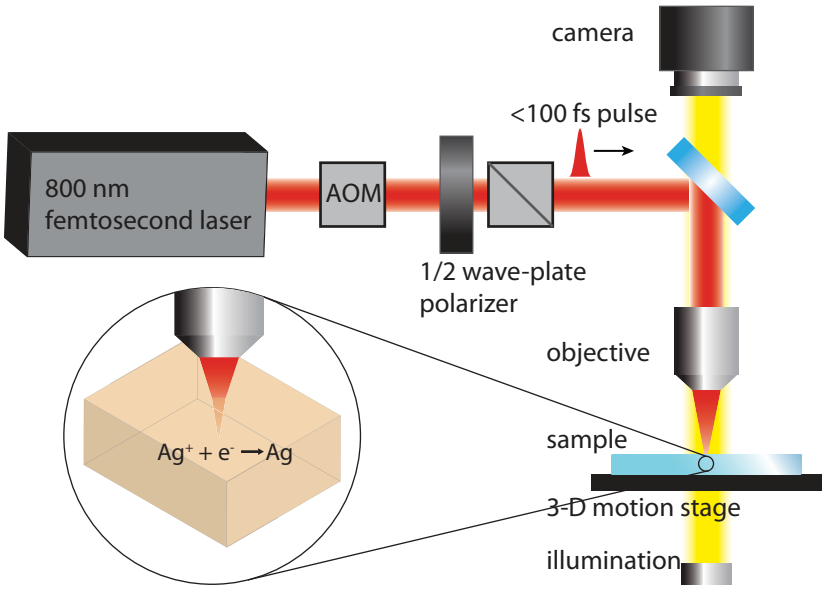

Figure 3.1: Schematic of the laser fabrication setup used to produce 3D metal structures in a polymer matrix. The output from a femtosecond laser in the near infrared is sent through an acousto-optic modulator (AOM), which allows precise control of when laser pulses are incident on the sample. A half-wave plate and polarizer are used to precisely control the laser power and polarization incident on the sample. A dichroic mirror is used to direct the beam through the microscope objective which focuses the femtosecond pulses on the sample. The 3-axis translation stage holding the sample is used to move the sample with respect to the laser focus, allowing precise control of where the sample is exposed to laser pulses. The AOM and 3-axis stage are synchronized and computer controlled. A light source and camera enable in-situ imaging of the sample during fabrication.

impact the voxel size, with features fabricated deeper within the polymer requiring higher exposure. Voxels are spaced by 5–40 μm in the x, y, and z-directions in order to observe multiple diffraction orders within a ± 45 degree arc when illuminating the sample with visible wavelengths. Samples span several millimeters in the x-y plane and consist of 2–12 layers in the z-direction.

We fabricate diffractive optical elements by focusing 90-fs pulses from an 80-MHz repetition rate fiber laser centered at 780 nm into the polymer layers. Zone plates

with focal lengths ranging from 4 to 50 μm at 633 nm and pinholes are fabricated. We use an average laser power of 3–15 mW and stage translation speed of 5–200 μm/s. Depth of the features below the surface of the polymer and laser exposure parameters determine the opacity, minimum feature size, and resolution of the silver structures produced. Higher exposure power produces more opaque features, but overexposure negatively impacts minimum feature size and resolution. Zone plates are also fabricated using electron beam lithography to pattern an aluminum mask in order to compare performance between lithographic and laser-written zone plates. Multi-layer structures consisting of a zone plate and pinhole fabricated by direct laser writing are also demonstrated.

3.5 3D gratings

In this section we will discuss experiments related to 3D gratings. These initial experimental efforts were aimed at demonstrating that our direct laser writing technique can be used for fabricating function 3D diffractive optical elements.

We measure experimental diffraction patterns from the fabricated 3D gratings to compare to calculated diffraction patterns based on Laue theory. Diffraction patterns are measured in transmission (Figure 3.2). A 633-nm HeNe laser is used to illuminate the sample with a beam spot approximately 0.5 mm in diameter. This spot size ensures that we illuminate at least 10 unit cells in the x and y-directions, while keeping a spot size smaller than the extent of the sample. A low laser exposure power of < 1 mW is used to avoid damage to the sample under continuous exposure. The sample is mounted on a rotation stage, allowing illumination in a range of ± 60 degrees

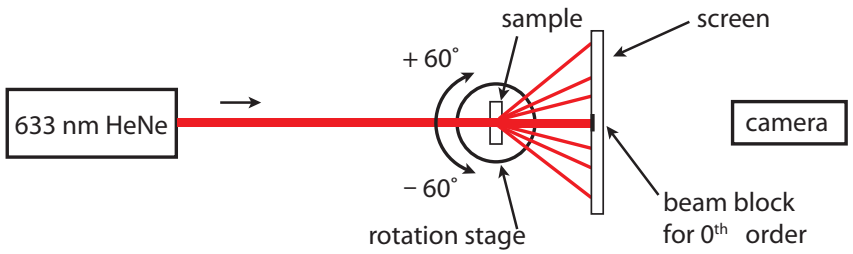

Figure 3.2: Schematic of the setup used to measure transmission diffraction patterns. A 633-nm HeNe laser is passed through the sample, which sits on a rotation stage, allowing rotation of the sample with respect to the incident beam. The transmitted light is projected on a screen, which enables imaging of the diffraction pattern. A beam block is used to remove the 0^{th} order transmitted beam to prevent it from overexposing the image of the diffraction pattern.

relative to the sample normal. The diffraction pattern is projected onto a screen with a beam block to remove the 0^{th} order transmitted beam. We image the diffraction pattern on the back surface of the screen. We are able to image diffracted beams at angles as large as 4°.

We estimate grating efficiency using image analysis to integrate the intensity of all diffracted beams within the field of view. Results from image analysis are compared to direct measurements of the incident and transmitted power through the sample and direct measurements of individual diffracted beams using a hand-held power meter. Due to the number of diffracted beams, direct measurements of all diffracted beams are not practical for measurement of the total grating efficiency, but can still provide verification for the image analysis techniques. We estimate a grating efficiency of 1–5% for gratings at normal incidence and 2–10% with the sample angled relative to the incident laser beam.

We use measurements from a 10-layer simple cubic grating to compare exper-

imental and theoretical results of 3D gratings due to the quality and uniformity of the voxels in the grating and the measured diffraction patterns. Figure 3.3 shows a schematic of the simple cubic 3D diffraction grating and a single unit cell. An optical image of a single layer of a 10-layer simple cubic grating is shown in Figure 3.3. The

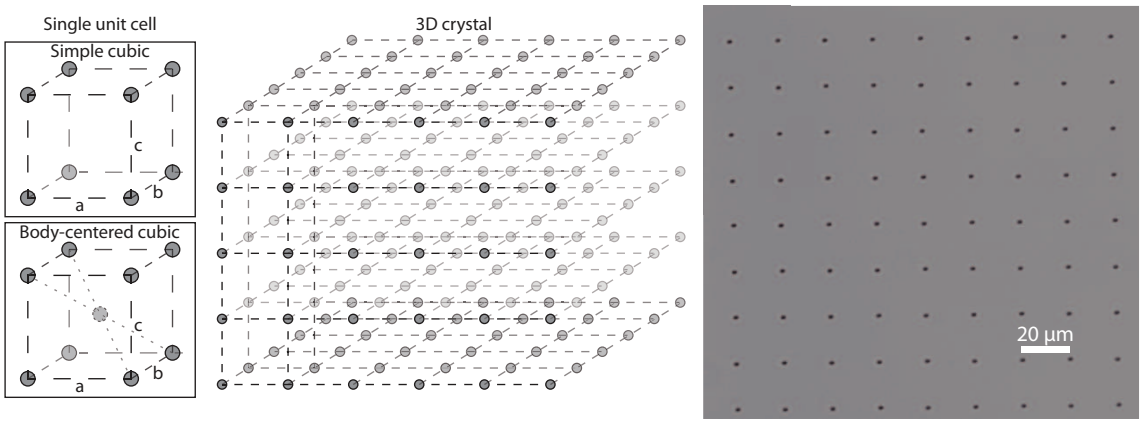

Figure 3.3: (*left*) Schematic of a single simple cubic and body-centered cubic unit cell. (*middle*) Schematic of a 3D simple cubic grating with multiple layers. (*right*) Optical image of a single layer of a simple cubic grating with 20 μm unit cell size.

spacing in the x, y, and z-directions is 20 μm with a voxel size of approximately 1 $\times$ 2 μm (elongated in the z-direction). Diffraction patterns for this grating are shown in Figure 3.4 at a beam incidence angle of 0° (normal incidence), 20°, and 40°.

Experimental results from 3D diffraction gratings are in good agreement with Laue theory and calculated diffraction patterns. Locations of diffraction maxima match expectations based on Laue diffraction theory. Intensity variations due to diffraction orders resulting from a multi-layer structure are close to expectations based on theory, however, bands from each diffraction order are wider than calculations predict for a given number of layers in the beam propagation direction. Figure 3.4

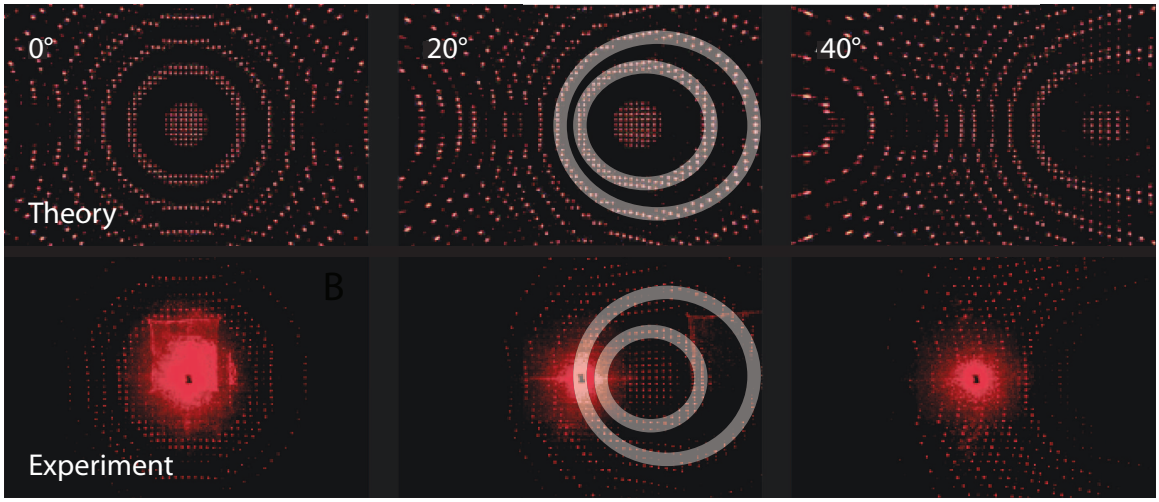

Figure 3.4: Comparison between the calculated diffraction pattern from a 4-layer simple cubic structure and measured diffraction patterns from a 10-layer simple cubic structure with the sample at 0°, 20°, and 40° relative to the incident irradiation. The positions of diffraction maxima in the experimental demonstration match well with theory. However, individual diffraction orders are wider than expected. Two diffraction orders have been highlighted in the 20° case for comparison between theory and experiment.

compares experimental results of the 10-layer simple cubic lattice with theoretical results for a 4-layer simple cubic lattice, showing the discrepancy between expected and observed width of diffraction orders. Additionally, diffraction patterns from 3D gratings containing a basis of two voxels of different sizes exhibit weak signals at some forbidden reciprocal lattice points Figure 3.5.

Differences between ideal point scatterers and the fabricated structures can account for some of these discrepancies. Shadowing effects due to large absorption and scattering cross sections may be the cause of experimental results from 3D gratings matching theory for gratings with a lower number of layers. Significant absorption in the upper layers of the grating would reduce the amount of incident light on the lower layers. This effect is noticeable for experimental results from gratings consisting

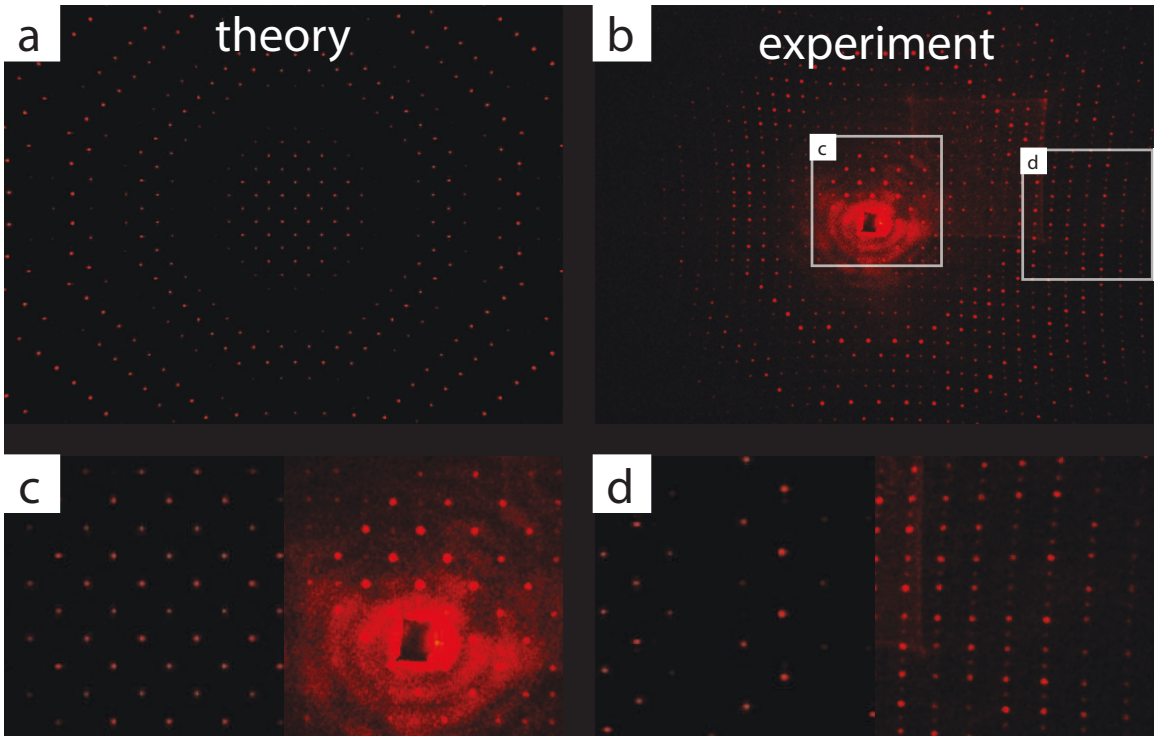

Figure 3.5: Comparison between the (a) calculated and (b) experimental diffraction patterns from a body-centered cubic 3D grating with 20-μm unit cell size. Panel (c) shows a zoom-in of the low angle, first-order diffraction maxima. There is good agreement between theory and experiment in this area. Panel (d) shows a zoom-in of higher-angle, higher-order diffraction maxima. Not only do we observe weak signal at forbidden diffraction points, but we also see an extra set of points with weak signal along the vertical direction which are not at expected locations based on the symmetry and lattice size of the grating.

of more than 4 layers along the illumination direction. As the effective number of layers in a 3D grating decreases, the bands for each diffraction order become wider (see Section 3.8).

We use a commercial finite difference time domain (FDTD) solver to investigate the differences in the scattered field produced by ideal, small spherical scatterers and larger, realistic scatterers that we fabricate by direct laser writing. We explore the

impact of non-ideal scatterers by running calculations of the scattering properties of different size and aspect ratio voxels in different orientations with respect to the incident irradiation. Figure 3.6 shows the near-field scattering from a small spherical particle and large elliptical particle. These results show that a small spherical particle

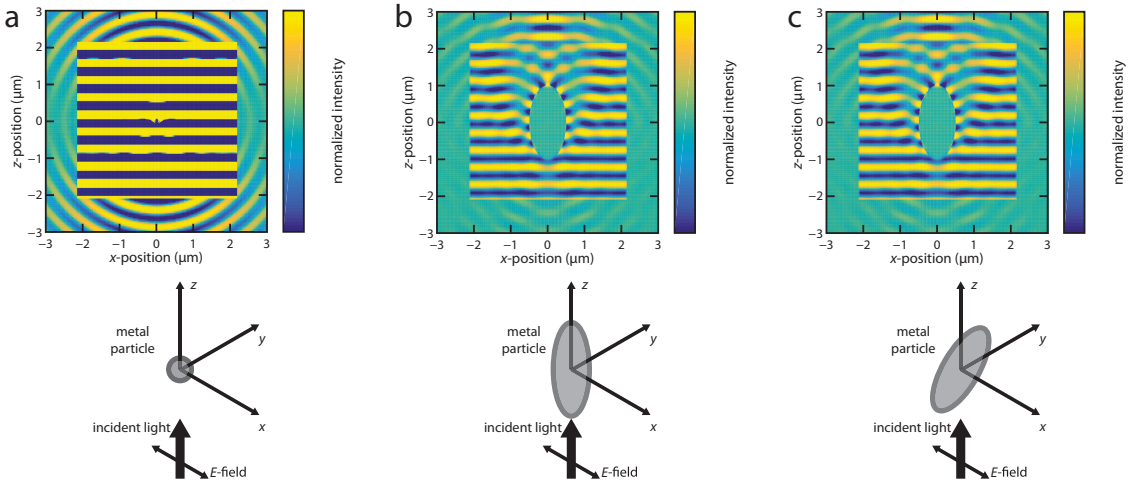

Figure 3.6: Plots of the near field scattering in the xz-plane from (a) a 50-nm spherical particle, (b) a 1×2-μm ellipsoidal particle, and (c) a 1×2-μm ellipsoidal particle angled at 45° toward the y-axis (rotated about the x-axis. Incident irradiation is along the z-axis at 633 nm, with the E-field polarized along the x-axis. The field intensity is amplified by 50× in (a) because the scattered intensity is much lower for this small particle size. We see greater directionality in the scattering from the large, elliptical particles.

will scatter like an ideal dipole, which would lead to diffraction patterns as predicted by Laue theory. Scattering from the ellipsoidal particles is much more directional, with the greatest intensity along the incident direction.

Near-field scattering patterns are helpful for understanding the differences in behavior, but we need to look at the far-field scattering to understand the diffraction patterns. We also want to understand if particle size or aspect ratio has a stronger impact on the scattering properties. Figure 3.7 shows the far-field scattering pattern

from different size spherical particles. This figure gives the far-field pattern in the

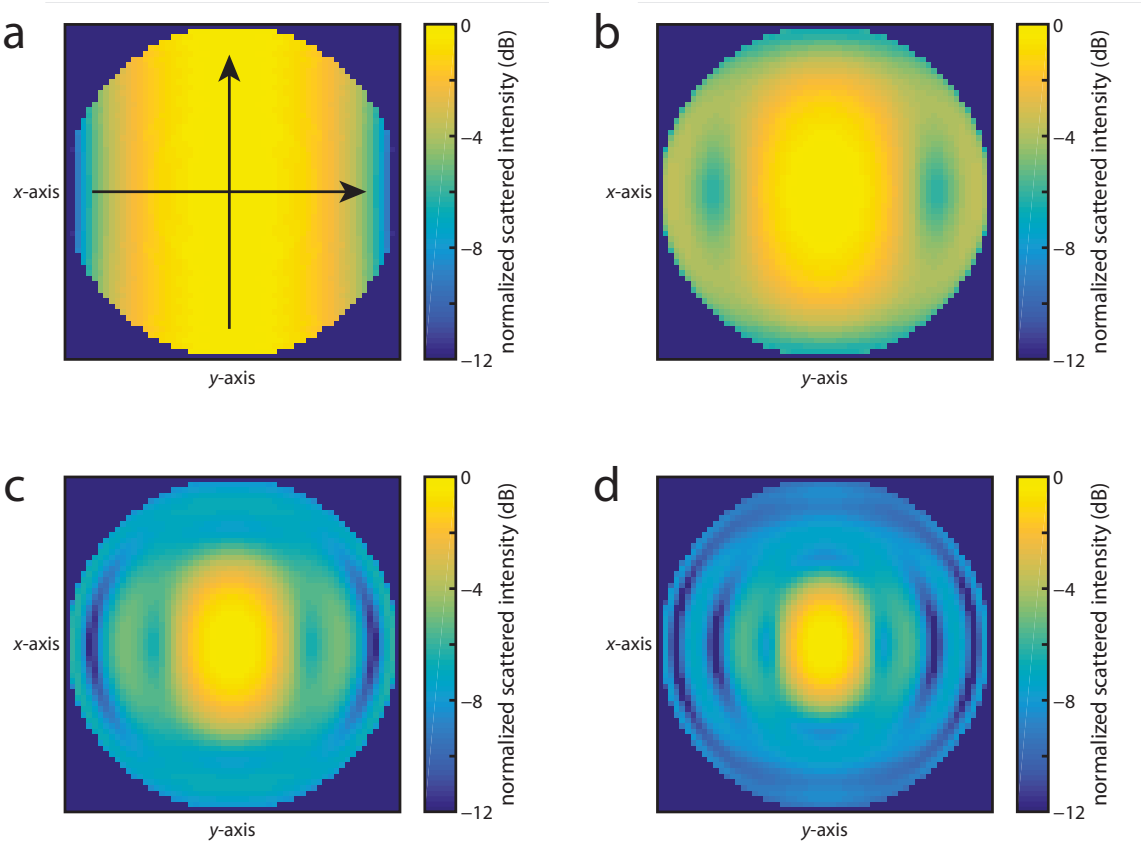

Figure 3.7: Far field scattering pattern from (a) a 50-nm sphere, (b) a 400-nm sphere, (c) a 700-nm sphere, and (d) a 1000-nm diameter sphere. The far field pattern on the hemisphere above the xy-plane is collapsed into 2D. The E-field is polarized along the x-axis. The x-axis runs in the horizontal direction and the y-axis in the vertical direction. The 50-nm sphere exhibits the scattering characteristics of a dipole, while directionality of scattering along the incident light direction and the prevalence of side lobes along the field polarization become more pronounced for larger particles.

hemisphere above the xy-plane collapsed to 2D. We observe increasing directionality and prevalence of lobes along the x-axis as particle size increases. We also calculate the far-field scattering produced by ellipsoidal particles at various orientations with respect to the incident light (Figure 3.8). We find that the side lobes in the far-field

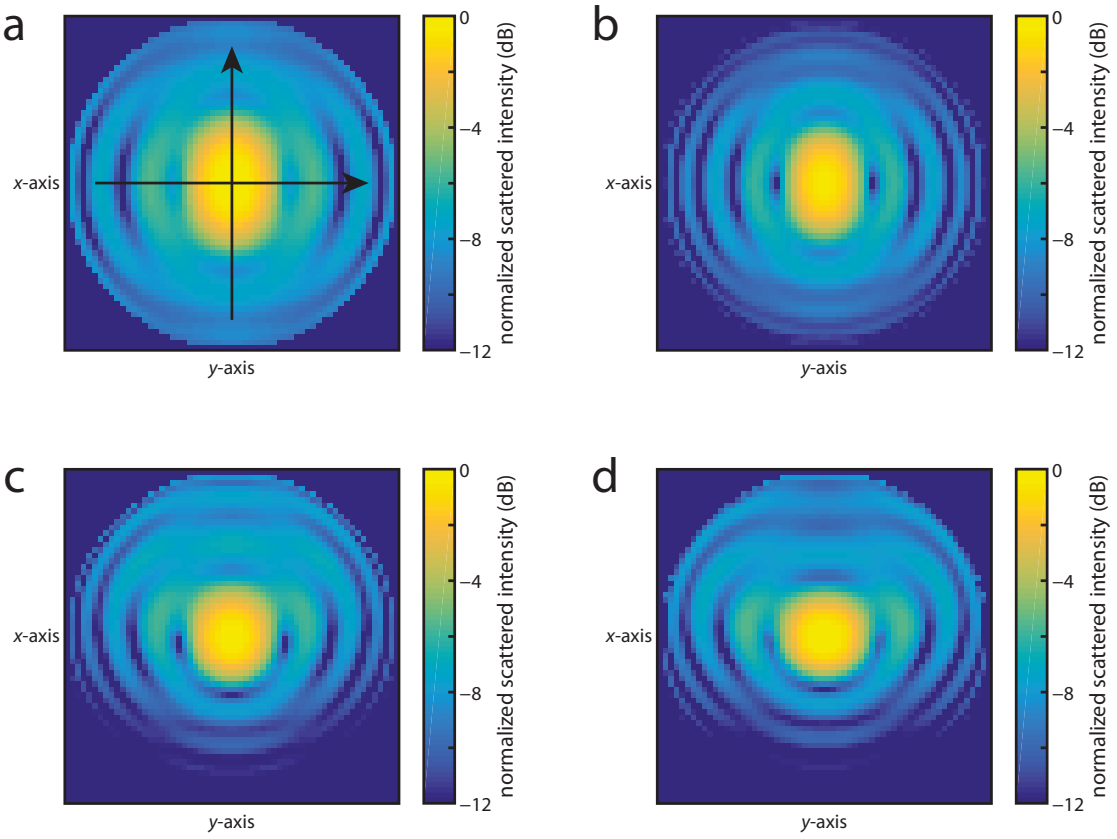

Figure 3.8: Far-field scattering for (a) a 1 μm sphere, (b) a 1×2 μm ellipsoidal particle aligned along the z-direction, (c) an ellipsoidal particle tilted at 30° toward the y-axis, and (d) an ellipsoidal particle tilted at 45° toward the y-axis. Elongating the particle leads to additional directionality and more prevalent side lobes in the far field pattern. Tilting the particle with respect to the incident light shifts the position and shape of these side lobes.

pattern shift along the direction of the particle tilt. We also extract scattering and absorption cross sections from these simulations. These calculated far-field scattering patterns can be used to improve predictions of the diffraction pattern.

For the 1×2-μm ellipsoidal particle, we find a scattering cross section $\rho_{\text{sc}} = 3 \times 10^{-12}$ m^2 and absorption cross section of $\rho_{\text{abs}} = 8 \times 10^{-13}$ m^2 at 600 nm for a particle with a physical cross sectional area $\rho = 8 \times 10^{-13}$. The scattering and

absorption cross sections are close to constant, regardless of particle angle with respect to the incident light. These results provide insights about the impact of particle size, shape, and orientation on the scattering properties. For a 20-μm unit cell size, this corresponds to scattering approximately 1% of incident light, which suggests that multiple scattering events should not be significant in our samples and is on the same order of magnitude as the scattering intensity we measure from our samples experimentally.

Fabrication variations also play a role in the quality of diffraction gratings and the resulting diffraction patterns. Variations in laser output power, irregularities in the silver content across the sample, and variations in polymer thickness across the sample result in variations of voxel size. We typically observe variations in power form our Ti:sapphire laser of $\pm 10\%$ at the objective during fabrication, which leads to a variation in voxel size greater than $\pm 10\%$. Additionally, higher exposure is required to produce structures deeper within the polymer matrix. We compensate for this by increasing the exposure time when fabricating layers of the 3D gratings deeper within the sample. Relationships between exposure and feature size can be found in Ref [57]. We compensate for some of the effects of sample tilt and variations in thickness using stage movement to ensure that all regions of the 3D grating are fabricated at an equivalent depth within the sample.

Laser exposure parameters strongly impact the quality of fabricated structures. We attempted fabrication of 3D gratings using both the 11-MHz Ti:sapphire femtosecond laser and 80-MHz fiber femtosecond laser. Fabrication was more successful with the 11 MHz system. We attribute the differences to a combination of repetition

rate and pulse energy. The 80-MHz fiber laser system provides maximum pulse energies <1 nJ/pulse at the objective. Fabricating voxels >1 μm in size with such low pulse energies requires a long exposure time, especially when fabricating structures deep within the polymer layer. With a high repetition rate of 80 MHz, there is a very narrow range of parameters that produce acceptable structures while avoiding runaway silver growth due to heating effects in the sample. Heating effects become more pronounced at higher repetition rates. Significantly higher pulse energies >10 nJ/pulse can be used with the 11-MHz system, yielding more stable silver growth characteristics.

3.6 Multi-layer diffractive optical elements

In this section we discuss experiments related to demonstrating single- and multi-layer diffractive optical elements. These experiments provide initial proof-of-concept demonstrations of using laser-written structures for integrated diffractive optical applications.

We demonstrate successful fabrication of zone plates (Figure 3.9a), pinholes (Figure 3.9b), and direct laser writing of multi-layer structures consisting of a zone plate and pinhole. We test diffractive optical elements using a transmission microscope setup. Samples are illuminated from below. Light transmitted through the sample is collected on the other side using a microscope objective (Figure 3.10e). A beam splitter sends light to a camera to image the sample and to a spectrometer to measure the transmitted spectrum. The distance between the sample and objective determines if the diffractive elements or the focal plane of the fabricated zone plates

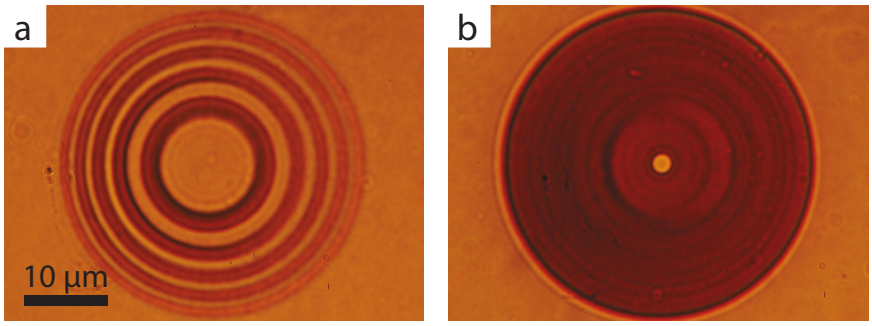

Figure 3.9: Optical image of (a) a zone plate with 50-μm focal length at 633 nm and (b) a pinhole, both fabricated by direct laser writing.

are imaged.

Zone plates fabricated by laser writing and electron beam lithography exhibit the expected focusing behavior, where the radius of each ring and the focal distance are related by:

$$r_{\mathrm{n}} = \sqrt{n\lambda f + \frac{n^2\lambda^2}{4}} \tag{3.1}$$

Where r_{n} is the ring radius, n is the order of the ring, λ is the incident wavelength, and f is the focal distance. These radii are used to define alternating opaque and transparent regions (*i.e.*, our zone plates are transparent from $r = 0\mu$m to r_1 and opaque from r_1 to r_2 and alternating thereafter). The results we report below are for zone plates with 50-μm focal length at 633 nm and a total of 10 rings (5 opaque regions). Longer focal lengths allow for easier fabrication because the width and separation of opaque rings are larger. Efficiency of laser-written zone plates is lower than the efficiency of lithographically defined zone plates.

Laser fabricated zone plates can be used to focus transmitted light from a point source (Figure 3.10a) and form images (Figure 3.10b). Depending on the separation of the zone plate and pinhole, different wavelengths are focused by the zone plate at

the pinhole aperture (Figure 3.10c and d), consistent with the expected dispersion characteristics given in Equation 3.1.

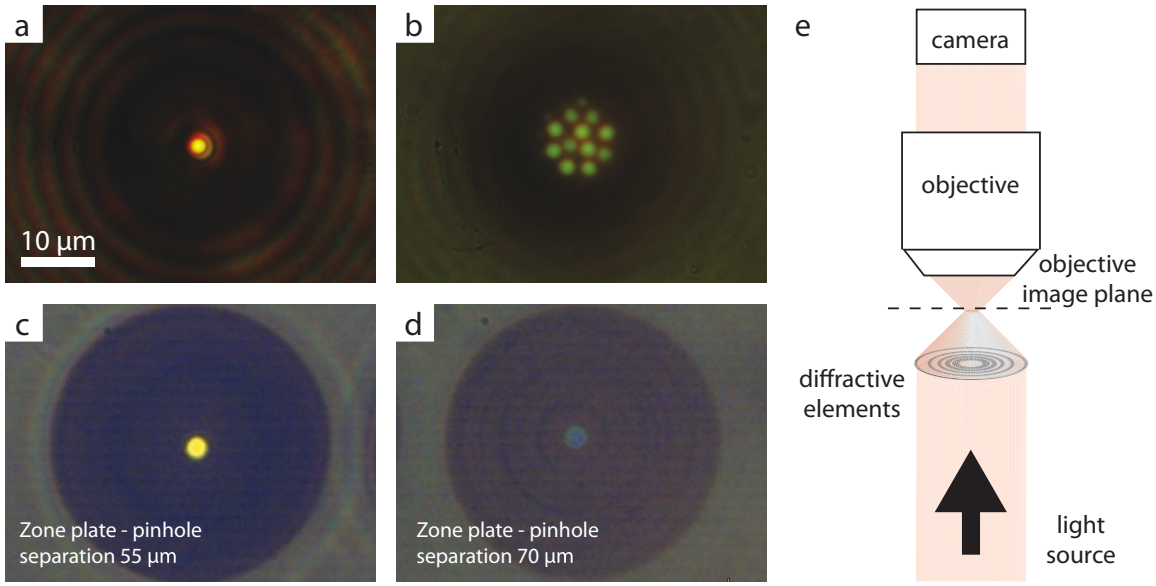

Figure 3.10: (*a*) Optical image of the focal spot produced by a laser-written zone plate of broadband illumination from a point source. (*b*) Optical image of the image formed by a laser-written zone plate of a compound LED placed below the zone plate. The image formed by the zone plate recovers the configuration of the compound LED. Panels (*c*) and (*d*) show that placing a pinhole at different separations in the z-direction from the zone plate allows selection of different wavelengths from broadband illumination. A 55-μm separation selects for wavelengths in the yellow, while a 70-μm separation selects for blue wavelengths. Panel (*e*) shows a schematic of the measurement setup. The illumination source is placed below the fabricated diffractive elements. By moving the objective in the z-direction, we can select if the diffractive elements or their image plane are in the objective image plane.

In order to measure wavelength selectivity, we fabricate arrays of zone plates within a thick ($>$ 100 μm) gelatin layer. Pinholes with an approximately 4-μm diameter aperture are fabricated above these zone plates at various distances in the z-direction. We measure the transmitted spectrum from a white light source through this multi-layer structure as a function of distance between the zone plate and pinhole,

as demonstrated in Figure 3.10c and d.

Laser-fabricated zone plates are functional, as shown by demonstrations of their dispersion characteristics (Figure 3.10c and d) and imaging (Figure 3.10b). We note that the efficiency of laser-fabricated zone plates and pinholes is lower than the efficiency of lithographically defined structures. This can be attributed to the fact that silver structures produced by direct laser writing consist of an agglomeration of silver nanoparticles held together by the polymer matrix. As a result, the silver structures are not fully opaque, allowing significant transmitted light through the structures. Additionally, surface roughness on the order of 5–50 nm due to the size of silver nanoparticles [28] in the structures can degrade performance of the diffractive elements. The advantages we gain with direct laser fabrication over lithography is the rapid fabrication of multi-layer structures and access to arbitrary orientations of diffractive elements, including tilted relative to the plane of the sample.

Wavelength selection with these laser-written structures has not led to efficient devices or conclusive measurements of the transmission spectrum. Based on the dimensions of the zone plate, we estimate an effective numerical aperture of 0.48. We calculate a transmission bandwidth for the zone plate–pinhole pair of approximately 70 nm (Figure 3.11). Although optical images at the plane of the pinhole show that the expected wavelengths are focused at the aperture, spectra taken of the transmitted light do not show a clear difference without background subtraction (Figure 3.12). We notice that the clearest difference between the incident and transmitted spectra is noticeably lower transmission in the short wavelength region. This may be due to stronger absorption of these wavelengths in the metal structures. Due to the

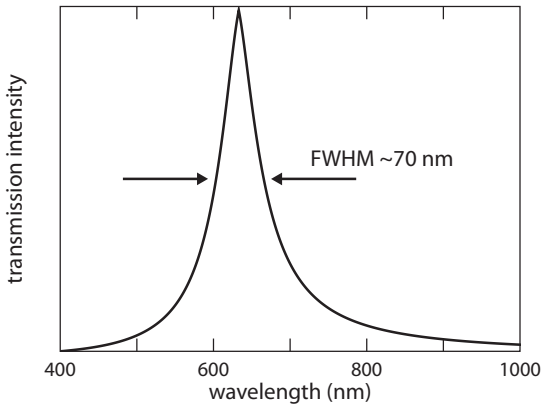

Figure 3.11: Calculated transmission spectrum for a zone plate and pinhole pair designed to transmit 633-nm light. The zone plate has an effective numerical aperture of 0.48 and the pinhole has an aperture diameter of 4 μm. The FWHM of the transmission has a bandwidth of approximately 70 nm.

aperture sizes and field of view of the microscope objective used in our test setup, a significant amount of light is collected from the regions surrounding the fabricated structures, adding to noise in the measurement. Analysis of the transmitted spectra does reveal that each zone plate and pinhole pair does preferentially transmit the designed wavelength more effectively, with a bandwidth of approximately 100 nm.

Fabrication of diffractive optical elements such as pinholes and zone plates required significantly different laser exposure parameters compared to 3D gratings. Low pulse energies of < 0.2 nJ/pulse and a high repetition rate of 80 MHz produced structures with higher opacity than using lower repetition rates and higher pulse energies. Laser exposure parameters close to the threshold for laser fabrication around 0.05–0.1 nJ/pulse and a low stage translation speed of 5–10 Âţm/s yielded structures with the greatest opacity and finest resolution. Zone plates fabricated with these parameters were most effective at focusing light and imaging. Slow stage translation speeds lead

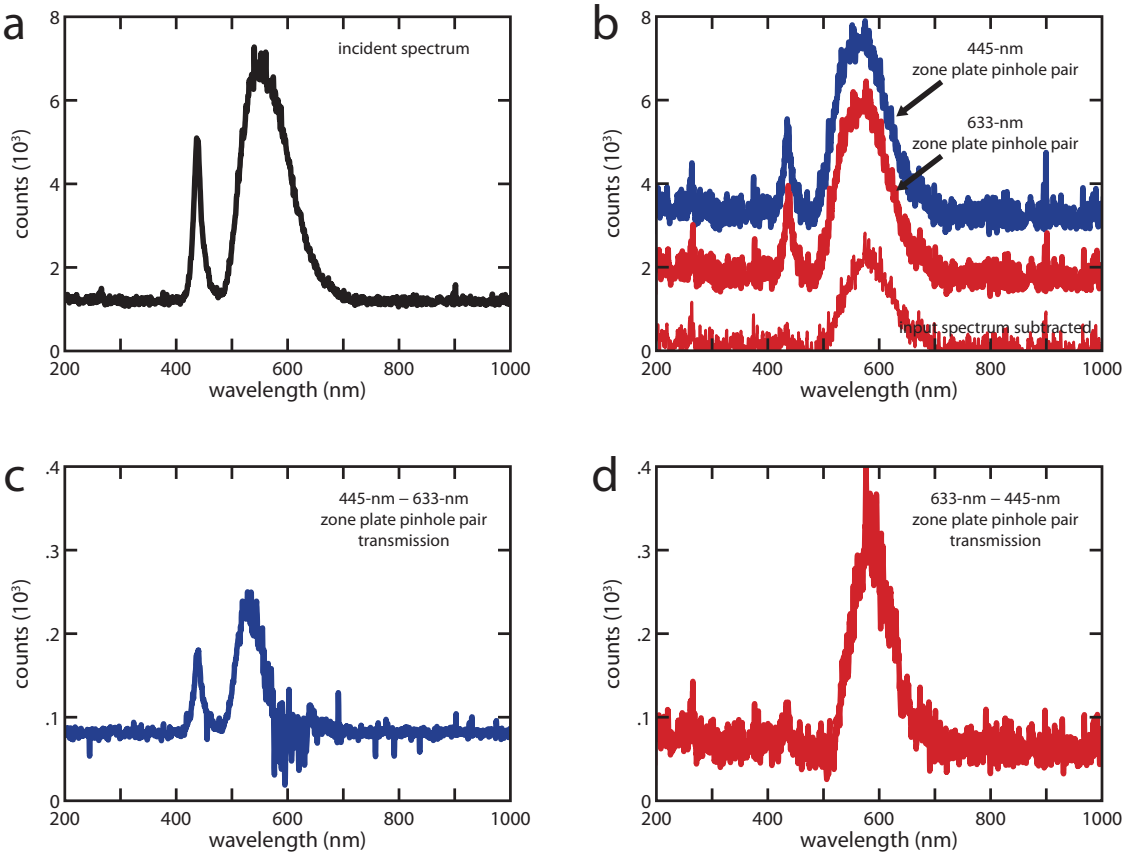

Figure 3.12: This figure shows preliminary results for wavelength selection using laser-fabricated zone plates and pinholes. Panel (*a*) shows the incident spectrum. Panel (*b*) shows the transmitted spectrum through a zone plate – pinhole pair designed to transmit 633-nm light, 445-nm light, and the spectrum transmitted through the 633-nm structure with the incident spectrum subtracted. Panel (*c*) shows the 445-nm spectrum minus the 633-nm spectrum, while panel (*d*) shows the 633-nm spectrum minus the 445-nm spectrum. This shows that there is a small difference (on the order of 1 %) between the two transmitted spectra.

to long fabrication times, limiting throughput.

3.7 Conclusion

We demonstrate the application of a novel 3D laser fabrication technique for 3D metal structures within a polymer matrix to 3D diffractive elements. We fabricate and test 3D gratings and multi-layer diffraction optical elements at visible wavelengths. 3D gratings behave close to what is expected from Laue diffraction theory. Laser fabricated zone plates can be used for focusing and imaging of light. This demonstrates that 3D direct laser writing can be used to produce operable devices.

We also note that diffractive techniques can be used to assess the quality of fabricated structures in a non-destructive manner [42–49]. Differences between expected and observed diffraction patterns provide insights into the size and uniformity of fabricated features. Diffraction results can be used as an assessment tool only if the results of measurements and calculated diffraction patterns are fully understood.

Diffractive optical elements can be used in various beam steering and manipulation schemes on the micro and macro-scale [38–41]. 3D gratings give control over incident light that is not possible with 2D or planar gratings. Laser written diffractive optical elements can be used to provide on-chip, integrated imaging systems, wavelength selection, and beam delivery in lab-on-a-chip applications. Laser fabrication allows for highly complex structures in 3D.

Further development of this laser fabrication technology must focus on overcoming several current challenges. The efficiency of diffractive elements is hindered by the limited opacity and quality of the silver structures. Dense, opaque structures would increase the efficiency of diffractive elements, such as zone plates. Achieving performance closer to that of lithographically fabricated structures is important

to make laser fabrication a viable alternative to traditional lithographic techniques. Throughput must also be greatly improved to make laser fabrication competitive. Parallel fabrication using lens arrays is one potential solution. Use of higher numerical objectives can further push the limits of minimum feature size and resolution.

Improvements to the chemistry involved with the fabrication process can also greatly impact applications. Device lifetime is limited by the polymer matrix drying out and cracking, as well as further silver growth under ultraviolet light exposure. This requires work on device packaging to protect the finished product from the outside environment. The polymer matrix could also be further developed to enable tunable or active devices. In our fabrication scheme the polymer matrix is on a rigid glass substrate. Separating the polymer from the substrate would allow the application of strain to the sample, changing the spacing between silver structures in the x, y, and z-directions on the fly. This could be used to alter the dispersive properties of diffractive optical elements and enable a variety of applications [55].

Acknowledgements

Several people contributed to the work described in this paper. MGM and KV conceived of the basic ideas for this work and GD suggested investigating zone plates and provided initial designs. MGM and SK completed sample preparation for laser fabrication. MGM and KV completed the laser fabrication work. MGM completed device measurements. PM and MGM completed simulations, calculations of diffraction patterns, and data analysis. EM supervised the research and the development of the manuscript. MGM and KV wrote the first draft of the manuscript and all

authors subsequently took part in the revision process and approved the final copy of the manuscript. The research was supported by the AFOSR and NSF.

3.8 Appendix 1 – Summary of diffraction theory

The following appendix provides a brief overview of Bragg and Laue diffraction theory. For simplicity we assume ideal point scatterers. The diffraction is built up by the interference of scattered light from all scatterers within the path of the illumination source. This is typically a source of x-rays or electrons with a narrow line width in energy. In our case, we use a continuous-wave laser.

For periodic or crystalline structures, the reciprocal lattice can be used to mathematically calculate the expected diffraction pattern. The real lattice is represented as a unit cell and basis. The unit cell consists of vectors defining the structure that is repeated to form the crystal:

$$\mathbf{a} = \begin{vmatrix} a_{11} & a_{12} & a_{13} \\ a_{21} & a_{22} & a_{23} \\ a_{31} & a_{32} & a_{33} \end{vmatrix} \tag{3.2}$$

where each row gives one of the vectors defining the shape of the unit cell. The unit cell basis gives the location of all elements (atoms, molecules, or in our case, micrometer-scale scatterers) that form a single unit cell:

$$\mathbf{v} = \begin{vmatrix} h_1 & k_1 & l_1 \\ h_2 & k_2 & l_2 \\ \vdots & \vdots & \vdots \end{vmatrix} \tag{3.3}$$

where each row represents one element of the basis. The location of each basis element is given by the product $\mathbf{a} * \mathbf{v}$.

All possible points that can appear in the diffraction pattern are given by the reciprocal lattice. The reciprocal lattice is defined by:

$$\mathbf{b} = 2\pi(\mathbf{a}^{-1})^{\mathrm{T}} \tag{3.4}$$

The reciprocal lattice points which will be visible are determined by selection rules:

$$F = \sum_{n} A_n e^{i(h_n b_1, k_n b_2, l_n b_3) \bullet (h_n a_1, k_n a_2, l_n a_3)} \tag{3.5}$$

where the indices h, k, l define the reciprocal lattice point and the coefficient A_n the scattering factor (related to the scattering cross section) of each of the n elements in the unit cell. A non-zero scattering factor, F, is required for the reciprocal lattice point to be visible and the magnitude of F determines relative intensities of diffraction maxima.

The size of reciprocal lattice points also has an impact on visibility in diffraction patterns. The size of each reciprocal lattice point is defined by the Fourier transform of the crystal producing the diffraction pattern. An infinite, perfect crystal will produce infinitely small reciprocal lattice points. As the crystal becomes smaller in a given dimension, the reciprocal lattice points become wider in that dimension. TEM samples (and our laser-written 3D gratings), for example, are very thin along the incident irradiation direction and thus produce rods in reciprocal space. A single layer of scatterers would produce rods in reciprocal space (Figure 3.13).

Diffraction techniques are used to sample different regions of the reciprocal lattice. The reciprocal lattice unit cell and structure factor define the reciprocal

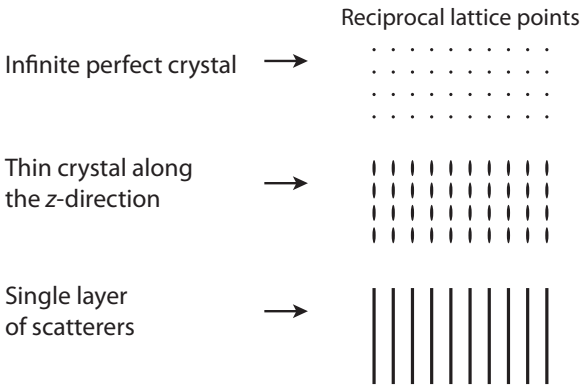

Figure 3.13: Diagram showing the shape of reciprocal lattice points as a result of changing the size of a crystal in the z-direction. A thinner crystal leads to longer reciprocal lattice points.

lattice, while the incident irradiation direction determines which reciprocal lattice planes and points will be visible. Figure 3.14 shows how the incident irradiation direction, wavelength, and reciprocal lattice are used to determine which reciprocal lattice points are visible in the diffraction pattern. A greater number of diffraction

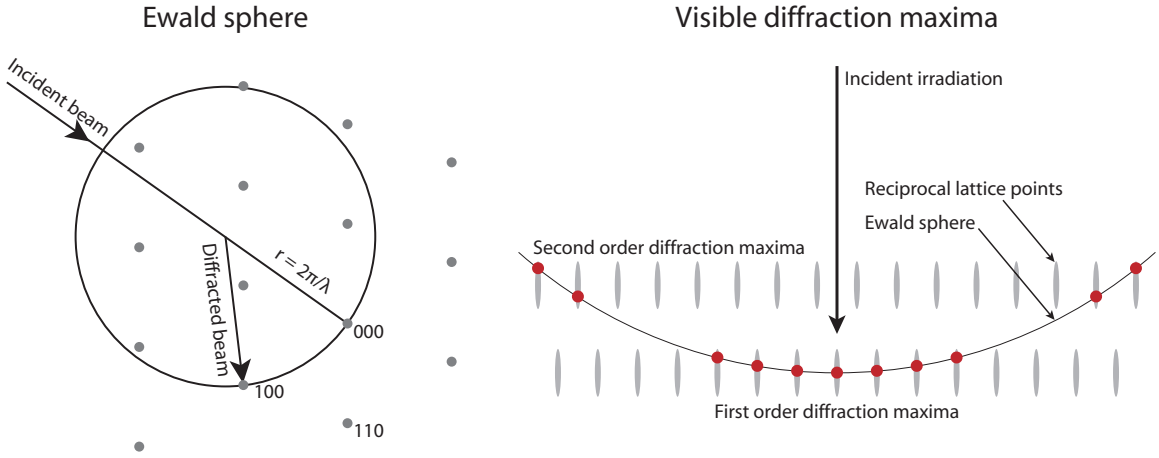

Figure 3.14: *(left)* Diagram showing a 2D depiction of a reciprocal lattice, incident beam, diffracted beam, and the Ewald sphere. The radius is given by $r = 2\pi/\lambda$. *(right)* Diagram showing which diffraction maxima are visible based on their intersection with the Ewald sphere.

maxima are visible when the sample is thinner because more reciprocal lattice rods intersect the Ewald sphere. Higher-order diffraction maxima are a result of different reciprocal lattice planes intersecting the Ewald sphere. Thin samples are necessary to make higher-order diffraction maxima visible.

Chapter 4

Laser modification of hydrogenated amorphous silicon for integrated photonic devices

4.1 Introduction

Femtosecond laser micromachining has been used to write bulk wave-guides and photonic devices in glasses, polymers, and crystalline silicon [6]. Refractive index changes in these materials tend to be less than a percent, which sets limitations on applications due to low light confinement. Hydrogenated amorphous silicon (a-Si:H) presents a unique, versatile material platform with incredible potential. Variations in the hydrogen content can produce refractive index changes as high as 0.5–1, depending on wavelength [35]. Figure 4.1 gives the trends of bandgap and refractive index as a function of hydrogen content reported by Futako et al. (2000) and Fortmann et

al. (2001) [34, 35]. Amorphous silicon can be deposited using CMOS compatible methods, providing potential for integration on a silicon platform.

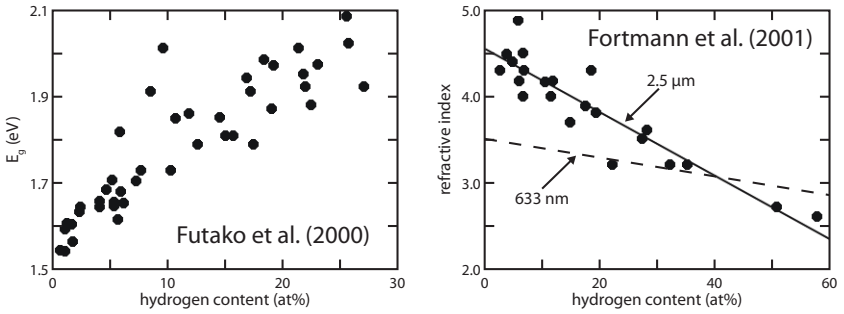

Figure 4.1: Trends of (*a*) band gap and (*b*) refractive index as a function of hydrogen content in hydrogenated amorphous silicon. Changes in hydrogen content can produce changes of 0.5–1 in refractive index [34, 35].

Waveguide fabrication through variations in hydrogen content has been demonstrated in 2D using traditional micro- and nanofabrication techniques [36, 37]. This process requires many steps and cleanroom processing, including lithography to produce a metal mask defining the waveguides, ion implantation to locally control hydrogen content, and mask removal. The waveguides consist of regions with low hydrogen content, corresponding to high refractive index. Fabrication of 3D photonic devices would require stacking many 2D layers. We are developing femtosecond laser processing to directly write complex 3D patterns in a single-step process, introducing greater versatility and processing speed.

We use femtosecond laser micromachining to locally reduce the hydrogen content of the material, with the goal of increasing the refractive index. An ultrafast pulsed laser is focused inside the bulk of a transparent material. Due to tight focusing, material modifications only occur at the focal point of the laser. Complex patterns

can by written by translating the sample with respect to the laser focus using x-, y- and z-translation. Intensity dependence of nonlinear processes enables fabrication of features with dimensions below the diffraction limit of light through careful selection of laser exposure. We will use this method to directly write three-dimensional (3D) photonic devices in a-Si:H, enabling greater versatility in devices and increased device density. Achieving these goals is critical for modern optics and electronics where space is at a premium. This novel, simple method for photonic device fabrication in a-Si:H will facilitate many applications and device integration.

In this chapter we describe the fabrication methods, including exposure parameters, to achieve modification of the properties in amorphous silicon films. We have used Raman spectroscopy and Fourier transform infrared spectroscopy (FTIR) to measure material properties of the films before and after direct laser writing. Because modification of large areas for detailed analysis of optical properties through ellipsometry is not practical due to the required material processing time, we have defined phase gratings to extract index contrast information.

4.2 Fabrication method

We use the 3D laser fabrication setup described in Chapter 3 to deliver femtosecond laser pulses to the sample. Three different lasers have been used to treat the amorphous silicon samples (Table 4.1). Several characteristics are important. The laser wavelength must be in the transparency region of the a-Si:H sample, ensuring that material changes will not be initiated by linear absorption (the transmission spectrum of the unaltered a-Si:H film is given in Figure 4.2). This will eventually

Table 4.1: Characteristics of lasers used for modification of a-Si:H samples.

Wavelength (nm)	Average power (mW)	Repetition rate (MHz)	Pulse duration (fs)	Pulse energy (nj)
1050	800	11	270	72
800	900	11	90	81
780	160	80	90	2

enable 3D fabrication. Secondly, the pulse energy must be large enough and pulse duration short enough to yield high peak intensities necessary to initiate nonlinear absorption in the material. Lastly, the laser repetition rate can impact laser writing, as will be explained below.

For initial experiments, the focus was on determining the laser exposure parameters which enable removal of hydrogen content from the silicon, without leading to crystallization of the silicon film. A combination of laser average power, pulse energy, spot size on the sample, and translation speed of the sample relative to the laser focus impact these results (summarized in Table 4.2: We find that the threshold for hydrogen removal from the a-Si:H film is very close to the threshold for crystallization of the silicon film in all cases except when using the 1050-nm laser. This means that laser stability and alignment of the film relative to the laser focal plane are very important for consistent, repeatable results. Secondly, the 80-MHz repetition rate allowed for higher stage translation speeds, while still successfully removing hydrogen from the sample without crystallization. This suggests that the hydrogen removal process is thermally mediated as high repetition rates lead to thermal buildup in the sample.

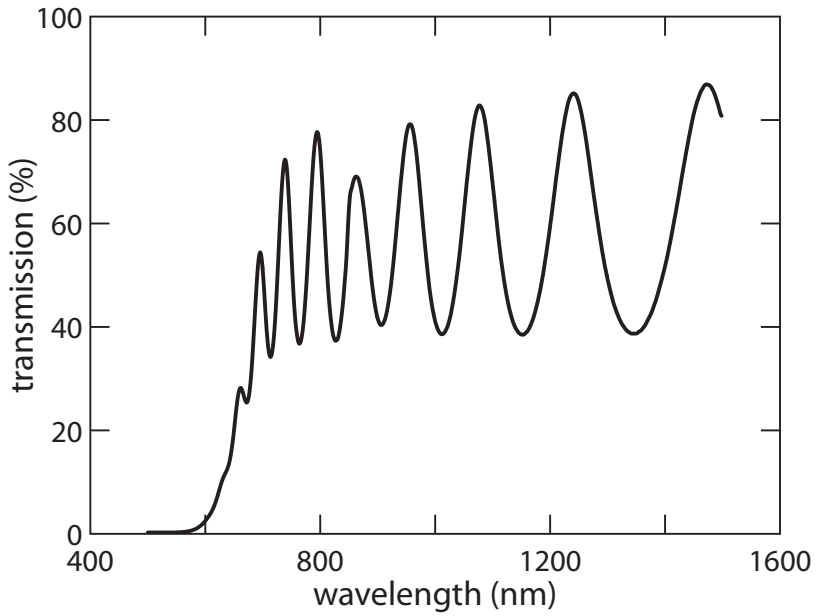

Figure 4.2: Transmission spectrum of the unaltered a-Si:H film. Note that the film becomes transparent around 650 nm, however, there is some evidence of an absorption tail up to approximately 800 nm. The oscillation in the transmission spectrum is due to interference effects in the amorphous silicon film because the thickness (930 nm) is on the order of the wavelength. These oscillations make estimations of the film absorption difficult.

However, the range of laser exposure parameters that allowed for hydrogen removal without crystallization was narrower in this case, suggesting that higher repetition rates would lead to runaway heating effects and crystallization. Shifting to shorter laser wavelengths also narrowed the range of laser powers useful for removal of hydrogen from the film. This may be due to the absorption edge of the film extending (see Figure 4.2) to the laser bandwidth, which leads to absorption in the entire interaction volume between the laser and sample. This would explain the drastic drop in average laser power required for material modification. At 1050 nm material change occurs only in regions of high intensity at the center of the focal volume because it is

Table 4.2: Laser exposure parameters for hydrogen removal from a-Si:H films and thresholds for crystallization. The write speed listed gives the maximum sample translation speed relative to the laser focus that enables significant removal of hydrogen content from the a-Si:H film. A laser spot diameter of approximately 1 μm was used in all cases.

Wavelength (nm)	Average power (mW)	Repetition rate (MHz)	Write speed (μm/s)
1050 (H removal)	40	11	5
1050 (Si crystallization)	80	11	5
800 (H removal)	8	11	5
800 (Si crystallization)	10	11	5
780 (H removal)	14	80	10
780 (Si crystallization)	16	80	10

initiated by multi-photon absorption and nonlinear interactions.

These experiments were completed using relatively high NA objectives (NA 0.8–0.9). Shifting to a lower NA objective would decrease the time necessary to modify large regions for material analysis. However, when we attempted using a low NA objective (NA 0.15) with approximately 4 μm laser spot diameter, no exposure parameters could be found which lead to hydrogen removal without silicon crystallization. We expect this may have to do with heat diffusion in the sample. Heat cannot diffuse out of the center of the laser spot between successive laser pulses, leading to heating of the sample up to the crystallization temperature.

4.3 Analysis of laser modified a-Si:H films

We have succeeded in lowering the hydrogen concentration in 2D patters within a 930-nm thick film of a-Si:H using femtosecond lasers centered at 780, 800, and 1050 nm. We use optical imaging, atomic force microscopy (AFM), and Raman spectroscopy to investigate the modified regions.

Optical imaging provides quick, qualitative analysis of the samples. Contrast is visible between unaltered and laser processed material under optical microscopy (Figure 4.3), suggesting index changes due to a reduction in hydrogen content. Contrast

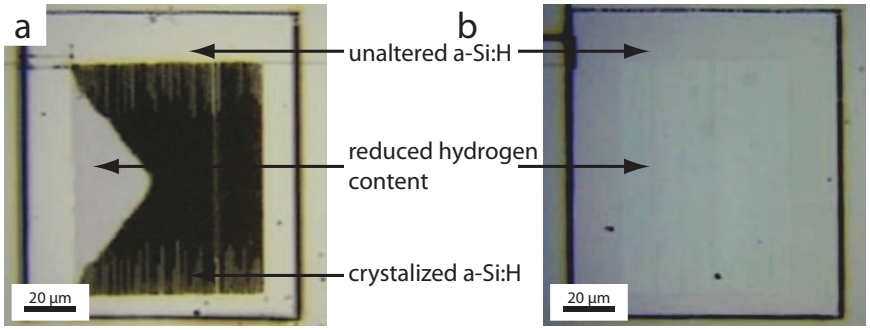

Figure 4.3: Optical images of laser-treated a-Si:H. The region in (*a*) was exposed to 1050-nm laser pulses close to the crystallization threshold. The sample was raster scanned vertically from left to right. Crystallization occurred first at the turnaround points at the left corners due to the longer dwell time of the laser in these regions. The region in (*b*) was exposed to 1050-nm laser pulses near the threshold of hydrogen removal, leading to low contrast between modified and unmodified regions.

increases with laser fluence or a greater number of incident laser pulses, starting at the thresholds given in Table 4.2. As laser exposure reaches the threshold for crystallization, changes in optical images are obvious. Explosive hydrogen effusion from the sample rips apart the film, producing a dark region on the sample.

The modified region in Figure 4.3a was further investigated using AFM (Fig-

ure 4.4). AFM can be used to ensure that the surface morphology of the sample is

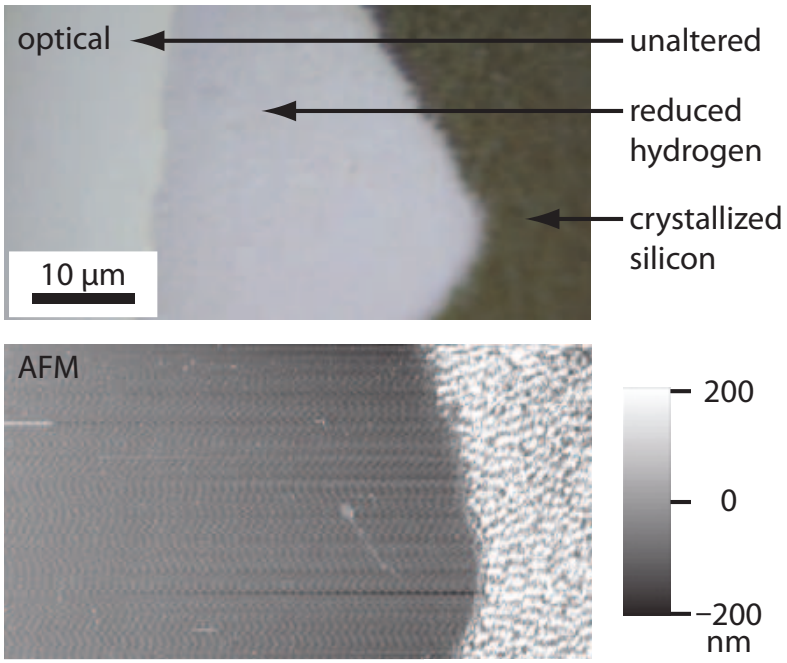

Figure 4.4: AFM of the laser treated region in Figure 4.3a. The crystallized region shows a clear increase in roughness. The laser modified region which is not crystallized exhibits no noticeable change in surface morphology relative to the unaltered a-Si:H film.

not altered due to laser writing. Controlling the hydrogen content of a-Si:H using ion implantation can lead to reduction in the height of the sample in ion implanted regions. By contrast, we find no change in the surface morphology, provided that the film is not crystallized as a result of laser exposure.

We used Raman spectroscopy to directly verify the reduction in hydrogen content. The ratio of peak intensities for the Si-H bonding peaks (2000 and 2100 cm^{-1}) to Si-Si bonding around 480 cm^{-1} corresponds to the hydrogen content of the film [58]. A reduction in the Si-H peak intensity corresponds to a reduction in hydrogen content. With laser exposure close to, but below the crystallization threshold we find a

reduction in the ratio between the Si-H to Si-Si peak intensity of approximately 30% (Figure 4.5). For laser exposure above the crystallization threshold, the modified re-

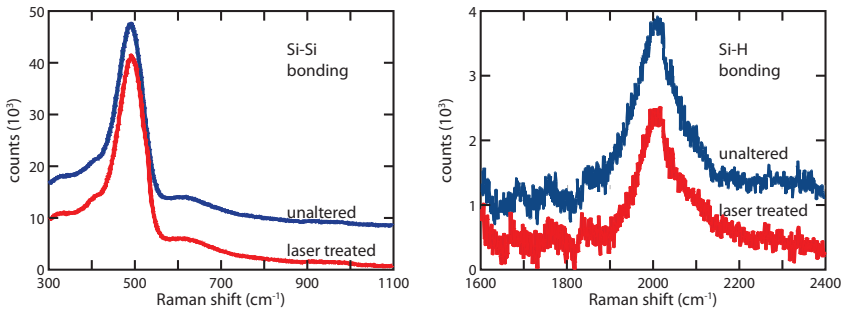

Figure 4.5: Raman spectra of unaltered and laser treated a-Si:H close to, but below the crystallization threshold using a 1050-nm laser. The intensity ratio between the Si-H to Si-Si bonding peaks drops by approximately 30%.

gions exhibit a clear crystalline silicon Raman signal at 520 cm^{-1} in addition to the broad amorphous silicon Raman signal around 480 cm^{-1} (Figure 4.6).

These initial results provide a proof of concept and valuable knowledge for the fabrication of devices.

4.4 Phase grating analysis

We use measurements from a phase grating to estimate the index contrast between unaltered and laser processed a-Si:H. Phase gratings produce diffracted beams based on phase differences imparted on incident light traveling through different regions of the structure. In most cases, this phase difference is produced by adding or removing material to different regions of the grating. Phase gratings can be produced by a-Si:H by introducing an index change in some regions of the sample.

We fabricate a 1 × 1-mm phase grating in a-Si:H using 15 mW of average power

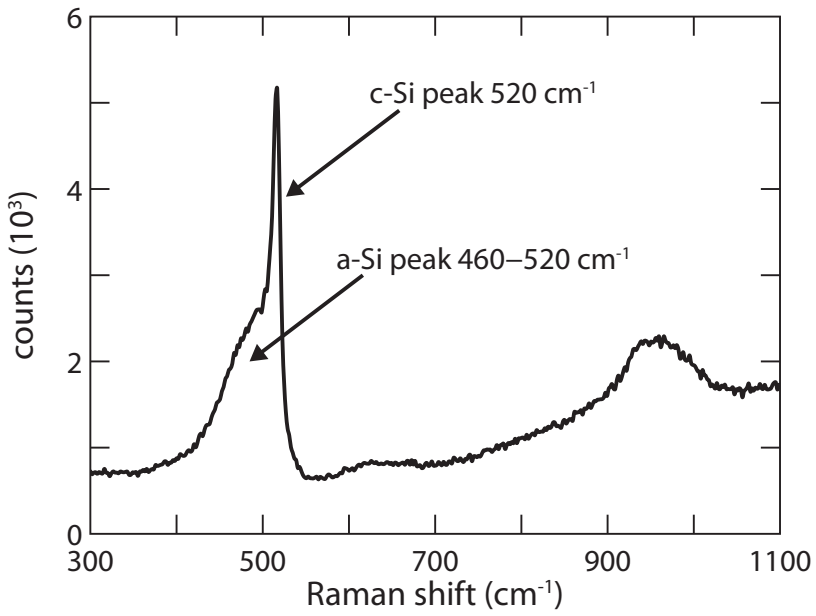

Figure 4.6: Raman spectrum of a-Si:H crystallized by exposure to a 1050-nm laser above the crystallization threshold. Notice that a sharp peak indicative of the presence of crystalline silicon is visible at 520 cm^{-1}.

from the 780-nm laser. The phase grating consists of vertical 5 × 1000-μm regions of laser processed a-Si:H separated by 5 × 1000-μm regions of unmodified a-Si:H (Figure 4.7a). With 633-nm light incident on the grating, we expect a first order diffraction angle of approximately 4°.

Based on the intensity of the diffracted beam, we can estimate the index change of the material in the modified region. Light passing through the modified region will accumulate a greater phase than light passing through the unmodified film because it will experience a higher refractive index where hydrogen has been removed from the a-Si:H layer. Phase gratings produce the greatest diffraction intensity when the phase difference is equal to π. Figure 4.7b shows the diffraction pattern produced. The diffraction efficiency achieved is <1%. This suggests an index change on the

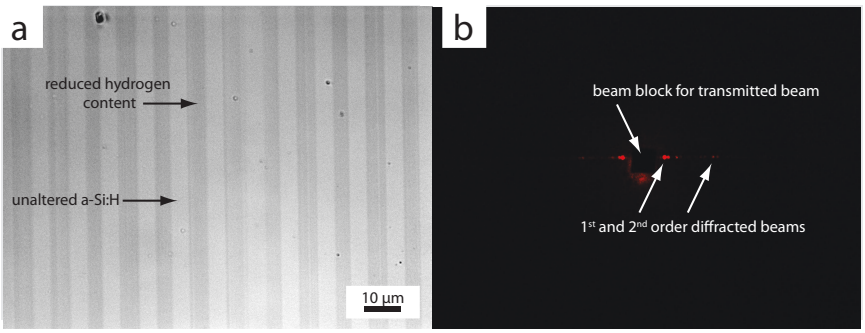

Figure 4.7: (*a*) Optical image of one region of a 1 × 1mm phase grating in a-Si:H. The laser-modified regions have been exposed to 15 mW of average power from a 780-nm laser. The laser focal spot was approximately 1 μm in diameter and a 10-μm/s stage translation speed was used. (*b*) Image of the diffraction pattern produced when 633-nm light is passed through the grating. The transmitted beam is blocked.

order of 10^{-2}.

4.5 Conclusions and outlook

We were able to find experimental evidence of hydrogen removal from a-Si:H films using direct laser writing. The necessity for low write speeds suggest that the kinetics of hydrogen removal from the amorphous silicon film are relatively slow. It is also unclear if the hydrogen is removed entirely from the film or moves into regions of the film surrounding the modified region. This could introduce an additional limitation on producing 3D laser-written structures in thick films of a-Si:H.

The large difference in laser-writing threshold between using a 1050-nm laser versus 800-nm laser suggests that material modification occurs due to nonlinear optical interactions for longer wavelengths and that the absorption tail in the material impacts the laser-writing process at shorter wavelengths. This shows that using a

laser wavelength several 100 nm above the absorption edge would be necessary for producing 3D structures in a-Si:H.

The low index contrast and low laser write speeds are major limitations that would need to be overcome in order to achieve practically useful results with this fabrication technique. One of the major draws of using a-Si:H would be to enable high index contrast structures through control of the hydrogen content in the film. The major draw of using direct laser writing is to enable 3D fabrication of structures without requiring multiple sets of lithographic fabrication, however, the laser write speed of structures must be competitive.

4.6 Acknowledgement

We acknowledge Howard Branz at NREL for providing the hydrogenated amorphous films used in this work and for engaging in valuable discussion while starting these experiments.

Chapter 5

Introduction to integrated optics

5.1 Overview

We now move to our work in integrated titanium dioxide (TiO_2) nanophotonic devices. Recent work in the group has focused on developing TiO_2 as a platform for integrated optics and integrated nonlinear nanophotonic devices [**?**, 59–62]. Our most recent focus has been on exploring the use of nanoscale waveguides as a source for entangled photon triplets generated by third-order spontaneous parametric down-conversion (TOSPDC). This chapter will provide motivation for moving from bulk optics to integrated optics and reasons for working with TiO_2 as opposed to more mature material platforms.

For derivations and detailed descriptions of the physics of guided optics and nano-scale waveguides, see the following references [12, 63–65].

The theory of generating photon triplets via TOSPDC in integrated nanophotonic waveguides is discussed in detail in Chapter 6 and experimental considerations

are discussed in Chapter 7.

5.2 Motivation for integrated optics and TiO_2

The move from bulk (table-top) to integrated optics is driven by several factors: miniaturization, the opportunity to package a single device to perform complex functions, and the enhancement of nonlinear interactions through intense optical fields and long interaction lengths. These factors play into why TiO_2 is a desirable material platform to work with.

Physical space is becoming an increasingly important commodity in modern devices and applications. As a result, the ability to scale down the size of a device and pack greater functionality into a small area is becoming more desirable. This outlines the importance of enabling light confinement on a small scale. The minimum beam sizes that can propagate across macro-scale distances in free space without significant divergence are on the order of 1 mm. Guided optics, on the other hand, provide continuous confinement of light along long distances, enabling confinement on the micrometer scale. Additionally, high index materials enable confinement of light in areas smaller than the diffraction limit in free space, further shrinking the size necessary for individual waveguides and components.

Alignment is an additional consideration. Free-space optics requires alignment of individual optical elements and are often subject to drift. Integrated optical components, once fabricated, eliminate the need for periodic alignment. Additionally, integrated components can be packaged inside a cladding layer, providing protection from the outside environment. Removing the presence of moving parts in a system

greatly increases robustness in transport. Temperature changes can still cause an issue for both free-space and integrated optical systems. In both cases thermal expansion can impact performance and materials used for waveguides are impacted by thermally-induced changes to the refractive index, which will change light propagation behavior in the material.

Depending on the material system used for devices, integration with existing electrical components on-chip is possible. Generally, this will require CMOS compatible fabrication techniques to be applicable for the optical materials. Important considerations also include the required temperatures for material deposition and patterning techniques, as these temperatures cannot exceed the thermal budget of other components already present on the device. The eventual goal with integrated optics is to produce systems that include light sources, an optical system that makes use of the generated light, and detectors directly on-chip.

On the subject of nonlinear optical interactions, integrated optics provides several key advantages. Long waveguides can provide long interaction lengths between the pump and signal wavelengths in nonlinear optical interactions. Particularly for weak nonlinear interactions, these long interaction lengths can be critical for achieving high efficiency. Intensity-dependent interactions benefit greatly from the strong light confinement provided by nanoscale waveguides fabricated in high-index media. By confining light to nanoscale structures, very high intensities can be achieved, boosting the efficiency of certain nonlinear interactions. Phase-matching schemes can also be realized that make use of different guiding modes (see Chapter 6), enabling tunable phase-matching for widely-separated wavelengths. Resonant structures, such as ring

resonators formed of integrated waveguides, can be used to further increase interaction lengths and field enhancements and their resonant conditions can lead to fine control of the output spectrum for nonlinear interactions.

TiO_2 has a variety of properties that make it advantageous for integrated optics and provide advantages relative to other material platforms. Silicon photonics is one of the most mature areas within integrated optics, boasting well-developed fabrication techniques and low propagation losses [66–71]. However several key factors make it unsuitable to certain applications. Silicon is only transparent for wavelengths > 1100 nm. As a result, visible and near infrared light propagation is not possible. For nonlinear applications, working above the half band gap ($\lambda < 2200$ nm) can lead to significant problems related to two-photon absorption. TiO_2 is transparent down to approximately 400 nm, enabling operation in the visible and operation free of two-photon absorption for wavelengths > 800 nm. A high linear refractive index enables strong light confinement in nanoscale waveguides. TiO_2 also has a high $\chi^{(3)}$ nonlinearity, approximately $30\times$ that of silica, making it an excellent platform for processes such as nonlinear refraction, four-wave mixing, third-harmonic generation, and third-order down-conversion. TiO_2 has an indirect bandgap which greatly reduces fluorescence in the material. The negative thermo-optic coefficient (meaning the refractive index decreases with increasing temperature) enables design of athermal devices (where the operation is unaffected by temperature changes) utilizing standard cladding materials, such as SiO_2, with positive a positive TOC. Finally, TiO_2 is CMOS compatible because it can be deposited on a variety of substrates at low temperature and fabrication methods exist that are CMOS compatible.

Other material platforms do exist for visible applications. Notable examples of materials with smaller band gaps which are used heavily in photonics applications include chalcogenide glasses, gallium arsenide, and silicon. These materials have a higher linear refractive index and nonlinear susceptibility, however, the transparency window starts at longer wavelengths than for TiO_2. Chalcogenide glasses have been investigated heavily because tuning the material composition enables tuning of the index, transparency regime, and nonlinear properties [72–76]. Significant improvements to fabrication have greatly reduced losses [77]. The most notable examples with larger band gaps than TiO_2 are silicon nitride and diamond. Silicon nitride in particular has been used to fabricate very low-loss waveguides and has a nonlinearity that is close to that of TiO_2, making it an attractive platform for nonlinear optical interactions [78–80]. However, silicon nitride does fluoresce more strongly when exposed to visible light. Diamond photonics has been developed in recent years for linear guided optics, nonlinear optics, and as a single-photon source [81–84]. Low losses have been achieved in the visible, but fabrication remains challenging and the magnitude of the nonlinearity is lower than in TiO_2.

Chapter 6

Efficient photon triplet generation in integrated nanophotonic waveguides

6.1 Preface

This chapter covers material presented in: Michael Moebius, Felipe Herrera, Sarah Griesse-Nascimento, Orad Reshef, Christopher Evans, Gian Giacomo Guerreschi, Alán Aspuru-Guzik, and Eric Mazur. "Efficient photon triplet generation in integrated nanophotonics waveguides," *manuscript submitted*, 2016. Classical calculations of phase-matching, nonlinear mode overlap, photon triplet generation rates, device design and optimization methods, and experimental validation of the phase-matching and mode overlap calculations via third harmonic generation (THG) were completed primarily by Michael Moebius, Sarah Griesse-Nascimento, Orad Reshef, and Christopher Evans in Eric Mazur's research group. Quantum mechanical descriptions of photon triplet generation rates and temporal coherence properties for photon triplets

were developed primarily by Felipe Herrera and Gian Giacomo Guerreschi in Alán Aspuru-Guzik's research group.

6.2 Abstract

Generation of entangled photons in nonlinear media constitutes a basic building block of modern photonic quantum technology. Current optical materials are severely limited in their ability to produce three or more entangled photons in a single event due to weak nonlinearities and challenges achieving phase-matching. Photon losses in materials and devices further limit performance. We use integrated nanophotonics to enhance nonlinear interactions and develop protocols to design multimode waveguides that enable sustained phase-matching for third-order spontaneous parametric down-conversion (TOSPDC). In the presence of typical losses, we predict a generation efficiency of 0.13 triplets/s/mW of pump power in TiO_2-based integrated waveguides, an order of magnitude higher than previous theoretical and experimental demonstrations. We experimentally verify our device design methods in TiO_2 waveguides using third-harmonic generation (THG), the reverse process of TOSPDC that is subject to the same phase-matching constraints. We finally discuss the effect of finite detector bandwidth and photon losses on the energy-time coherence properties of the expected TOSPDC source.

6.3 Introduction

Optical quantum technologies [85] often rely on nonlinear optical crystals pumped with coherent radiation to generate light with non-classical properties, including entanglement. Entangled photons have applications in many fields, such as quantum cryptography [86], quantum metrology [87], quantum imaging [88,89], quantum spectroscopy [90], and quantum information processing [91]. Many experimental efforts aim towards the generation, manipulation, and detection of entangled photons using nanoscale optical devices that provide a compact and scalable platform to perform quantum optics experiments on a single chip [85].

Entangled states of light containing three or more photons are currently built interferometrically starting from entangled photon pairs or single photons [86], with entangled pairs typically generated via spontaneous parametric down-conversion (SPDC) [92], biexciton decay [93], and spontaneous four-wave mixing [94]. Tripartite entanglement can be used for quantum secret sharing [95] and measurement-based quantum computing [96]. The production of entangled photon triplets via cascaded SPDC has been demonstrated [97–99], with generation efficiencies on the order of 10^{-2} triplets/s/mW pump power [98]. Third-order spontaneous parametric down conversion (TOSPDC), when one pump photon splits into three signal photons, can also generate entangled photon triplets. The temporal coherence properties of TOSPDC photon triplets are different from cascaded SPDC sources [100].

TOSPDC represents an experimental challenge [101] due to low third-order nonlinearities ($\chi^{(3)}$) in typical optical materials. Moreover, phase-matching becomes increasingly difficult to satisfy for widely-spaced wavelengths. Recently, nanoscale

optical devices have emerged as a promising route to enhance nonlinear-optical processes, mostly due to high field intensity from sub-wavelength confinement of the electromagnetic field [85]. In addition, sustained phase-matching for widely-spaced wavelengths can be achieved using strong dispersion in non-fundamental waveguide modes. These remarkable improvements over bulk materials indicate that integrated nanophotonic waveguides can enable efficient TOSPDC.

In this work, we propose a protocol to optimize efficient generation of entangled photon triplets via TOSPDC in nanophotonic waveguides. We discuss in detail how to optimize key design parameters, such as phase-matching and mode overlap between visible pump and infrared signal modes, while also considering the impacts of photon losses. Our proposed design protocol can be applied to many waveguide materials and geometries. We validate our design protocol experimentally by demonstrating THG, the reverse of TOSPDC, in nanoscale TiO_2 waveguides. Titanium dioxide (TiO_2) is a promising material platform for efficient TOSPDC [**?**,59–61,102]. Pumping with a visible laser at λ_p = 420–450 nm or 510–520 nm generates photons in the O and C telecommunication bands, allowing integration with silicon photonics, existing telecommunications infrastructure, and efficient single photon detection [103]. We finally calculate the temporal coherence properties of TOSPDC sources in coincidence measurements, taking into account finite detector bandwidths and propagation losses.

6.4 Device Design

TOSPDC in bulk nonlinear optical materials has previously been ruled out as a viable source of entangled photons due to the inherent difficulty of achieving

phase-matching across nearly two octaves, low $\chi^{(3)}$ nonlinearities, and weak light confinement over long interaction lengths [101]. TOSPDC in nano-scale silica fibers was proposed theoretically by Corona et al. [104]. The predicted photon triplet generation efficiency in 10-cm long silica fibers, ignoring the impact of photon losses, is 1.9×10^{-2} triplets/s/mW of pump power [104,105], which is comparable to current experimental demonstrations [97,98]. However, silica fibers cannot be easily integrated to produce on-chip photon triplet sources due to incompatibility with CMOS fabrication techniques and low index contrast with commonly-used cladding materials.

We propose to use an alternative material, TiO_2, for its high refractive index, high $\chi^{(3)}$ nonlinearity, and CMOS compatibility [62,106]. These characteristics make TiO_2 an excellent platform for an on-chip, integrated photon triplet source.

Optimizing the efficiency of photon triplet generation in nanophotonic waveguides requires four major considerations: phase-matching, mode overlap, interaction length, and power coupled into the phase-matched pump mode. In the rest of this section, we define criteria to optimize these factors and achieve the largest triplet generation efficiency. We consider photon losses due to their impact on conversion efficiency, optimal device length, and signal spectrum. Using optimized parameters for a TiO_2 nanoscale waveguide, we predict its performance for TOSPDC under realistic conditions, including photon losses.

6.4.1 Higher-order mode phase-matching

According to Fermi's golden rule [101], the transition rate for the conversion of a pump photon of frequency ω_{p} into three signal photons at frequencies denoted as ω_{s}, ω_{r}

and ω_{i} is strongly suppressed for any combination of frequencies that does not satisfy the energy conservation constraint $\omega_{\mathrm{p}} = \omega_{\mathrm{r}} + \omega_{\mathrm{s}} + \omega_{\mathrm{i}}$. The probability of generating signal photons that satisfy energy conservation is maximal for those combinations that also satisfy the phase-matching or momentum-conservation rule, $\mathbf{k}_{\mathrm{p}} = \mathbf{k}_{\mathrm{r}} + \mathbf{k}_{\mathrm{s}} + \mathbf{k}_{\mathrm{i}}$, where $\mathbf{k}_m$ is the wavevector of each photon in mode $m = \{\mathrm{p}, \mathrm{s}, \mathrm{r}, \mathrm{i}\}$. In this work, we consider nanoscale ridge waveguides (Figure 6.1b), for which the propagation direction of guided modes is along the waveguide. In this case, momentum conservation reduces to a scalar identity for the magnitude of the wavenumbers of propagating modes $k = 2\pi n_{\mathrm{eff}}/\lambda$, where n_{eff} is the effective refractive index of the signal mode at wavelength λ.

The wavelength dependence of the effective index $n_{\mathrm{eff}}(\lambda)$ in guided modes is determined by the waveguide geometry, dispersion properties of the core and cladding materials, and mode order. In the optical regime, the refractive index for a transparent material is typically larger at the shortest wavelengths, monotonically decreasing with increasing wavelength. For example, in TiO_2 there is an index mismatch of 0.17 between a 532-nm pump and 1596-nm signal wavelength, which leads to a 1.6-μm coherence length. Additionally, for a given wavelength λ, higher-order modes have a lower effective index than the fundamental mode. In Figure 6.1a, we demonstrate these two points by plotting the effective index for two modes (*i.e.*, the TM_{00} fundamental [signal] and TM_{02} higher-order [pump] modes) of a TiO_2 waveguide with a 550-nm core width and a 360-nm thickness, with an SiO_2 cladding. By employing a higher-order mode at the shorter wavelength, we can match effective indices for highly disparate wavelengths [61, 107].

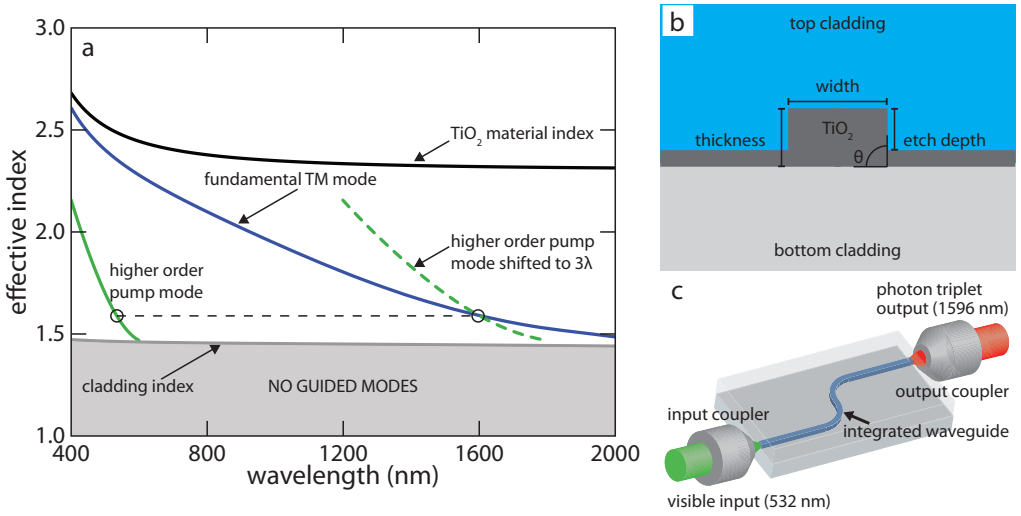

Figure 6.1: (*a*) Schematic of higher-order mode phase matching using calculated dispersion data for a fully-etched 550 × 360 nm TiO_2 waveguide with SiO_2 cladding. Shifting the pump mode from λ_p to $3\lambda_p$ gives a point of intersection where the effective indices of the TM_{00} signal and TM_{02} pump modes are the same. Phase matching is achieved at $\lambda_p = 532$ nm. Guided modes reach a cutoff wavelength when their effective index is equal to the cladding SiO_2 index (gray curve). (*b*) Schematic of the waveguide cross section and tunable parameters. (*c*) 3D schematic of an integrated device with input and output coupling.

We define the perfect phase matching (PPM) point as the pump wavelength λ_p^0 for which $n_{\text{eff}}^s(3\lambda_p^0) = n_{\text{eff}}^p(\lambda_p^0)$, where n_{eff}^s is the effective index of the signal mode of interest and n_{eff}^p is the pump index. At the PPM point, the phase-matching condition reads $k_p^0 = 3k_s^0$, since all three signal photon frequencies are degenerate. For the case of a monochromatic pump at the PPM-condition, the signal photons can be generated away from $\omega_p/3$, so long as energy conservation is maintained. A finite phase-mismatch will result from group velocity dispersion (GVD) in the signal mode ($D_s = \partial^2 k_s/\partial\omega_s^2|_{\omega_s=\omega_s^0}$), limiting the bandwidth. The signal bandwidth at PPM is thus given by Δ_{PPM}, corresponding to the FWHM of the function $\text{sinc}^2(\Delta kL/2)$,

which determines the triplet generation rate as a function of finite phase mismatch (see Section 6.4.3):

$$\Delta_{\mathrm{PPM}} = \sqrt{\frac{4\pi}{L|D_{\mathrm{s}}|}} \tag{6.1}$$

where L is the nonlinear interaction length. The relative intensities of the signal photons that are emitted for the PPM case are visualized in Figure 6.2a, where the idler (ω_{r}, ω_{i}) vs. signal-frequency (ω_{s}) intensity-plot shows a single peak centered at the degenerate signal frequency. The black curve in Figure 6.2d shows corresponding intensity of all three signal photons as a function of frequency.

In TOSPDC, the pump wavelength can be blue-detuned away from the PPM point while still satisfying energy and momentum conservation efficiently for normal signal-mode dispersion. This produces non-degenerate photon triplets in energy. Energy and momentum conservation cannot simultaneously be satisfied for a red-detuned pump with normal dispersion in the signal mode. Satisfying energy and momentum conservation rules for 1D propagation results in an under-constrained system of equations with two free parameters. One is fixed by choosing the pump frequency $\omega_{\mathrm{p}} = 2\pi c/\lambda_{\mathrm{p}}$. We can choose the remaining degree of freedom to be one of the signal frequencies ω_m, with $m = \{\mathrm{s}, \mathrm{r}, \mathrm{i}\}$.

We refer to the range of signal frequencies over which energy and momentum conservation is fulfilled for TOSPDC as the signal bandwidth δ_{s} (derived in Appendix 6.7), given by:

$$\delta_{\mathrm{s}} = 2\left(\frac{2}{3}\right)^{1/2}\left[\frac{2\left(v_{\mathrm{p}}^{-1} - {v_{\mathrm{s}}}^{-1}\right)}{D_{\mathrm{s}}}\Delta_{\mathrm{p}} + \left(\frac{D_{\mathrm{p}}}{D_{\mathrm{s}}}\right)\Delta_{\mathrm{p}}^2\right]^{1/2}, \tag{6.2}$$

where $\Delta_{\mathrm{p}} = \omega_{\mathrm{p}} - \omega_{\mathrm{p}}^0$ and $\Delta_m = \omega_m - \omega_{\mathrm{p}}^0/3$, with $m = \{\mathrm{s}, \mathrm{r}, \mathrm{i}\}$, are the pump and signal detunings from the PPM point. ω_{p}^0 is the pump frequency that gives PPM. v_{p}

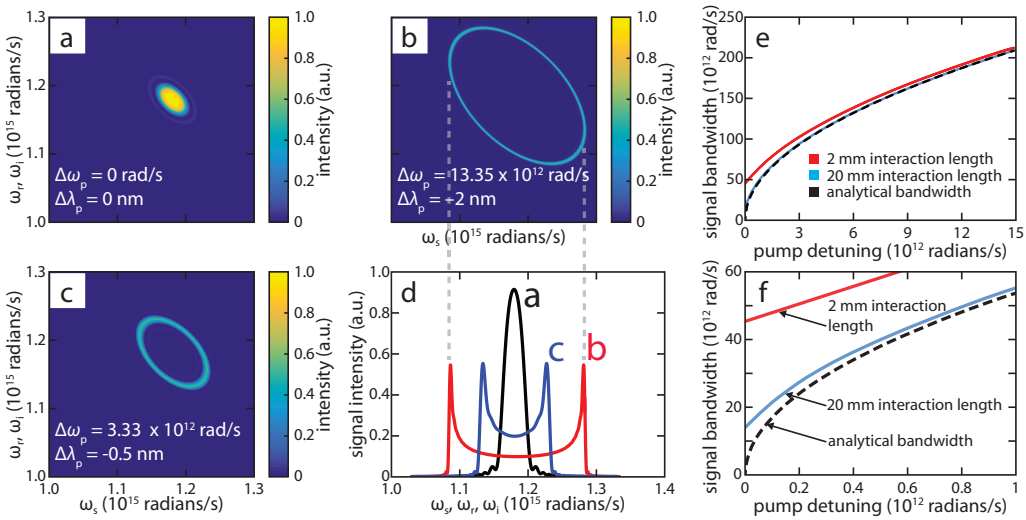

Figure 6.2: We visualize the joint spectral intensity as an intensity plot of frequency versus frequency for several values of the pump detuning $\Delta\lambda_{\mathrm{p}}$ from the PPM wavelength. Panels (a), (b) and (c) correspond to $\Delta_{\mathrm{p}} = 0$, $\Delta_{\mathrm{p}} = -2$ nm and $\Delta_{\mathrm{p}} = -0.5$ nm, respectively. We assume a waveguide length $L = 2$ mm and use dispersion values for the phase matching point shown in Figure 6.1. Fixing one of the three signal wavelengths (ω_{s}) on the horizontal axis, the two other signal wavelengths (ω_{r} and ω_{i}) are given by the two values on the vertical axis that intersect the ellipse. Phase matching is achieved along the perimeter of the ellipse and the thickness is determined by the pump and signal interaction length, based on Eq. (6.1). By collapsing the plots in (a), (b), and (c) onto the horizontal axis, we generate the spectra shown in (d). All three spectra are normalized by the total conversion efficiency. Panel (e) shows signal spectrum bandwidth as a function of pump detuning $\Delta\omega_{\mathrm{p}}$. The dashed black curve gives the bandwidth defined by Eq. (6.2). Red and blue curves are numerically obtained signal bandwidths for waveguide lengths $L = 2$ mm and $L = 20$ mm, respectively. Panel (f) zooms near the PPM point.

and v_{s} are the group velocities of the pump and signal modes at the PPM point, and D_{p} and D_{s} are their group velocity dispersion.

For a long interaction length L and a monochromatic pump with detuning Δ_{p}, the signal frequencies that satisfy energy and momentum conservation simultaneously

can be represented in a (ω_s, ω_r)-plane by the ellipse (derived in Appendix 6.7):

$$\Delta_s^2 + \Delta_r^2 - \Delta_r\Delta_s - \Delta_p(\Delta_r + \Delta_s) = A_p, \tag{6.3}$$

where $A_p = (3/16)\delta_s^2 - \Delta_p^2$. In Figures 6.2b and 6.2c, we plot the relative intensity of emitted signal photons in a frequency-frequency plane for cases where the pump is slightly detuned from the PPM point. The highest intensities occur at frequencies satisfying the ellipse equation above. The photon triplet wavefunction has a non-vanishing amplitude for signal frequencies outside the ellipse in Eq. (6.3); however these frequencies are strongly suppressed because of poor phase matching (Figure 6.2b and 6.2c).

The ellipse width δ_s grows with a scaling $(\Delta_p)^{1/2}$ for pump detuning $0 < \Delta_p < \Delta_p^c = 2(v_s - v_p)/(v_p v_s D_p)$ and with a scaling $(\Delta_p)^1$ for greater pump detuning. Maximizing signal D_s and minimizing $v_s - v_p$ and D_p minimizes signal bandwidth for finite phase mismatch. This provides a method to minimize signal bandwidth in the case that fabrication variations introduce finite phase mismatch. For fixed pump detuning Δ_p, the signal bandwidth δ_s in Eq. (6.2) corresponds to the distance between the highest and lowest points in the ellipse. The corresponding spectrum consists of a two-peak structure with intensity maxima ocurring roughly at frequencies $\omega_p^0/3 \pm \delta_s/2$ (Figure 6.2d). The spectra in Figure 6.2 are obtained numerically by computing the triplet generation rate from Eq. (6.6) in Section 6.4.3.

In Figure 6.2e, we plot the signal bandwidth δ_s as a function of pump detuning Δ_p for the TiO_2 waveguide parameters from Figure 6.1. The bandwidth is obtained from numerical spectra (as in Figure 6.2a, b, and c) computed at 1/10-th the peak maximum, for the interaction lengths $L = 2$ mm and $L = 20$ mm. As the pump-signal

interaction length increases, the spectral amplitude of the three-photon state (Section 6.4.3) approaches a delta function in the phase mismatch $\Delta k = k_{\mathrm{p}} - k_{\mathrm{r}} - k_{\mathrm{s}} - k_{\mathrm{i}}$. In this limit, the bandwidth δ_{s} in Eq. (6.2) accurately matches the numerical bandwidth. The discrepancy between analytical and numerically calculated bandwidth is greatest at $\Delta_{\mathrm{p}} = 0$, with a minimum bandwidth $\delta_{\mathrm{s}} = 54 \times 10^{12}$ rad/s for $L = 2$ mm and $\delta_{\mathrm{s}} = 14 \times 10^{12}$ rad/s for $L = 20$ mm. As we discuss in Section 6.4.3, photon loss due to scattering and absorption reduces the effective interaction length, thus broadening the signal.

6.4.2 Effective nonlinearity and modal overlap

Once phase matching and energy conservation are satisfied for the interacting pump and signal modes, the efficiency of TOSPDC is determined by the effective nonlinearity [104]:

$$\gamma = \frac{3\chi^{(3)}\omega_{\mathrm{p}}}{4\epsilon_0 c^2 n^2}\eta\,, \tag{6.4}$$

where n is the material index and $\chi^{(3)}$ is the effective third-order susceptibility at the pump frequency. We can define η as the sum of mode overlap components $\eta_{ijkl} \equiv [A_{\mathrm{eff}}^{ijkl}]^{-1} = \iint E_{\mathrm{p}}^{i*} E_{\mathrm{s}}^{j} E_{\mathrm{s}}^{k} E_{\mathrm{s}}^{l} \mathrm{d}x\mathrm{d}y$ between pump and signal electric field components [104] corresponding to all non-zero susceptibility tensor elements $\chi_{ijkl}^{(3)}$. The electric fields in this calculation are normalized. The non-zero tensor elements are determined by the material crystal structure and orientation.

Our TiO_2 is deposited on a thick thermal oxide and is thus polycrystalline with randomly oriented grains of diameter smaller than 50 nm. The lack of long-range order and the small grain size allows us to treat the material as effectively isotropic.

Using the methods above we typically find an effective interaction area A_{eff} on the order of 10^{-10} m^2 for our TiO_2 waveguides. The details on how to obtain the nonlinear overlaps η_{ijkl} are given in Appendix 6.8.

We calculate the effective nonlinearity γ in Eq. (6.4) for a pump and signal mode pair using mode profiles calculated with a commercial finite-difference eigenmode solver [108]. Because a significant part of the field in nanoscale waveguides is evanescent, we must consider the components of the mode profile that are in the waveguide core and cladding independently and utilize the corresponding nonlinear tensors.

Direct measurements of $\chi^{(3)}$ are difficult because of multi-photon absorption and other competing nonlinear interactions, especially at photon wavelengths below the half band gap; therefore, we use the nonlinear index [12]

$$n_2 = \frac{3\chi^{(3)}}{4n_0^2\epsilon_0 c} \tag{6.5}$$

to parameterize the magnitude of the third-order nonlinearity. We use the value $n_2 = 4.65 \times 10^{-19}$ m^2/W for the TiO_2 nonlinearity at 532 nm. This value is obtained from the bandgap scaling of $n_2(\lambda)$ [109] (see Appendix 6.8 for details).

6.4.3 Triplet generation rate in lossy waveguides

The rate of direct generation of photon triplets R_3 from TOSPDC in the absence of photon losses has been calculated in previous work [100, 104]. Findings in Refs. [100, 104] can be qualitatively summarized by the expression $R_3 \approx \tilde{\zeta}\, N_p(0)\, L$, where $N_p(0)$ is the number of pump photons entering the waveguide and $\tilde{\zeta} \propto \gamma^2$ is the conversion efficiency per unit length, and L the waveguide length.

In the presence of photon losses, the triplet generation rate no longer increases linearly with L. We account for scattering losses by introducing pump and signal intensity attenuation coefficients α_{p} and α_{s}, respectively. We emphasize that an optimal length L_{opt} must exist such that the waveguide is long enough to generate a large number of triplets, but short enough so that a large fraction of complete triplets reaches the end when losses are taken into consideration. Extending the analysis in Ref. [104], we can express the triplet generation rate R_3 in the presence of losses for a continuous wave (cw) pump as (derivation in Appendix 6.9)

$$R_3 = \frac{2^2\,3^2\,\hbar c^3 n_{\mathrm{p}}^3}{\pi^2[\omega_{\mathrm{p}}^0]^2}\gamma^2 L^2 P\left(\frac{\omega_0}{n_0^2(\omega)}g(\omega_0)\right)^3 e^{-(\alpha_{\mathrm{p}}+3\alpha_{\mathrm{s}})L/2} \quad \iint_{-\infty}^{\infty} d\nu_{\mathrm{r}}\, d\nu_{\mathrm{s}} |\Phi(\nu_{\mathrm{r}},\nu_{\mathrm{s}})|^2\,, \tag{6.6}$$

where the spectral amplitude $\Phi(\nu_{\mathrm{r}},\nu_{\mathrm{s}})$ is defined in Appendix 6.9 in terms of the frequency-dependent phase mismatch $\Delta k(\nu_{\mathrm{r}},\nu_{\mathrm{s}})$ and a loss mismatch parameter $\Delta\alpha = (\alpha_{\mathrm{p}} - 3\alpha_{\mathrm{s}})$. P is the pump power and $\omega_0 = \omega_{\mathrm{p}}^0/3$. The integration variables ν_{r} and ν_{s} are signal detunings from $\omega_{\mathrm{p}}^0/3$.

We can compare the triplet generation rate from Eq. (6.6), which takes into account the dispersion properties of the signal mode around the phase matching point, with a simplified expression that ignores dispersion (derivation in Appendix 6.9)

$$N_3 \equiv \int_0^L z\,\frac{\mathrm{d}N_3(z)}{\mathrm{d}z} = \tilde{\zeta}\frac{N_{\mathrm{p0}}}{\alpha_{\mathrm{p}} - 3\alpha_{\mathrm{s}}}\left(e^{-3\alpha_{\mathrm{s}}\,L} - e^{-\alpha_{\mathrm{p}}\,L}\right), \tag{6.7}$$

where $\tilde{\zeta}$ quantifies the conversion efficiency. The device length that optimizes N_3 is thus given by $L_{\mathrm{opt}} = \left[1/(\alpha_{\mathrm{p}} - 3\,\alpha_{\mathrm{s}})\right]\ln\left(\alpha_{\mathrm{p}}/3\,\alpha_{\mathrm{s}}\right)$, for $\Delta\alpha = (\alpha_{\mathrm{p}} - 3\alpha_{\mathrm{s}}) \neq 0$.

In Figure 6.3a, we plot the normalized signal intensity in the waveguide as a function of the waveguide length L, for different amounts of photon loss in TiO_2

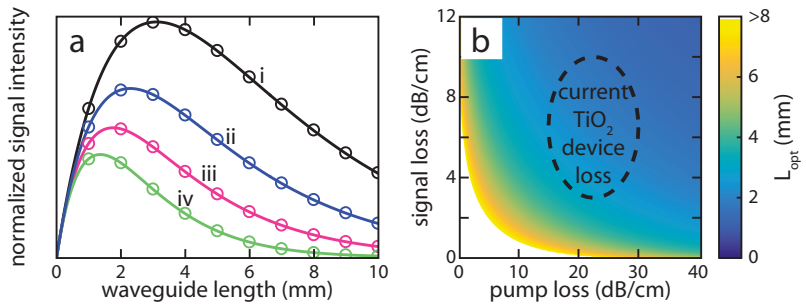

Figure 6.3: (*a*) Signal intensity as a function of device length for pump and signal loss values, respectively, of (*i*) 16 and 4 dB/cm, (*ii*) 16 and 12 dB/cm, (*iii*) 28 and 4 dB/cm, and (*iv*) 28 and 12 db/cm, representing losses on the lower and upper extremes for TiO_2 devices. Circles show the full quantum prediction, including signal dispersion, from Eq. (6.6) and lines show the prediction from Eq. (6.7). All curves are normalized by the maximum signal. (*b*) Ideal waveguide length plotted as a function of pump and signal losses. Current polycrystalline anatase TiO_2 waveguide losses give optimal device lengths $L_{\mathrm{opt}} = 1 - 4$ mm. White denotes $L_{\mathrm{opt}} > 8$ mm.

waveguides. The simplified model that ignores dispersion (Eq. (6.7)) is an excellent approximation for the results obtained by integrating the squared spectral amplitude $|\Phi(\nu_{\mathrm{r}}, \nu_{\mathrm{s}})|^2$ (Eq. (6.6)) near points of PPM. In Figure 6.3b, we plot the optimal device length L_{opt}, as a function of the pump and signal loss parameters α_{p} and α_{s}. Highlighted is the parameter region for the waveguides considered in this work.

6.5 Device optimization

For efficient device operation, we maximize the triplet generation rate R_3 in Eq. (6.6). Given an optimal device length L_{opt}, we must thus minimize the phase mismatch Δk for the desired combination of pump and signal frequencies. This will produce narrow-bandwidth photon triplets as shown in Figure 6.2a and 6.2d. We must also maximize the effective nonlinearity γ by choosing a waveguide geometry

that enhances the electric field overlap between pump and signal modes within a material with a high $\chi^{(3)}$ coefficient. We design TiO_2 waveguides with rectangular core geometry that achieve $\gamma = 1100$ $W^{-1}km^{-1}$ while maintaining single mode operation at 1596 nm. In Section 6.5.1 we describe the optimization protocol used and in Section 6.5.2 we verify the design method with a demonstration of THG.

6.5.1 Optimization protocol

We design our devices for $\lambda_p = 532$ nm because high-power pump lasers with narrow bandwidth, high stability, and low cost are readily available at this wavelength. Our design protocol can be extended to other wavelengths and material platforms depending on the desired signal photon wavelength and available pump laser wavelength. Designing for a particular pump wavelength requires precise control of the waveguide dimensions [61, 110, 111].

We illustrate in Figure 6.1b the geometry of our TiO_2 waveguides. The design parameters that can be tuned include: the waveguide core material, bottom cladding or substrate material, top cladding material, waveguide width, waveguide height, etch fraction, and the waveguide sidewall angle (θ). Due to the current state of the art in TiO_2 waveguide fabrication, we focus on fully etched, symmetric waveguide geometries with 90° sidewall angles.

We use a commercial finite-difference eigenmode solver [108] to complete our device design and optimization. For a given device geometry, we calculate all propagating modes and their dispersion properties at λ_p and $3\lambda_p$, using measured materials properties. We then use calculated mode dispersion properties to calculate the phase

mismatch Δk for all mode pairs consisting of visible pump and IR signal. The mode profiles and the $\chi^{(3)}$ nonlinearity of the core and cladding materials are used to calculate the mode overlap and γ for all mode pairs (see Appendix 6.8). This process is repeated for all device geometries to minimize phase mismatch and maximize γ.

We complete a sweep for rectangular waveguides, varying the waveguide height in the range 200 – 400 nm and width in the range 400 – 600 nm. This range of dimensions is chosen to ensure single mode operation at $3\lambda_{\mathrm{p}}$, meaning only one TE and one TM guiding mode are supported by the waveguide. To quickly assess different waveguide geometries we introduce a figure of merit that describes the effective spectral density of signal photons

$$\mathcal{F} = \frac{\gamma^2}{\delta_{\mathrm{s}}}, \tag{6.8}$$

where the minimum signal bandwidth $\min\{\delta_{\mathrm{s}}\} = \Delta_{\mathrm{PPM}}$ is given by the PPM bandwidth in Eq. (6.1) for degenerate TOSPDC. For each set of waveguide dimensions, we find the mode pair (pump and signal) with the lowest phase mismatch that has non-zero effective nonlinearity. In Figure 6.4, we show the effective nonlinearity γ and figure of merit $\mathcal{F}$ for the best phase matched mode pair with the fundamental IR signal mode, as a function of waveguide dimensions. Regions that are colored in black for the TM signal γ do not support a TM signal mode. Discontinuities in the plots of γ arise when the pump mode with the lowest phase mismatch changes. The regions with high $\mathcal{F}$ in Figure 6.4 are further restricted by the fact that the conversion efficiency drops significantly for negative phase mismatch $\Delta k < 0$ (black regions) because normal dispersion in the signal modes at the signal frequencies makes simultaneous phase matching and energy conservation impossible. Rapid broadening

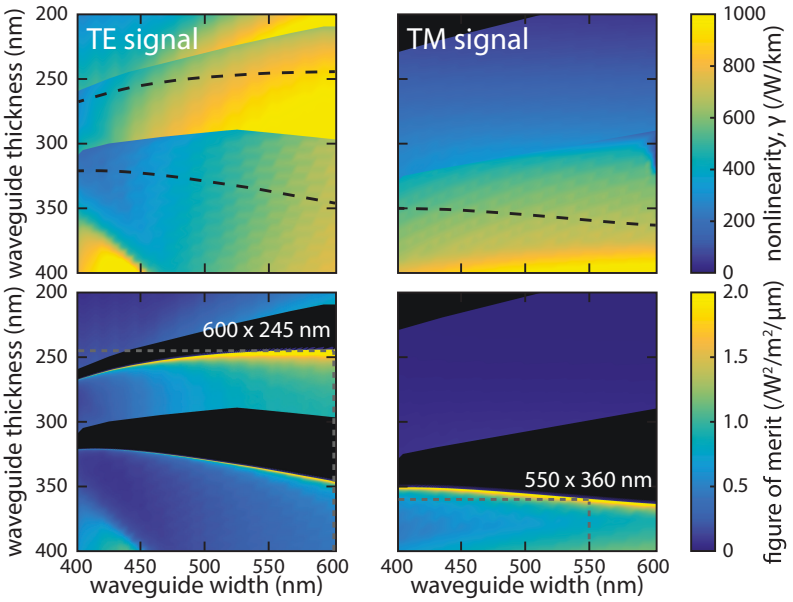

Figure 6.4: (*top*) The effective nonlinearity γ as a function of waveguide width and thickness for the best phase-matching point. The highest $\gamma = 1100$ W^{-1}km^{-1} is achieved in a 600×300 nm waveguide for TE signal and a 600×400 nm waveguide for TM signal. However, these dimensions do not achieve phase-matching. Lines mark regions with high $\mathcal{F}$ which do achieve phase-matching. (*bottom*) Figure of merit $\mathcal{F}$ as a function of waveguide dimensions. The best combination of phase matching and γ are achieved at 600×245 nm ($\gamma = 908$ W^{-1}km^{-1}) for TE signal and 550×360 nm ($\gamma = 674$ W^{-1}km^{-1}) for TM signal.

of the signal spectrum when shifting waveguide dimensions away from regions that achieve PPM greatly reduces $\mathcal{F}$.

We extract the optimal waveguide dimensions using the maximum values of $\mathcal{F}$ (Table 6.1). Choosing a region where a high figure of merit is maintained for a larger range of waveguide dimensions can reduce the negative impacts of fabrication tolerances on device performance in experimental demonstrations. The same figure of merit can be used to optimize other waveguide parameters and geometries.

Table 6.1: **Waveguide parameters for phase-matching regions with high figure of merit $\mathcal{F}$. $\mathbf{e_s}$ is the signal mode polarization and γ the effective nonlinearity.**

$\mathbf{e_s}$	Width (nm)	Thickness (nm)	γ ($W^{-1}km^{-1}$)	Δ_{PPM} (μm)	$\mathcal{F}$ ($W^{-2}m^{-2}\mu m^{-1}$)
TE	400 – 600	268 – 245	291 – 908	0.046 – 0.051	1.81 – 16.2
TE	400 – 600	322 – 346	233 – 718	0.044 – 0.062	1.22 – 11.6
TM	400 – 600	351 – 364	522 – 671	0.044 – 0.048	6.19 – 14.0

6.5.2 Experimental validation of the protocol

The reverse process of TOSPDC, THG, has been demonstrated in nanoscale polycrystalline anatase TiO_2 waveguides by Evans *et al.* [61]. Because the same energy conservation, phase matching and mode overlap constraints govern both processes, we perform similar experimental validation of our design methods by means of THG measurements.

The waveguide (780×244 nm) is designed to have multiple phase-match points within the TE-polarized pump bandwidth. Using the techniques from Sections 6.4.1 and 6.4.2, we calculate phase match points with $\gamma = 253$ and 304 $W^{-1}km^{-1}$ at 513.3 and 523.0 nm, respectively. In Figure 6.5, we plot the expected relative intensities of THG based on the measured input pump spectrum, calculated mode dispersion, and calculated γ of both mode pairs, showing close agreement with experimental results. The experimental phase-match points are within 1.5 nm of the calculated phase match points and the measured THG signal is broader by approximately 3 nm. This can be explained by variations in waveguide width of ± 5 nm and thickness of ± 2 nm along the length of the waveguide. These variations are within the measured fabrication

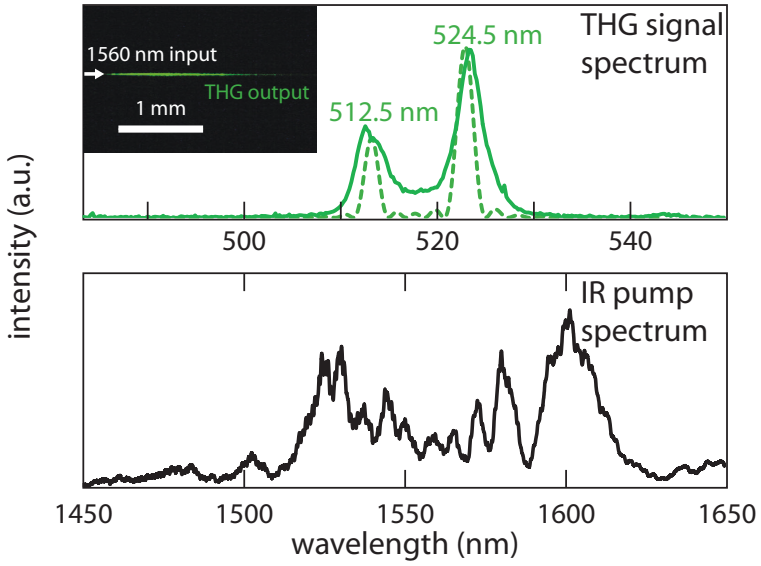

Figure 6.5: Experimental demonstration of THG in an integrated waveguide with two phase-matching points within the infrared pump bandwidth (black curve). The calculated THG signal (dashed curve) shows agreement with the measured THG signal (solid green curve). The inset shows a top-down image of scattered THG signal from the waveguide.

tolerances of waveguide width and roughness of the film used to fabricate the device. This demonstration experimentally shows that the device design methods outlined in this paper can be used to optimize devices for THG and, consequently, TOSPDC.

6.5.3 Realistic device performance

Combining the results of the design sweeps presented in Figures 6.3 and 6.4 with measured losses, we estimate TOSPDC device performance. We have previously measured losses as low as 4 dB/cm in polycrystalline anatase TiO_2 waveguides in the telecommunications wavelengths [**?**, 62] and estimate losses of 20–30 dB/cm at 532 nm. With this amount of losses, the optimal device length is $L_{\text{opt}} = 2.2 - 2.8$ mm. We estimate a photon triplet conversion efficiency of 0.1 – 0.13 triplets/s/mW of pump power and maximum generation rate of 130 – 160 triplets/s. This rate takes into account an optimal end-fire coupling efficiency of 20.6% calculated for the 550 × 360 nm waveguide and higher-order pump mode described in Figure 6.1 and an input pump power of 1250 mW at 532 nm, corresponding to the measured damage threshold of our TiO_2 devices. We note that the TE signal phase-matching point in a 600 × 245 nm waveguide does have a higher γ, however, the photon triplet generation rate would be lower due to a maximum end-fire coupling efficiency of only 10.5% into the higher-order pump mode. We use a nonlinear index of $n_2 = 4.65 \times 10^{-19}$ m^2/W. Film losses as low as 3 dB/cm in the telecommunications wavelengths and 15 dB/cm in the visible wavelengths have been measured using prism coupling techniques [**?**]. By optimizing the fabrication, we can reduce losses to the limit of the film losses, increasing the optimal device length to 3.7 mm and the maximum triplet

generation efficiency to 0.17 triplets/s/mW of pump power, over an order of magnitude higher than previous theoretical and experimental results [97, 98, 104, 105, 112]. This highlights the importance of reducing photon losses in waveguide-based devices.

6.5.4 Temporal coherence of TOSPDC sources

Second-order spontaneous parametric down conversion (SPDC) generates photon pairs that possess quantum correlations in energy and time degrees of freedom. This energy-time entanglement can be exploited in quantum communication protocols [113, 114]. Our TOSPDC sources are expected to exhibit tripartite energy-time entanglement. However, the type of encoding of quantum information that can be exploited for quantum communication protocols with our source ultimately depends on the spectral and temporal coherence properties of the down-converted signal [115]. In this section we therefore discuss the coherence properties of TOSPDC sources for realistic detector and loss parameters.

The temporal coherence of a triplet source can be characterized in three-photon coincidence detection experiments, which gives access to the third-order intensity correlation function [100]

$$G^{(3)}(x_1, x_2, x_3) = \langle E^{(-)}(x_1)E^{(-)}(x_2)E^{(-)}(x_3)E^{(+)}(x_3)E^{(+)}(x_2)E^{(+)}(x_1)\rangle, \qquad (6.9)$$

where $\hat{E}^{(+)}(x_j)$ is an operator describing the propagating electric field at the j-th detector, with $\hat{E}^{(-)} = [\hat{E}^{(+)}]^{\dagger}$. The field at the detector is given by a wavepacket of the form $\hat{E}^{(+)}(x_j) = \int d\omega f_j(\omega)\hat{a}(\omega)\exp[-i\omega x_j]$, where $\hat{a}(\omega)$ is a free-space bosonic operator. We assume a Gaussian detector filter function $f_j(\omega) = f_0\exp[-(\omega-\omega_j)^2/2\sigma_j^2]$ [92]. f_0 is a normalization constant and ω_j is the center frequency of the j-th spectral filter.

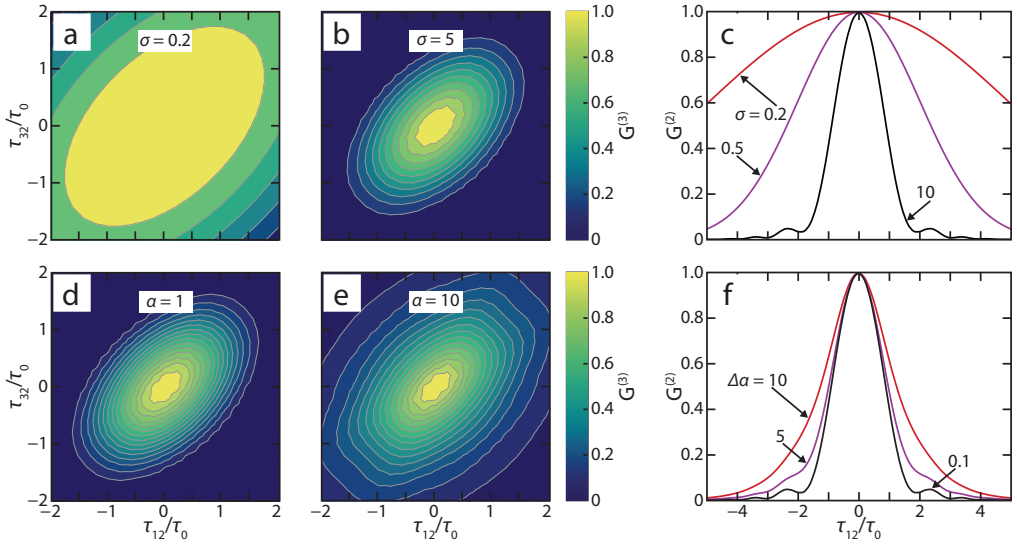

Figure 6.6: Triple and two-photon coincidence signals, for detectors placed at equal distance from the TOSPDC output. Time delays $\tau_{12} = t_1 - t_2$ and $\tau_{32} = t_3 - t_2$ are given in units of the characteristic timescale $\tau_0 = \sqrt{D_s\, L/2}$. Panels (a) and (b) are $G^{(3)}$ functions for the detector filter bandwidths $\sigma = 0.2\nu_0$ and $\sigma = 5\nu_0$, respectively, with a loss mismatch parameter $\Delta\alpha\, L \equiv (\alpha_{\rm p} - 3\alpha_{\rm s})\, L = 0.1$. Panels (d) and (e) correspond to the $G^{(3)}$ functions for $\Delta\alpha\, L = 1$ and $\Delta\alpha\, L = 10$, respectively, with a detector bandwidth $\sigma = 5\nu_0$. Panel (c) is the $G^{(2)}$ function for several values of σ with fixed $\Delta\alpha\, L = 0.1$ and (f) is the $G^{(2)}$ signal for several values of $\Delta\alpha\, L$ with fixed $\sigma = 5\nu_0$. Frequency is in units of $\nu_0 = 1/\tau_0$, L is the waveguide length and D_s is the group velocity dispersion (GVD) of the signal guiding mode. Plots are normalized to their maximum values.

For simplicity, we assume that all filters have the same bandwidth $\sigma_k = \sigma$.

The $G^{(3)}(x_1, x_2, x_3)$ correlation function is proportional to the probability of detecting a photon at the space-time location $x_1 = t_1 - r_1/c$, followed by a detection event at location $x_2 = t_2 - r_2/c$ and another one at $x_3 = t_3 - r_3/c$. In this notation, the j-th detector fires at time t_j at a distance r_j from the TOSPDC output. This triple coincidence signal can be computed for an output triplet state $|\Psi_3\rangle$ as

$$G^{(3)}(x_1, x_2, x_3) = |\, \langle 0|\, E^{(+)}(x_3) E^{(+)}(x_2) E^{(+)}(x_1)\, |\Psi_3\rangle\, |^2. \tag{6.10}$$

We are interested in $G^{(3)}$ for a triplet state generated by a narrow band cw pump near the perfect phase matching point (PPM), defined in Section 6.4.1. For a pump photon with fixed frequency ω_p^0 and wavenumber k_p^0, the triplet state $|\Psi_3\rangle$ is a continuous wavepacket describing three signal photons having frequencies $(\omega_\mathrm{r}, \omega_\mathrm{s}, \omega_\mathrm{i})$ that satisfy energy and momentum conservation. The triplet wavepacket is characterized by a joint spectral amplitude function $\Phi(\omega_\mathrm{r}, \omega_\mathrm{s}, \omega_\mathrm{i})$, whose imaginary part depends on the amount of pump and signal losses. We refer the reader to Appendix 6.9 for more details on this point. Signal photon frequencies that are detuned from the PPM point, lead to a phase mismatch $\Delta k \neq 0$. For the triplet state $|\Psi_3\rangle$ described in Appendix 6.9, we numerically evaluate the $G^{(3)}$ function by expanding the frequency mismatch Δk up to second order in signal detunings from PPM.

In Figure 6.6 we plot the computed $G^{(3)}$ signals with time delays in units of the timescale $\tau_0 = \sqrt{D_\mathrm{s}\, L/2}$, where L is the waveguide length and D_s is the group velocity dispersion (GVD) of the signal guiding mode. For a typical optimized TiO_2 waveguide with $L = 2$ mm and $D_s = 5.36 \times 10^{-3}$ ps^2/mm, the characteristic coherence time is $\tau_0 = 73$ fs. The signal depends on the bandwidth σ of the detectors, given here in units of $1/\tau_0$, as well as the loss mismatch parameter $\Delta\alpha \equiv (\alpha_\mathrm{p} - 3\alpha_\mathrm{s})$, which characterizes the frequency-time decoherence of the triphoton state. For our 2 mm long waveguides, we have a small loss mismatch $\Delta\alpha\, L \approx 0.08$. The mirror symmetry around $\tau_{12} = \tau_{32}$ is due to the fact that all photons in a triplet have the same GVD in mode-degenerate TOSPDC. The FHWM of the $G^{(3)}$ function along the cut $\tau_{12} = -\tau_{32}$ is roughly equals to τ_0 for large detector bandwidths $\sigma\tau_0 \gg 1$. Small bandwidths $\sigma\tau_0 \ll 1$ broaden the $G^{(3)}$ function such that highly correlated photons can be detected within a wide

range of time delays. This behaviour resembles the two-photon coincidence signals for second-order SPDC sources [92]. Increasing the loss mismatch $\Delta\alpha$ also broadens the $G^{(3)}$ function, but in a qualitatively different way. Photon losses directly broaden the joint spectral amplitude $\Phi(\omega_{\mathrm{r}}, \omega_{\mathrm{s}}, \omega_{\mathrm{i}})$, which characterizes the wavepacket structure of the triplet state $|\Psi_3\rangle$ in the frequency domain. This broadening is independent of the time-domain field representation of $|\Psi_3\rangle$ at the detectors, the so-called triphoton wavepacket $\psi(x_1, x_2, x_3) \equiv \langle 0| E^{(+)}(x_3)E^{(+)}(x_2)E^{(+)}(x_1) |\Psi_3\rangle$, which involves shaping the triplet state $|\Psi_3\rangle$ by the detector filters.

We finally consider a scenario where only two photons of the TOSPDC source are detected in coincidence measurements. In other words, we discard the information about the third photon. The resulting coincidence signal is proportional to the correlation function $G^{(2)}(x_1, x_2)$, the second order analogue of $G^{(3)}$. For the TOSPDC triplet state $|\Psi_3\rangle$, this signal can be written as

$$G^{(2)}(x_1, x_2) \;=\; \int d\omega_3 |\, \langle 0| \, a(\omega_3)E^{(+)}(x_2)E^{(+)}(x_1) \, |\Psi_3\rangle \, |^2. \tag{6.11}$$

We compute the $G^{(2)}$ correlation function as described in Appendix 6.10 for a source pumped at the PPM point, for several values of the detector bandwidth σ and loss mismatch $\Delta\alpha$. The results are shown in Figure 6.6 (panels c and f). The two-photon correlation function has qualitatively the same behaviour as the the $G^{(3)}$ function with σ and $\Delta\alpha$. Its width is also on the order of $1/\tau_0$ for $\sigma\tau_0 \gg 1$. These results show that unlike an SPDC process, where detection of one photon in a photon pair destroys any useful entanglement [92], frequency-time entanglement in a TOSPDC source is robust against single photon losses [116].

6.6 Conclusion and outlook

We provide design principles for practical on-chip sources of photon triplets generated via TOSPDC and discuss the non-unitary propagation of the photon triplet state in the presence of pump and signal photon losses. Including the impact of losses is critical, especially when operating at visible wavelengths where surface roughness and fabrication imperfections are closer to the size of a single wavelength and material absorption increases close to the band edge of the waveguide core material. The design methods discussed in this work can be applied broadly to various device geometries, loss conditions, and material platforms. This will facilitate experimental demonstrations of spontaneously generated photon triplets and development of a platform for commercially viable sources.

We use TiO_2 to illustrate our design protocol. TiO_2 is a promising material platform for an integrated entangled photon triplet source due to its transparency across the visible and telecommunication wavelengths as well as its high linear and nonlinear refractive indices. We discuss the mean signal flux and prospects for detecting continuous-variable entanglement of the photon triplet quantum state in the presence of photon loss. We calculate triplet generation rates on the order of 10^{-1} triplets/s/mW of pump power, which exceeds the triplet generation efficiencies obtained by cascading entangled photon pairs by an order of magnitude. Our work thus sets the stage for the development of on-chip photon triplet sources for applications in photonic quantum technologies.

Improvements to the proposed waveguide design and current fabrication techniques can greatly enhance generation rates and accelerate experimental efforts. Gen-

erating photon triplets within an integrated micro-ring resonator or resonant cavity can provide an additional constraint on the spectrum of generated photons, enabling greater spectral control of the output signal via the Purcell effect. Optimization of fabrication processes, including resist reflow techniques and new etchless fabrication techniques [117], can reduce waveguide losses. Photonic crystals and slot waveguides can be used to greatly enhance the effective nonlinearity of integrated photonic devices [118].

Device performance can also benefit from improvements in material deposition. Film optimization through epitaxial growth has the potential to dramatically reduce scattering losses due to grain boundaries, increasing the achievable optimal device length and conversion efficiency. Rutile TiO_2 is unexplored as a photonic device platform although other studies have shown extraordinarily high nonlinearity at visible wavelengths in this material [119]. Alternatively, exploring other material platforms, for example silicon nitride or diamond, may enable better devices despite their lower nonlinearity due to the trade-offs between propagation losses, nonlinearity, and damage threshold.

Several experimental considerations need to be taken into account for successful measurements of photon triplets. Although a pulsed pump would enable gated detection schemes important for many applications, competing intensity-dependent nonlinear interactions, such as multi-photon absorption and self- and cross-phase modulation, would limit the usable pulse energy and attainable photon triplet generation rate. Secondly, spectral filtering at the device output is necessary to reduce noise from residual pump photons. Lastly, as in all experimental demonstrations, the

rate of detected photon triplets is lower than the generated rate due to losses at the device output, detector efficiency, and the detection scheme for measuring 3-photon coincidences. These factors, coupled with the required fabrication precision for realizing an efficient device, highlight the challenges associated with an experimental demonstration.

In summary, we have developed a design protocol to optimize the efficiency of TOSPDC in nanoscale waveguides. We illustrate the scheme using TiO_2 photonic chips, but the method is general and can be applied to any material platform. Entangled photon triplets generated this way can find applications in quantum tasks that can benefit from states with non-Gaussian quantum statistics, serve as a starting point to build large entangled states of light for quantum information purposes, or to develop novel spectroscopic tools.

Funding Information

We acknowledge support from the NSF Division of Physics under contract PHY-1415236, the Harvard Quantum Optics Center, the Natural Sciences and Engineering Research Council of Canada, the NSF Graduate Research Fellowship Program (DGE1144152), and Harvard CNS. FH thanks support from DTRA HDTRA 1-100109946 and the CONICYT programs PAI 79140030 and Iniciación 11140158. CCE acknowledges support from the Kavli Institute at Cornell for Nanoscale Science.

Acknowledgments

*MGM and FH are co-first authors of the manuscript. CCE proposed to use TiO_2 for TOSPDC. MGM, CCE, FH and OR developed the description of phase matching in integrated devices. MGM, SG-N and OR developed the mode overlap calculations and device design methods. OR fabricated waveguides and MGM, SG-N, and OR completed measurements of THG. FH and GGG developed the quantum theory of lossy TOSPDC. FH performed stochastic wavefunction simulations and derived the entanglement witness for non-degenerate TOSPDC. EM and AA-G supervised the research and manuscript preparation. All authors approved the final copy of the manuscript. Benjamin Franta and Philip Muñoz provided feedback on the manuscript throughout its development.

6.7 Appendix 1 - Signal bandwidth for mode-degenerate TOSPDC

In this Appendix we derive Eq. (2) of the main manuscript, for the signal bandwidth Δ_{s}. We expand the signal and pump wavenumbers around the perfect phase-matching (PPM) point. We allow the signal and pump frequencies to be detuned from this crossing by the quantities $\Delta_m = \omega_m - \omega_{\mathrm{p}}^0/3$ with $m = \{\mathrm{s}, \mathrm{r}, \mathrm{i}\}$. The phase-matching condition at the PPM point reads $k_{\mathrm{p}}^0 = 3k_{\mathrm{s}}^0$. Expanding the pump and signal wavenumbers around PPM with respect to the pump and signal detunings, the

condition $(k_\mathrm{p} - k_\mathrm{s} - k_\mathrm{r} - k_\mathrm{i}) = 0$ yields

$$\left(\Delta_\mathrm{s}^2 + \Delta_\mathrm{r}^2 + \Delta_\mathrm{i}^2\right) = \frac{2\left(v_\mathrm{p}^{-1} - v_\mathrm{s}^{-1}\right)}{D_\mathrm{s}}\Delta_\mathrm{p} + \left(\frac{D_\mathrm{p}}{D_\mathrm{s}}\right)\Delta_\mathrm{p}^2 \equiv r_\mathrm{p}^2 \tag{6.12}$$

where $v_m \equiv d\omega_m/dk_\mathrm{p}$ and $D_m \equiv d^2k_m/d\omega_m^2$ are the mode group velocity and group velocity dispersion (GVD) of the m-th photon at the PPM point. Because the three signal photons belong to the same guided mode, they have the same values of v_s and D_s, defined at $\omega_\mathrm{p}^0/3$.

We use energy conservation to simplify the linear terms with respect to the signal detunings. Eq. (6.12) shows that for mode-degenerate and frequency non-degenerate TOSPDC, phase matching can be satisfied by the signal detunings Δ_m that lie on the surface of a sphere with radius r_p, subject to the linear constraint $\Delta_\mathrm{p} = \Delta_\mathrm{s} + \Delta_\mathrm{r} + \Delta_\mathrm{i}$, due to energy conservation. We define dimensionless signal detunings $x_m = \Delta_m/\Delta_\mathrm{p}$, for $m = \{\mathrm{r}, \mathrm{s}\}$, and the parameter $a_\mathrm{p} = r_\mathrm{p}^2/(2\Delta_\mathrm{p}^2) - 1$ (in Eq. 6.3 we use $A_\mathrm{p} = a_\mathrm{p}\Delta_\mathrm{p}^2$). The points satisfying both energy and momentum conservation form the ellipse

$$x_\mathrm{s}^2 + x_\mathrm{r}^2 - x_\mathrm{r}x_\mathrm{s} - x_\mathrm{r} - x_\mathrm{s} = a_\mathrm{p}. \tag{6.13}$$

The signal bandwidth is therefore given by the distance between the critical points $x_\mathrm{s} = 1 \pm \sqrt{(1 + a_\mathrm{p})/3}$. Inserting the expression for a_p and inserting the original frequency variables we can write the signal bandwidth as

$$\delta_\mathrm{s} \equiv \sqrt{\frac{2}{3}} \times 2\, r_\mathrm{p} = 2\left(\frac{2}{3}\right)^{1/2}\left[\frac{2\left(v_\mathrm{p}^{-1} - v_\mathrm{s}^{-1}\right)}{D_\mathrm{s}}\Delta_\mathrm{p} + \left(\frac{D_\mathrm{p}}{D_\mathrm{s}}\right)\Delta_\mathrm{p}^2\right]^{1/2}, \tag{6.14}$$

which exhibits a crossover in the scaling $(\Delta_\mathrm{p})^\alpha$ from $\alpha = 1/2$ to $\alpha = 1$ roughly at the pump detuning $|\Delta_\mathrm{p}| = 2|v_\mathrm{s} - v_\mathrm{p}|/(v_\mathrm{s}v_\mathrm{p}D_\mathrm{p})$.

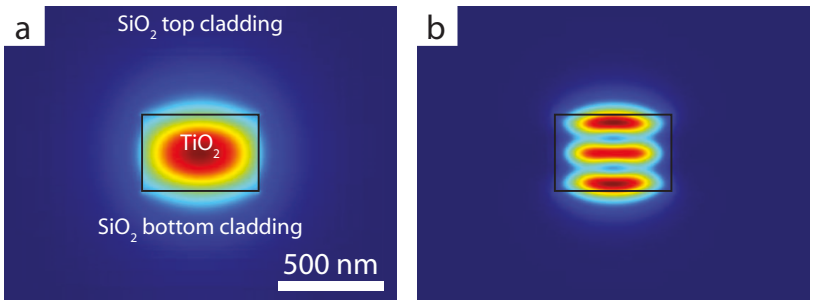

Figure 6.7: Examples of (a) a signal mode power density profile and (b) pump mode power density profile. These mode profiles are for a TM_{00} signal mode and TM_{02} pump mode phase matched at 532 nm in a 550 × 360 nm TiO_2 waveguide with SiO_2 cladding (first presented in Figure 6.1 of the main text).

6.8 Appendix 2 - Overlap calculation with nonlinear susceptibility tensor elements

In this Appendix, we provide a generalized method of calculating overlap η and effective nonlinearity γ that can be applied to any crystal symmetry and orientation, as well as a derivation of the symmetry conditions that apply in polycrystalline anatase TiO_2. We calculate the effective nonlinearity of TOSPDC for phase-matched pump and signal modes using the definition

$$\gamma = \frac{3\chi^{(3)}\omega_{\mathrm{p}}}{4\epsilon_0 c^2 n^2}\eta\,, \tag{6.15}$$

where n is the material index, $\chi^{(3)}$ is the nonlinear susceptibility and η is the overlap between the modes. Crystal symmetry is taken into account to determine relative magnitudes of $\chi^{(3)}$ tensor elements. We discuss considerations relevant to determining the strength of the nonlinearity at the pump wavelength.

The overlap between phase-matched pump and signal modes propagating along the z-direction is calculated using the x, y, z electric field components of each mode

as

$$\eta_{ijkl} = \frac{\iint \mathrm{d}x\mathrm{d}y \; E_{\mathrm{p}}^{i*} \, E_{\mathrm{s}}^{j} \, E_{\mathrm{s}}^{k} \, E_{\mathrm{s}}^{l}}{\left[\iint \left|E_{\mathrm{p}}(x,y)\right|^2 \mathrm{d}x\mathrm{d}y\right]^{1/2} \left[\iint \left|E_{\mathrm{s}}(x,y)\right|^2 \mathrm{d}x\mathrm{d}y\right]^{3/2}}, \tag{6.16}$$

where $E_{\mathrm{p}}^{i}(x,y)$ and $E_{\mathrm{s}}^{j}(x,y)$ are the components of the pump and signal mode electric fields. The denominator in Eq. (6.16) normalizes the pump and signal fields such that they satisfy the condition $\iint |E|^2 \, \mathrm{d}x\mathrm{d}y = 1$. Figure 6.7 gives an example of a pair of modes with non-zero overlap.

Spatial distributions of the x, y, z E-field components of each mode in Eq. (6.16) are calculated using simulations [108]. The subscripts i, j, k, l correspond to the Cartesian indices for crystal axes along which the E-field is polarized. In our notation, the first index refers to the pump polarization and the subsequent three indices refer to the polarization of the signal modes. In the degenerate TOSPDC case, all three signal modes have the same E-field distribution.

To illustrate the calculation of overlap terms for a specific $\chi^{(3)}$ tensor element, we first consider the simplest case of an E-field and a single crystal oriented along the same axes (Figure 6.8a and 6.8b). We use indices x, y, z for the E-field coordinate axes and i, j, k, l for the crystal axes. In this case, the χ_{iijj} contribution to the TOSPDC process is determined by the field overlap component $\eta_{iijj} = \iint E_p^{x*} E_s^x E_s^y E_s^y \mathrm{d}x\mathrm{d}y$. For the same electric field orientation but a different crystal orientation shown in Figure 6.8c, the contribution of the χ_{iijj} term is calculated by projecting the E-field onto the crystal axes, such that *e.g.* $E_i = E_x \cos\theta + E_y \sin\theta$ and $E_j = -E_x \sin\theta + E_y \cos\theta$ and $E_k = E_z$, and then computing $\eta_{iijj} = \iint E_p^{i*} E_s^i E_s^j E_s^j \mathrm{d}x\mathrm{d}y$. Because the crystal symmetry determines the nonlinearity, projecting the E-field onto the crystal axes allows us to calculate the total nonlinear overlap with the fewest number of

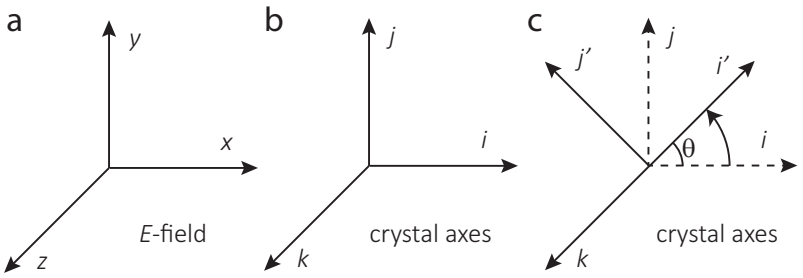

Figure 6.8: Examples of a) E-field orientation, b) crystal axes orientation and c) crystal axes orientation with a rotation by an arbitrary angle in the xy plane.

unique terms, η_{ijkl}.

There are 81 possible permutations of the field polarizations in the overlap calculation for η_{ijkl}. Their contribution to the total overlap is determined by the magnitude of the corresponding nonlinear susceptibility tensor element, χ_{ijkl}. The material crystal structure of the waveguide determines which χ_{ijkl} terms are non-zero and their relative magnitudes. As an example, anatase TiO_2 has tetragonal symmetry and belongs to the crystal class $4/mmm$. Our anatase TiO_2 films polycrystalline with randomly oriented grains much smaller than the wavelength ($\lambda_s/30$ and $\lambda_p/10$). As a result, an incoming field along the x-direction polarizes the medium along all orthogonal crystal axes. Furthermore, this response is indistinguishable from the polarization of the medium when the incoming field is along y or z. Therefore, we can treat the material as effectively isotropic. The relationships between non-zero isotropic tensor elements can be found in Ref. [12] and are as follows:

$$\begin{gathered} jjkk = kkjj = kkii = iikk = iijj = jjii \;\; ; \;\; jkkj = kjjk = kiik = ikki = ijji = jiij \\ jkjk = kjkj = kiki = ikik = ijij = jiji \;\; ; \;\; iiii = jjjj = kkkk = iijj + ijij + ijji \end{gathered} \tag{6.17}$$

For a material containing large grains with n crystal orientations, the E-field projection can be performed on each of the n crystal axes to identify the overlap terms of interest for each non-zero $\chi^{(3)}$ term. Considering the small grain sizes and the assumption of isotropic crystal symmetry in our waveguide medium, we can significantly simplify this process. The relations in Eq. (6.17) show that there are three independent $\chi^{(3)}$ variables: $iijj$, $ijij$ and $ijji$. Furthermore, when we consider the degenerate TOSPDC case, we find that all three signal modes are the same; therefore, with a given pump index, we can arbitrarily arrange the signal indices and obtain the same overlap:

$$\eta_{iijj} = \eta_{ijij} = \eta_{ijji}. \tag{6.18}$$

This leads to three important conclusions: (i) all overlap terms of interest can be calculated by considering a single crystal axis orientation; (ii) using the relations in Eq. (6.18) we can simplify the number of overlap terms we calculate from 21 to 9 unique terms; and, (iii) we find that $\chi_{iiii} = \chi_{jjjj} = \chi_{kkkk} = 3\chi_{iijj}$, meaning that the contribution of the diagonal nonlinear tensor elements χ_{iiii}, χ_{jjjj} and χ_{kkkk} is three times stronger than the contribution generated by the non-zero off-diagonal terms. Note that there are three times as many off-diagonal $\chi^{(3)}$ terms, so that each of the 9 unique overlap terms makes an equal contribution to the total overlap.

Based on the symmetry of the $\chi^{(3)}$ tensor, we can also gain an intuition for which combinations of mode profiles yield non-zero overlap and contribute to the effective nonlinearity. In the case of polycrystalline TiO_2, each of the x, y, and z components appears an even number of times in each non-zero $\chi^{(3)}$ tensor element. The mode profile of the x, y, and z components of the field must therefore be even, meaning

that sign of E_{x}, E_{y}, and E_{z} is symmetrical about the x and y axes. Alternatively, an even number of odd field profiles must be present to yield non-zero overlap.

Nanoscale waveguides often have a significant evanescent field, requiring that nonlinear overlaps take into account different $\chi^{(3)}$ nonlinearities in the core and cladding regions. In this case, the integration in Eq. (6.16) is carried out over the area of the core, top cladding, and bottom cladding separately. These values are then used to calculate γ in each region separately using Eq. (6.15). The total effective nonlinearity of the waveguide will be the sum $\gamma = \gamma_{\mathrm{core}} + \gamma_{\mathrm{topcladding}} + \gamma_{\mathrm{bottomcladding}}$.

In the main text we note that the $\chi^{(3)}$ nonlinearity is parametrized using the nonlinear index

$$n_2 = \frac{3\chi^{(3)}}{4n_0^2\epsilon_0 c}\,, \tag{6.19}$$

which is often measured using Z-scan and self-phase modulation techniques, both of which also rely on third-order nonlinear interactions. In order to produce photon triplets in the telecommunications band via TOSPDC, the pump wavelength is in the visible. Z-scan and self-phase modulation measurements are challenging in the presence of two-photon absorption and other effects prevalent below the half-bandgap wavelength [119,120]. For this reason, we have applied a bandgap scaling approach of n_2 [109] to nonlinearities measured in polycrystalline anatase TiO_2 films for the range of wavelengths $\lambda = 800 - 1560$ nm [60]. The estimated value of n_2 can be considered as a lower bound because the model in Ref. [109] is known to underestimate the magnitude of the nonlinearity at photon energies above three-quarters of the bandgap. As a result, our calculated nonlinearities for a 532-nm pump wavelength and the corresponding photon triplet generation rates can be considered a lower bound on

expected device performance.

In conclusion, we find the total overlap in polycrystalline anatase TiO_2 by summing 9 unique overlap terms calculated using Eq. (6.16). The effective nonlinearity is calculated, in turn, using the total overlap as an input parameter in Eq. (4) of the main text. Our approach for determining the effective interaction area and effective nonlinearity by assuming that our material has isotropic symmetry can be used for other polycrystalline materials with grains on the order of $\lambda/10$ or smaller. In addition, the general approach describes how to determine the effective nonlinearity for arbitrary crystal symmetries, crystal orientations and electric field orientations.

6.9 Appendix 3 - Triplet generation rate in presence of propagation losses

In this appendix we derive Eqs. (6) and (8) of the main text. We note that the effects of multi-photon absorption are ignored in this analysis and justify this assumption for the waveguide parameters presented in the main text.

We use a formalism that extends the approach in Refs. [100, 104]. The starting point is the expression for the TOSPDC light-matter interaction Hamiltonian

$$\hat{H}_{\mathrm{I}} = \frac{3\epsilon_0 \chi^{(3)}}{4} \int \mathrm{d}V \hat{E}_{\mathrm{p}}^{(+)}(\mathbf{r},t)\hat{E}_{\mathrm{r}}^{(-)}(\mathbf{r},t)\hat{E}_{\mathrm{s}}^{(-)}(\mathbf{r},t)\hat{E}_{\mathrm{i}}^{(-)}(\mathbf{r},t) + \mathrm{H.c.} \tag{6.20}$$

in terms of the electric field operators $\hat{E}^{(+)}(\mathbf{r},t) = iA(x,y)\sqrt{\delta k}\sum_k \ell(\omega)\exp\left[i(kz-\omega t)\right]\hat{a}(t)$, where $\ell(\omega) = \sqrt{\hbar\omega/\pi\epsilon_0 n^2(\omega)}$. ϵ_0 is the vacuum permittivity, $n(\omega)$ the refractive index, and $\hbar$ is Planck's constant. The label p refers to the pump field, and $\{r,s,i\}$ refer to the signal fields. $\delta k = 2\pi/L_Q$ is the mode spacing defined by the quantization

length L_Q, $A(x,y)$ characterizes the transverse spatial distribution of the field, taken to be normalized and frequency-independent.

We describe the pump mode as a strong classical field of the form

$$E_{\rm p}^{(+)}(\mathbf{r},t) = A_0 A_p(x,y) \int {\rm d}\omega_{\rm p} \beta(\omega_{\rm p}) {\rm e}^{[i(k_{\rm p}(\omega_{\rm p})z - \omega_{\rm p} t)]}\,, \tag{6.21}$$

and consider the pump Gaussian amplitude $\beta(\omega_{\rm p}) = 2^{1/4}/(\pi^{1/4}\sqrt{\sigma}){\rm exp}[-(\omega_{\rm p}-\omega_{\rm p}^0)^2/\sigma^2]$ where $\omega_{\rm p}^0$ is the pump carrier frequency and σ the pump pulse bandwidth. In general, A_0 is related to the peak pump power, but for a Gaussian pump amplitude, it is related to the average pump power P by $A_0 = \sqrt{P/\pi\epsilon_0 c n_p R}$, with R the pulse repetition rate and $n_p = n(\omega_{\rm p}^0)$.

In the absence of propagation losses, first-order perturbation theory with respect to the interaction Hamiltonian allows us to write the output signal state as [92]

$$|\Psi\rangle = \left[1 - \frac{i}{\hbar}\int_{t_0}^{t} {\rm d}t'\, H_{\rm I}(t')\right]|0\rangle = |0\rangle + \lambda|\Psi_3\rangle\,. \tag{6.22}$$

The photon triplet state can be written as

$$|\Psi_3\rangle = \int {\rm d}\omega_{\rm p}\, \beta(\omega_{\rm p}) \sum_{k_{\rm s},k_{\rm r},k_{\rm i}} \ell(\omega_{\rm r})\ell(\omega_{\rm s})\ell(\omega_{\rm i}) \left[\int_{t_0}^{t} {\rm d}t' \int {\rm d}z\; \phi(t,z)\; \hat{a}^\dagger(k_{\rm r})\hat{a}^\dagger(k_{\rm s})\hat{a}^\dagger(k_{\rm i})|0\rangle\right], \tag{6.23}$$

where $\omega_m = \omega(k_m)$ for $m = \{{\rm s},{\rm r},{\rm i}\}$. We have defined the frequency-dependent function $\phi(t,z) = \exp[i\,\Delta\omega\, t]\exp[i\,\Delta k\, z]$, where $\Delta k = (k_{\rm p} - k_{\rm r} - k_{\rm s} - k_{\rm i})$ is the phase mismatch and $\Delta\omega = (\omega_{\rm r} + \omega_{\rm s} + \omega_{\rm i} - \omega_p)$ the energy mismatch. The spatial integration is carried out over the waveguide length L. The photon triplet state amplitude λ is given by

$$\lambda = \frac{3\epsilon_0 \chi^{(3)} A_0}{4\hbar A_{\rm eff}}\,(\delta k)^{3/2}, \tag{6.24}$$

where the effective area is the inverse of η given in Eq. (6.16).

In order to include the propagation losses, we model them phenomenologically through an exponential decay of the pump and signal fields. This approach ignores the probability of observing signal modes with one or two photons as a result of photon scattering. Such conditional states are highly unlikely to occur because the signal modes are found in the vacuum $|0\rangle$ with a near unit probability because $\lambda \ll 1$. We are interested in the part of the output state that involves three photons. If the interaction takes place at position z within a waveguide that spans $z = [-L/2, L/2]$, the corresponding amplitude is decreased by a factor: $e^{-(\alpha_\mathrm{p}/2)(z+L/2)}\, e^{-3(\alpha_\mathrm{s}/2)(L/2-z)}$, where we have used the attenuation coefficients α_p and α_s (in units of inverse length) to describe pump and signal photon loss, respectively. Therefore, the photon triplet state in Eq. (6.23) needs to be modified in the presence of photon losses to read

$$\begin{aligned} |\Psi_3\rangle \;=\; & \int \mathrm{d}\omega_\mathrm{p}\, \beta(\omega_\mathrm{p}) \sum_{k_\mathrm{r},k_\mathrm{s},k_\mathrm{i}} \ell(\omega_\mathrm{r})\ell(\omega_\mathrm{s})\ell(\omega_\mathrm{i}) \\ & \times \left[\int_{t_0}^{t} \mathrm{d}t' \int \mathrm{d}z\; \phi(t',z) e^{-(\alpha_\mathrm{p}-3\alpha_\mathrm{s})z/2} \mathrm{e}^{-(\alpha_\mathrm{p}+3\alpha_\mathrm{s})L/4} \times\; \hat{a}^\dagger(k_\mathrm{r})\hat{a}^\dagger(k_\mathrm{s})\hat{a}^\dagger(k_\mathrm{i})|0\rangle\right] \end{aligned} \tag{6.25}$$

Because the propagation times inside the waveguide are much longer than $1/\Delta\omega$, we carry out the time integration by setting $t_0 = -\infty$ and $t = \infty$ and obtain the energy conservation rule $\int_{-\infty}^{\infty} \mathrm{d}t'\, \phi(z,t) = 2\pi \mathrm{e}^{i\Delta k z}\, \delta(\omega_\mathrm{p} - \omega_\mathrm{r} - \omega_\mathrm{s} - \omega_\mathrm{i})$. Carrying out the spatial integration including the loss terms, imposes the phase-matching condition associated to momentum conservation, which gives the triplet state

$$|\Psi_3\rangle = \left(\frac{2\pi\lambda L}{(\delta k)^3}\right) e^{-(\alpha_\mathrm{p}+3\alpha_\mathrm{s})L/4} \sum_{k_\mathrm{r}} \sum_{k_\mathrm{s}} \sum_{k_\mathrm{i}} \Phi(\omega_\mathrm{r},\omega_\mathrm{s},\omega_\mathrm{i})\, \hat{a}^\dagger(\omega_\mathrm{r})\hat{a}^\dagger(\omega_\mathrm{s})\hat{a}^\dagger(\omega_\mathrm{i})|0\rangle, \tag{6.26}$$

where the condition $\omega_\mathrm{p} = \omega_\mathrm{r} + \omega_\mathrm{s} + \omega_\mathrm{i}$ holds. We have defined the spectral amplitude

function

$$\Phi(\omega_{\rm r},\omega_{\rm s},\omega_{\rm i}) = \beta(\omega_{\rm p})\ell(\omega_{\rm r})\ell(\omega_{\rm s})\ell(\omega_{\rm i})\,\mathrm{sinc}[\{\Delta k + i\Delta\alpha\}L/4], \tag{6.27}$$

where the function $\mathrm{sinc}(x) = \sin(x)/x$ is highly peaked at $x = 0$. We have defined the loss mismatch $\Delta\alpha = (\alpha_{\rm p} - 3\alpha_{\rm s})$.

The signal intensity outside the waveguide is proportional to the expectation value $\langle\Psi_3|\hat{E}^{(-)}(t)\hat{E}^{(+)}(t)|\Psi_3\rangle$, with electric field operator $\hat{E}^{(+)}(t) \propto i\sqrt{\delta k}\sum_k \ell(\omega)\exp[i\omega t]\hat{a}(k)$, that includes all possible wavevectors k. The detected intensity must be averaged over a specific time interval. The Fourier components of the intensity sum up separately. Since the signal intensity is proportional to the number of photons, we have $N_3 \propto \langle\Psi_3|\sum_k \hat{a}^\dagger(k)\hat{a}(k)|\Psi_3\rangle$. Accordingly, the number of triplets per second (generalizing Eq. (19) in Ref. [104]) can be written as

$$\begin{aligned} R_3 &= R\langle\Psi_3|\sum_k \hat{a}^\dagger(k)\hat{a}(k)|\Psi_3\rangle \qquad (6.28)\\ &= R\,\frac{(2\pi\lambda L)^2(3^2)}{\delta k^3}e^{-(\alpha_{\rm p}+3\alpha_{\rm s})L/2}\iiint_{-\infty}^{\infty}\mathrm{d}\omega_{\rm r}\,\mathrm{d}\omega_{\rm s}\,\mathrm{d}\omega_{\rm i}\,g(\omega_{\rm r})g(\omega_{\rm s})g(\omega_{\rm i})|\Phi(\omega_{\rm r},\omega_{\rm s},\omega_{\rm i})|^2 \end{aligned}$$

where $g(\omega_{\rm i}) = [\partial k/\partial\omega]_{\omega=\omega_{\rm i}}$ is a factor resulting from the change of variable from k to ω and R is the repetition rate of the pump. To further simplify the expression for R_3, we expand the phase mismatch Δk to second order in the signal detuning ν_m from the point of PPM $\omega_m^0 = \omega_p/3$, assuming that the pump frequency is fixed at the PPM point. The zeroth and first order terms in the expansion vanish, giving

$$\Delta k = k(\omega_{\rm s}) + k(\omega_{\rm r}) + k(\omega_{\rm i}) - k(\omega_{\rm p}) = \frac{D_{\rm s}}{2}[\nu_{\rm r}^2 + \nu_{\rm s}^2 + (\nu_{\rm s}+\nu_{\rm r})^2], \tag{6.29}$$

where we have eliminated one of the signal detunings (ν_i) from the integration using the energy conservation rule. $D_{\rm s} \equiv \partial^2 k/\partial\omega^2$ is the group velocity dispersion (GVD)

of the signal mode, which is the same for the all frequencies in mode-degenerate TOSPDC.

We note that for a Gaussian pump, the peak pump power P_0 is related to the average pump power P and to the repetition rate R by $P_0 = P\sigma/\sqrt{2\pi}R$ and that $\left|\int \mathrm{d}\omega_\mathrm{p}\beta(\omega_\mathrm{p})\right|^2 = \sqrt{2\pi}\sigma$. The dependence on the pump bandwidth σ disappears from the factor outside the integrals characterizing the rate R_3 in Eq. (6.28), so we can easily take the limit $\sigma \to 0$ corresponding to continuous wave (cw) pumping to obtain

$$R_3 = \frac{2^2\,3^2\,\hbar c^3 n_\mathrm{p}^3}{\pi^2(\omega_\mathrm{p}^0)^2}\gamma^2 L^2 p \left(\frac{\omega_0}{n_0^2(\omega)}g(\omega_0)\right)^3 \times e^{-(\alpha_\mathrm{p}+3\alpha_\mathrm{s})L/2} \iint_{-\infty}^{\infty} \mathrm{d}\nu_\mathrm{r}\mathrm{d}\nu_\mathrm{s}|\Phi(\nu_\mathrm{r},\nu_\mathrm{s})|^2\,. \tag{6.30}$$

In the integration we used the approximation $\ell(\omega_0+\nu_\mathrm{r}) = \ell(\omega_0+\nu_\mathrm{s}) = \ell(\omega_0-\nu_\mathrm{r}-\nu_\mathrm{s}) = \ell(\omega_0)$, with $\omega_0 = \omega_\mathrm{p}/3$. For notational convenience, we made the replacement

$$\frac{(2\pi\lambda L)^2 3^2}{\delta k^3} = \frac{3^2(2\pi)^2\epsilon_0^3 c^3 n_\mathrm{p}^3}{\hbar^2(\omega_\mathrm{p}^0)^2}\frac{2\gamma^2 L^2 P}{\left|\int \mathrm{d}\omega_\mathrm{p}\beta(\omega_\mathrm{p})\right|^2}\,, \tag{6.31}$$

where γ is the effective nonlinearity from Eq. (6.15).

In the main text, we also introduced Eq. (6) for estimating the triplet generation rate with losses, not taking into account mode dispersion. The expression can be derived as follows. The number of complete triplets that reach the end of the waveguide after being generated in the segment of the waveguide from z to $z+\Delta z$ can be estimated as

$$\begin{aligned}\mathrm{d}N_3(z) &= \tilde{\zeta}\, N_\mathrm{p}(z)\, e^{-3\alpha_\mathrm{s}(L-z)}\,\Delta z \\ &= \tilde{\zeta}\, N_\mathrm{p0}\, e^{-\alpha_\mathrm{p} z}\, e^{-3\alpha_\mathrm{s}(L-z)}\,\mathrm{d}z\,,\end{aligned} \tag{6.32}$$

where N_p0 is the number of pump photons at the input facet of the waveguide. $\tilde{\zeta}$ quantifies the conversion efficiency. Integrating the expression above from $z = 0$ to

$z = L$ gives the total number of generated triplets

$$N_3 \equiv \int_0^L \mathrm{d}z\, N_3(z) = \frac{\tilde{\zeta}\, N_{\mathrm{p0}}}{\alpha_{\mathrm{p}} - 3\alpha_{\mathrm{s}}} \left(e^{-3\alpha_{\mathrm{s}} L} - e^{-\alpha_{\mathrm{p}} L} \right). \tag{6.33}$$

Maximizing this expression with respect to L gives the optimal length L_{opt}.

Due to strong light confinement within integrated waveguides and the potential to use high pump powers with materials that have a high damage threshold, two-photon absorption must be considered even for continuous wave pump sources. Multi-photon absorption is described by the relationship

$$\frac{\mathrm{d}I(z)}{\mathrm{d}z} = -\alpha^{(1)} I(z) - \alpha^{(2)} [I(z)]^2 \tag{6.34}$$

Where $\alpha^{(1)}$ is single photon loss, $\alpha^{(2)}$ is the two-photon absorption coefficient, and $I(z)$ is the light intensity in the waveguide as a function of position. We can solve Eq. (6.34) to calculate light intensity as a function of z

$$I(z) = \frac{\alpha I_0 / (\alpha^{(1)} + \alpha^{(2)} I_0)}{e^{\alpha^{(1)} z} - \alpha^{(2)} I_0 / (\alpha^{(1)} + \alpha^{(2)} I_0)} \tag{6.35}$$

Where I_0 is the initial light intensity inside the waveguide. Intensity relates to the number of photons in a waveguide propagating mode by $N_0 = I_0 A_{\mathrm{mode}} / \hbar\omega_{\mathrm{p}}$ where A_{mode} is the cross-sectional area of the mode. We can rewrite Eq. (6.32) to include the effect of two-photon absorption

$$\mathrm{d}N_3(z) = \frac{\tilde{\zeta}\; A_{mode} I_{\mathrm{p0}}}{\hbar\omega_{\mathrm{p}}} \frac{\alpha_{\mathrm{p}}^{(1)} / (\alpha_{\mathrm{p}}^{(1)} + \alpha_{\mathrm{p}}^{(2)} I_{\mathrm{p0}})}{e^{\alpha_{\mathrm{p}}^{(1)} z} - \alpha_{\mathrm{p}}^{(2)} I_{\mathrm{p0}} / (\alpha_{\mathrm{p}}^{(1)} + \alpha_{\mathrm{p}}^{(2)} I_{\mathrm{p0}})} e^{-3\alpha_{\mathrm{s}}^{(1)} (L - z)} \mathrm{d}z. \tag{6.36}$$

We can use the ratio of Eq. (6.36) and (6.32) to gain insight under which conditions two-photon absorption has a significant impact on device performance. We define an arbitrary threshold

$$\frac{\alpha_{\mathrm{p}}^{(2)} I_{\mathrm{p0}}}{\alpha_{\mathrm{p}}^{(1)}} (1 - e^{-\alpha_{\mathrm{p}}^{(1)} L_{\mathrm{opt}}}) < 0.2 \tag{6.37}$$

below which the impact of two-photon absorption decreases the photon triplet generation rate by less than 10%. For our proposed TiO_2 devices, this corresponds to $\alpha_p^{(1)}$ >10 dB/cm, a maximum pump power of approximately 1 W, and $\alpha_p^{(2)}$ = 3 cm/GW (determined by band-gap scaling [12] of two-photon absorption measured in the wavelength range 780 – 1560 nm [60]).

6.10 Appendix 4 - Coincidence detection signals

The temporal coherence of a triplet source is characterized by the third-order intensity correlation function

$$G^{(3)}(x_1, x_2, x_3) = \langle \Psi_3 | E^{(-)}(x_1) E^{(-)}(x_2) E^{(-)}(x_3) E^{(+)}(x_3) E^{(+)}(x_2) E^{(+)}(x_1) | \Psi_3 \rangle. \tag{6.38}$$

where $|\Psi_3\rangle$ is the triplet state defined in Eq. (6.26). For waveguides much longer than a typical signal wavelength, we can replace the wave vector summations by frequency integrals. Energy conservation allows us to eliminate one of the signal variables from the integration. We can also absorb physical parameters like the cw pump amplitude, the effective waveguide area and the material nonlinear susceptibility into a normalization factor factor that depends on the waveguide length L. We assume a narrow cw pump at fixed frequency ω_p.The triplet state is completely characterized by the spectral amplitude $\Phi(\omega_r, \omega_s)$ in eq. (6.27). The loss mismatch parameter $\Delta\alpha \equiv (\alpha_p - 3\alpha_s)$ introduces a frequency-dependent imaginary part to the spectral amplitude, which broadens the triplet state in the frequency domain. The $G^{(3)}$ function in eq.

(6.38) can be written in simplified form as

$$G^{(3)}(x_1, x_2, x_3) = |\psi(x_1, x_2, x_3)|^2, \tag{6.39}$$

were $\psi(x_1, x_2, x_3) = \langle 0| E^{(+)}(x_3)E^{(+)}(x_2)E^{(+)}(x_1) |\Psi_3\rangle$ is the so-called triphoton state [100], which can be written as

$$\begin{aligned}\psi(x_1, x_2, x_3) \;=\; & \int d\omega_1 d\omega_2 d\omega_3 \int d\omega_\mathrm{r} d\omega_\mathrm{s}\, f_1(\omega_1) f_2(\omega_2) f_3(\omega_3) \mathrm{e}^{-i\omega_1 x_1 - i\omega_2 x_2 - i\omega_3 x_3} \\ & \times \Phi(\omega_\mathrm{r}, \omega_\mathrm{s})\, \langle 0| a(\omega_1)a(\omega_2)a(\omega_3)a^\dagger(\omega_\mathrm{r})a^\dagger(\omega_\mathrm{s})a^\dagger(\omega_p - \omega_\mathrm{r} - \omega_\mathrm{s})|0\rangle.\end{aligned} \tag{6.40}$$

We assume Gaussian detector filters $f_j(\omega) = f_0 \mathrm{exp}[-(\omega - \omega_j)^2/2\sigma_j^2]$, where f_0 is a normalization constant and ω_j is the center frequency of the j-th spectral filter. All filters are assumed to have the same bandwidth $\sigma_k = \sigma$. We ignore the frequency-independent normalization factor of the state.

The correlation function $\langle 0|a(\omega_1)a(\omega_2)a(\omega_3)a^\dagger(\omega_\mathrm{r})a^\dagger(\omega_\mathrm{s})a^\dagger(\omega_\mathrm{i})|0\rangle$ in eq. (6.40) contains six terms corresponding to permutations of the frequency variables. We can interpret each term by labelling a photon in the triplet source by its frequency. There are thus $3! = 6$ ways for these photons to reach three photodetectors. If the optical paths from the triplet source to each detector are indistinguishable, then all six frequency permutations give the same contribution to the field correlation function. It thus suffices to compute a single permutation to study the triple coincidence signal. We choose $\omega_1 = \omega_\mathrm{r}$, $\omega_2 = \omega_\mathrm{s}$, and $\omega_3 = \omega_p - \omega_\mathrm{r} - \omega_\mathrm{s}$ to obtain

$$\psi(x_1, x_2, x_3) = \mathrm{e}^{-i\omega_p x_3} \iint d\omega_\mathrm{r}\, d\omega_\mathrm{s} f(\omega_\mathrm{r}) f(\omega_\mathrm{s}) f(\omega_p - \omega_\mathrm{r} - \omega_\mathrm{s}) \Phi(\omega_\mathrm{r}, \omega_\mathrm{s}) \mathrm{e}^{-i\omega_\mathrm{r}(x_1 - x_3) - i\omega_\mathrm{s}(x_2 - x_3)}. \tag{6.41}$$

We expand the frequencies as $\omega_m = \Omega_m + \nu_m$, with $m = \{\mathrm{r}, \mathrm{s}, \mathrm{i}\}$, around central signal frequencies Ω_m that satisfy the energy conservation rule $\omega_p = \omega_\mathrm{r} + \omega_\mathrm{s} + \omega_\mathrm{i}$ at the

PPM point. In what follows we consider that the spectral filter $f(\omega_m)$ is centered at the frequency Ω_m. Expanding the wavenumbers to second order in the frequency detunings ν_m around the PPM point gives a phase mismatch Δk as in eq. (6.29). For mode-degenerate down-conversion the group velocities are equal for the three photons, making the linear term vanish by energy conservation for a cw pump. We can rewrite the integrals in terms in terms of frequency detunings to obtain

$$G^{(3)}(x_1,x_2,x_3) = \left| \int d\nu_{\rm r} d\nu_{\rm s} f_r(\nu_{\rm r}) f_s(\nu_{\rm s}) f_i(\nu_{\rm r}+\nu_{\rm s}) \Phi(\nu_{\rm r},\nu_{\rm s}) {\rm e}^{-i\nu_{\rm r}(x_1-x_3)-i\nu_{\rm s}(x_2-x_3)} \right|^2 . \tag{6.42}$$

The numerical evaluation of the integral is simplified by rescaling the detunings and delay times as ν_n/ν_0 and x_n/τ_0, where $\tau_0 = \sqrt{D_s\, L/2}$ and $\nu_0 = 1/\tau_0$ are the characteristic frequency and timescale associated with a waveguide of length L and group velocity dispersion D_s of the signal guiding mode.

The two-photon coincidence detection signal is proportional to the second-order correlation function

$$G^{(2)}(x_1,x_2) = \langle \hat{E}^{(-)}(x_1)\hat{E}^{(-)}(x_2)\hat{E}^{(+)}(x_2)\hat{E}^{(+)}(x_1)\rangle, \tag{6.43}$$

which can be written by inserting the resolution of the identity in the Fock basis as

$$G^{(2)}(x_1,x_2) \;=\; \int d\omega_3 |\, \langle 0|\, a(\omega_3) E^{(+)}(x_2) E^{(+)}(x_1)\, |\Psi_3\rangle\, |^2, \tag{6.44}$$

with a wavepacket amplitude given by

$$\begin{aligned} \langle 0|\, a(\omega_3) E^{(+)}(x_2) E^{(+)}(x_1)\, |\Psi_3\rangle \;=\; & \int d\omega_1 d\omega_2 \int d\omega_{\rm r} d\omega_{\rm s} \Phi(\omega_{\rm r},\omega_{\rm s}) f(\omega_1) f(\omega_2) {\rm e}^{-i\omega_1 x_1 - i\omega_2 x_2} \\ & \times \langle 0| a(\omega_3) a(\omega_1) a(\omega_2) a^\dagger(\omega_{\rm r}) a^\dagger(\omega_{\rm s}) a^\dagger(\omega_p-\omega_{\rm r}-\omega_{\rm s}) |0\rangle . \end{aligned}$$

The evaluation of the vacuum correlation function gives $2! = 4$ non-zero terms associated with the commutation of the operators $a(\omega_1)$ and $a(\omega_2)$ with $a(\omega_{\rm r})$ and $a(\omega_{\rm s})$.

These these four terms can be made equal to each other by exchanging integration variables appropriately when the optical paths to the detectors are equal. We thus evaluate a single representative term, corresponding to $\omega_1 = \omega_\mathrm{r}$ and $\omega_2 = \omega_\mathrm{s}$ to obtain

$$G^{(2)}(x_1, x_2) = \int d\nu_3 \left| \int d\nu_\mathrm{r} G(\nu_\mathrm{r}, \nu_\mathrm{r} + \nu_3) f_1(\nu_\mathrm{r}) f_2(\nu_\mathrm{r} + \nu_3) e^{-i\nu_\mathrm{r}(x_1 - x_2)} \right|^2 . \tag{6.45}$$

Chapter 7

Experimental work toward realization of a TOSPDC source

7.1 Introduction

In 6 we laid the groundwork for designing efficient photon triplet sources using integrated waveguides. In the following section we will discuss our progress towards experimental demonstrations as well as several of the remaining challenges.

Theoretical designs of TOSPDC experiments have been conducted for a number of different device designs, including silica fibers [104], bulk crystals [121], and our own work in polycrystalline anatase TiO_2 nanoscale integrated waveguides (Chapter 6). It is helpful to draw a comparison between these theoretical works and the best experimental demonstrations to-date using cascaded SPDC [97,98]. Silica fibers have predicted generation efficiencies comparable to current experimental demonstrations, on the order of 10^{-2} triplets/s/mW of pump power, with the caveat that losses

in the fiber are not taken into account [104]. Theoretical predictions of TOSPDC in bulk crystals are at least three orders of magnitude lower [121]. Our work on polycrystalline anatase TiO_2 waveguides, on the other hand, predicts efficiencies one order of magnitude higher than silica fibers or cascaded SPDC, approximately 0.1 triplets/s/mW of pump power. As we discussed in Chapter 6, this efficiency can be greatly improved with optimization of fabrication and material deposition to reduce losses and increase nonlinearities in the material. This makes integrated waveguides the best avenue to achieve experimental demonstrations of directly generated photon triplets via TOSPDC.

Despite relatively high predicted device efficiencies, experimental demonstrations are non-trivial. Many challenges are still present, many of which we have made progress in addressing.

We will begin by describing our integrated chip coupling and measurement setup, as well as our device characterization and preparation methods. This requires measurement of losses in the visible and infrared, polishing of the chip to achieve the optimal device length and produce clean facets for improved coupling, and characterization of the phase-matched pump wavelength. These steps are designed to ensure only waveguides with the correct parameters and low losses are used for TOSPDC experiments due to the long measurement times required to attain statistically significant results.

We will then cover the three most important experimental challenges to consider: fabrication variations, management of infrared photons in the pump source, and management of the device damage threshold and infrared signal generated by

fluorescence and competing nonlinear processes in the device. Fabrication variations can be mitigated by device design and proper characterization of the fabricated devices. Infrared photons in the pump source can be a significant problem especially for tunable sources which rely on nonlinear optical interactions to function. This presents trade-offs between using diodes which have a very small tuning range versus pulsed or truly tunable laser sources. Fluorescence in the device and the damage threshold at the pump wavelength define the maximum pump power that can be used in experimental demonstrations. Several methods can be implemented during measurements to mitigate the impacts of fluorescence.

We provide a description of experimental progress to-date on detecting photon triplets generated via TOSPDC in polycrystalline anatase TiO_2 nanoscale waveguides, including our progress characterizing fluorescence in our devices. We conclude the chapter with an overview of immediate experimental goals toward enabling experimental demonstrations of TOSPDC in nanoscale waveguides.

7.2 Device characterization and preparation

Limited single photon counter efficiencies can lead to verified photon triplet detection rates over an order of magnitude lower than the photon triplet generation rate. Additional losses inherent in coupling light out of integrated devices and in the beam path between the entangled photon source and the detectors will further reduce the detection rate. For these reasons, gathering statistically significant data to verify the conversion efficiency of an entangled photon source or to characterize the entangled state requires long integration times, on the order of 10s of hours or longer.

We also discussed in Chapter 6 that fabrication variations can lead to variations in the phase-matched wavelength and that pumping a TOSPDC source off the perfectly phase-matched (PPM) wavelength can greatly complicate measurements or reduce the conversion efficiency. Consequently, an efficient characterization scheme for integrated photon triplet sources is necessary in order to quickly assess the quality of the device and determine the required pump wavelength. We use a combination of linear loss measurements and nonlinear characterization with third-harmonic generation (THG) on our fabricated devices to experimentally determine the ideal device length and PPM wavelengths of each waveguide.

We begin with linear loss measurements to determine the ideal device length. We provide a schematic of our coupling setup in Figure 7.1. We couple light in and out of our devices using end-fire coupling with a pair of 0.85 NA objectives on a pair of 3-axis stages. The device is mounted on a 2-axis stage between the two objectives. Photodiode detectors are used to measure the input laser power before the input coupling objective and the transmitted power after the output objective. Continuous wave (CW) infrared lasers (IR) at 1310 and 1550 nm are used to measure the total transmission loss across the device at the signal wavelength. We can account for the coupling losses in our devices (3–6 dB/facet [62]) based on previous measurements. We estimate the propagation loss based on the measured total transmission loss and expected coupling loss, with expected values between 4–10 dB/cm in the infrared [**?**,62]. Top-view imaging techniques can also be used to provide a direct estimate of propagation losses [**?**]. We include a half wave plate and polarizer for the infrared in the input beam path in order to characterize the transmission losses for both

TE and TM polarizations at the IR signal wavelength. We complete these same measurements in the visible. Because losses in the visible are high (15–30 dB/cm), relatively high input powers (>100 mW) must be used to accurately measure an output power. These measurements allow us to estimate the ideal device length and determine which waveguides have the lowest losses and are thus most suited for TOSPDC measurements.

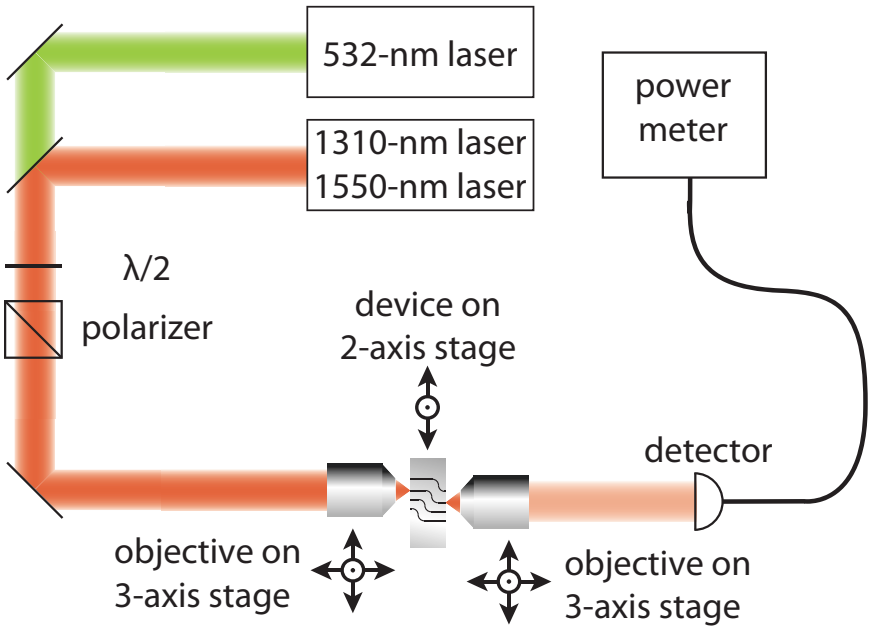

Figure 7.1: Schematic of the coupling setup used to measure linear transmission losses in TiO_2 nano-scale waveguides. The chip is imaged from above using a stereo microscope to aid in alignment of the input and output objectives. Both the input and output laser powers are measured using a power meter. Coupling through the waveguides is optimized by maximizing the power measured at the output power meter.

We conclude device characterization with THG. We modify the original coupling setup in Figure 7.1 to launch infrared pulses into the waveguides (Figure 7.2). We use a pulsed fiber laser with 80-MHz repetition, <100-fs pulse duration, maximum

output power of approximately 350 mW, and a spectrum covering 1510–1600 nm. The maximum average power we can couple into our waveguides from this pulsed source without causing damage is approximately 100 mW. Optical damage manifests itself as an increase in the total waveguide transmission loss. We note that the effective bandwidth of the laser is increased in the waveguide due to spectral broadening [60], allowing us to identify PPM points by measuring THG between 500–535 nm. Visible light generated via THG is measured by bringing a bare fiber connected to a visible spectrometer close to the waveguide to collect scattered signal. The fiber is mounted on a 3-axis translation stage to enable measuring THG along the length of the waveguide. Fabrication variations along the length of the waveguide can shift the phase-matching point. These measurements determine the PPM point(s) for each waveguide and thus the ideal pump wavelength to use in a TOSPDC measurement.

Additional information about the quality of the waveguide can be extracted from the measured THG spectrum. We note that based on the interaction length between the pulsed IR pump and visible THG signal, we can estimate the expected bandwidth of the THG signal. Changes in waveguide width and height shift the phase-matched wavelength and thus the wavelength of visible photons generated via THG. We can use the measured THG spectrum to estimate the uniformity of the waveguides fabricated by using simulations of waveguides with slightly different width and thickness to determine the rate at which phase-matched wavelengths shift as a function of varying waveguide dimensions. Choosing uniform waveguides for TOSPDC measurements will lead to a narrower IR signal bandwidth, which will improve the coupling efficiency and simplify measurements due to reduced impact from chromatic dispersion effects.

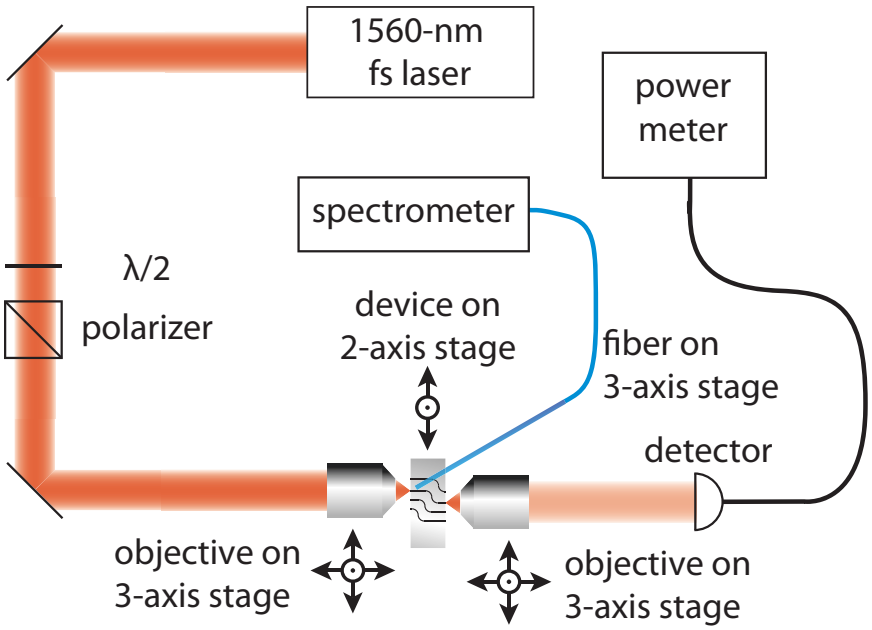

Figure 7.2: Modified coupling setup used to measure THG signal from devices designed for TOSPDC. A fiber is aligned with a waveguide using a 3-axis translation stage while the waveguide is pumped with femtosecond pulses in the IR. Light collected in the fiber is used to measure the visible spectrum generated via THG.

We polish waveguide to reduce coupling losses at the input and output facets and to reduce the waveguide length to the ideal device length. Finite element simulations give a maximum power overlap of over 60% between the fundamental guided modes in waveguides suitable for TOSPDC and a focused Gaussian beam spot from a 0.85 NA objective at 1550 nm. Consequently, Fresnel reflections only account for approximately 2 dB/facet of the coupling loss. The remaining 1–4 dB/facet arises from scattering off imperfections created during facet cleaving. This additional scattering loss can be greatly reduced or almost entirely removed by polishing the end facets of devices. The polishing process provides the opportunity to also carefully control the length of waveguides on the chip by polishing the device to a specific width.

Linear loss and THG measurements are a quick and reliable method for characterizing devices and provide a final opportunity to optimize devices before attempting TOSPDC measurements. Measuring photon triplet generation requires multiple hours of measurement for a single waveguide. In contrast, linear loss and THG measurements can be completed for several waveguides within an hour. Especially if the available visible pump wavelengths are limited by equipment, selection of specific waveguides with the correct PPM wavelength is critical. Finally, reduction of losses with polishing and adjusting the waveguide length to the optimal length maximizes the potential number of triplet photons that can be generated and measured from a device.

7.3 Fabrication difficulties

As we described above, THG results can reveal the presence of fabrication variations and these variations can lead to reduced conversion efficiency and a broadened signal in TOSPDC. These include variations along the length of a single waveguide, such as waveguide sidewall and surface roughness and fabrication defects. Deviations of the fabricated waveguide width and thickness relative to the designed parameters are also common due to variations in the processing conditions from one fabrication run to the next. Fabrication variations along the length of a single waveguide lead to changes in the phase-matching conditions and broadening of THG and TOSPDC signal. Deviations from the designed width and thickness lead to a shift in the phase-matching condition of the entire waveguide, leading to a phase-matched wavelength that is shifted from the expected value. In this section we discuss sources of fabrica-

tion variations and several methods of mitigating their effects on experiments.

7.3.1 Variations in dimensions along a single waveguide

Variations in dimensions along the length of individual waveguides are significantly impacted by the properties of materials used in the device and can be introduced by several steps in the fabrication process. The morphology of the thin films we pattern to form the waveguide core impacts the fabricated structures. Our devices are fabricated from thin films of polycrystalline anatase TiO_2. Surface roughness of the film, introduced primarily by grain boundaries (Figure 7.3a), determines the roughness of the top surface of fabricated waveguides. Using AFM, we have measured a minimum root mean squared roughness of 3–6 nm in our deposited films with grain sizes of approximately 20–50 nm in the plane of the film. Cleaving the device reveals that the crystal grains are columnar spanning the thickness of the film in the vertical direction (Figure 7.3b). This grain structure contributes to the roughness on waveguide sidewalls (Figure 7.3c and d). These characteristics of the TiO_2 films introduces unavoidable variations in waveguide width and thickness.

Waveguide dimension variations along the length of individual waveguides can also be introduced by steps in the fabrication process. Slight variations of the resist thickness across the device and variations in the exposure of resist during electron beam lithography lead to changes in the waveguide width. The morphology of the mask used during the etch step of waveguide fabrication can also introduce sidewall roughness. We use a chromium mask deposited via electron beam evaporation. The mask consists of chromium grains of finite size. Smaller grain sizes lead to a smoother

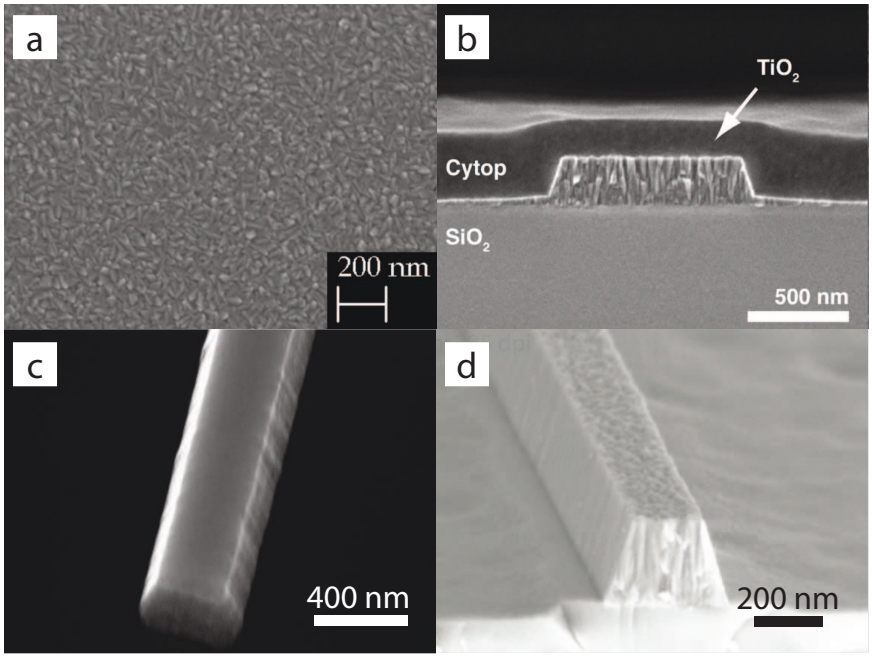

Figure 7.3: (a) SEM of the top surface of a polycrystalline anatase TiO_2 film deposited by sputtering. Grains on the order of 20–50 nm in size are visible. (b) SEM of the cleaved facet of an anatase TiO_2 waveguide. The columnar grains spanning the thickness of the waveguide are visible in the waveguide core. (c) Top view of a waveguide showing variations in waveguide width along the length on the order of 10–20 nm. (d) Angled view of a cleaved waveguide end facet showing the roughness on the waveguide sidewalls resulting from a combination of etching and the columnar grains in the polycrystalline anatase TiO_2 films.

mask because any roughness along the edge of the mask is transferred to the TiO_2 when unmasked material is etched away to define the waveguides. We have measured sidewall roughness on the order of 10–20 nm in TiO_2 waveguides using SEM imaging (Figure 7.3c and d).

7.3.2 Deviations from design dimensions

Deviations of fabricated device dimensions from the designed specifications pose a significant problem because the tolerance tends to be very tight for waveguides designed for TOSPDC. The first source of deviations is in deposition of the nonlinear optical material used to fabricate the waveguides. Deposition rates and optical properties of deposited films vary from one deposition run to another when using thin film deposition techniques, particularly when the equipment is used for many different deposition processes. This leads to deposition of films that are not the correct thickness for the designed waveguide and exhibit slightly different dispersion properties from previous films. We have observed film thickness deviations of approximately $\pm 20\%$ from the designed parameters and index variations of approximately $\pm$ 0.1 for TiO_2 films, measured using spectroscopic ellipsometry. Secondly, variations during fabrication can lead to deviations of waveguide width from the designed parameters. The thickness of the electron beam lithography resist, deviations from the intended dose during electron beam lithography, and variations in temperature and time during electron beam mask developing lead to changes in the overall width of waveguides fabricated. Fabricating waveguides and features close together also leads to a proximity effect – writing a second structure nearby exposes the existing structure further, leading to increased dimensions. We have observed deviations in the fabricated waveguide width of $\pm$ 40 nm from the designed width in TiO_2 waveguides.

7.3.3 Improvements to fabrication

We have explored and considered numerous methods to mitigate the impact of fabrication variations – including roughness and variations along the length of individual waveguides, as well as deviations from the design parameters.

Film deposition and fabrication techniques can be adjusted to reduce roughness and variations along the length of waveguides. Film deposition can be optimized in two different ways. Choosing film deposition parameters that minimize the grain size could reduce the impact of grain boundaries on the sidewall of waveguides. Additionally, grain boundaries will contribute less severely to waveguide loss if the grain size is deeper sub-wavelength. The other option is to epitaxially grow films in order to eliminate the presence of grain boundaries. Epitaxial growth requires changing the substrate to a lattice-matched crystal, such as sapphire, which may have other impacts on device design and fabrication. Theoretically, epitaxial, single-crystal films will have no losses as a result of grain boundaries. Primary loss mechanisms would arise from defects and contaminants in the film.

Several methods can be used to improve device quality using fabrication optimization. Resist reflow techniques have been used to successfully lower the scattering losses in devices by reducing roughness at the edges of features [122,123]. The impact of this technique may be limited in devices fabricated from polycrystalline materials due to the impact of grain boundaries on roughness. Using multiple electron beam exposures during lithography to deliver the desired dose can reduce random variations in dose across the device and lead to more consistent device dimensions. Additionally, etch optimization has been used in other material systems to reduce waveguide side-

wall roughness and losses by as much as an order of magnitude [77]. Finally, atomic layer deposition (ALD) on top of fabricated waveguides has been used to reduce the roughness and losses in TiO_2 waveguides and provides a post-fabrication method of improving devices [124].

Because a significant percentage of our device losses and measured waveguide roughness in nanoscale TiO_2 waveguides is due to grain boundaries and surface roughness in our films, as evidenced by losses measured using prism coupling (3 dB/cm in the IR and 15 dB/cm in the visible), film deposition optimization must be used in conjunction with the other proposed improvements.

We can address deviations from designed dimensions with the addition of several steps in the fabrication process and careful planning in the device design process. Achieving the correct film thickness is the first priority. One option is to deposit a film that is thicker than necessary and use an etching process to reduce the thickness to the value dictated by the device design before completing fabrication of the waveguides. The second option is to use a thinner film and either increase the thickness before fabrication using ALD or use ALD after device fabrication to fine tune both the waveguide width and thickness. Because the waveguide width can vary by as much as $\pm$ 40 nm relative to the designed width due to the fabrication process, this variation must be taken into account in device design. We design our TiO_2 devices with several sets of waveguides with designed widths ranging from $W_{design} - 40$ nm to $W_{design} + 40$ nm in 5–10-nm increments. Using device characterization via THG allows us to identify which of these waveguides falls closest to the desired design specifications.

7.4 Selection of pump sources

The pump source can have a significant impact on the experimental setup for TOSPDC and the output signal. The presence of infrared photons in some visible lasers is an issue that must be addressed due to the low conversion efficiencies, on the order of 10^{-15}, in even the most efficient photon triplet sources. Very low emission rates of IR photons, on the order of 10^{-12} per visible photon, can cause serious problems because this introduces noise over the generated signal photons. This level of selectivity is significantly higher than what is required for most laser applications. Pump bandwidth impacts the minimum signal bandwidth of the device due to the rapid expansion of the signal spectrum as the pump photon wavelength is detuned from the PPM point. Additionally, given the fabrication difficulties discussed above, a tunable pump source would allow compensating for deviations in the fabricated waveguide from the device design, simplifying device fabrication by tuning the pump source to the PPM wavelength identified by THG. The ideal pump source for TOSPDC would provide high power (several 100 mW) with narrow line width, tunability over at least 10 nm around 440 or 520 nm, and produce no IR photons. This set of characteristics is generally unrealistic, especially in the case of visible laser sources – diode laser sources often lack tunability and many tunable laser sources rely on nonlinear interactions which introduce IR photons into the output. This leads to a trade-off between choosing a source with low IR output but low tunability, which exacerbates challenges caused by fabrication variations, and choosing a source with high wavelength tunability but IR noise in the pump beam.

Visible diode lasers tend to avoid issues of IR photons in the beam path. Some

tunability can be achieved, typically on the order of ± 1–2 nm, through temperature control of the laser diode. Though many laser diodes have line widths of 1–2 nm, placing the diode in a cavity can provide a narrow line width.

Tunability over a large wavelength range in the visible often requires making use of nonlinear optical processes, such as spectral broadening of a pulsed near infrared source. These types of sources can produce output across the visible spectrum. Because the output from spectral broadening is broadband, the power per unit bandwidth can be severely limited to several mW/nm. The line width is defined by the filter used in the output beam path and is often in the range of 0.5–1 nm.

Many laser sources, particularly those relying on frequency conversion to produce the output wavelength, utilize band pass filters to remove unwanted wavelengths from the output. As one example, many lasers at 532 nm are doubled Nd:YAG lasers, where the remaining light at 1064 nm is filtered from the output. We have found during experiments with tunable pulsed lasers that the stop band of dielectric filters tends not to be wide enough to fully remove IR signal from the pump beam path or the optical density of the stop band is not high enough. This is to be expected because designing a dielectric stack with a stop band spanning at least two octaves from the visible around 600 nm to 2 μm is non-trivial and most applications do not require such a large wavelength range to be clear of noise. We have used a prism-based wavelength filter for the visible pump beam path (Figure 7.4) to solve this limitation.

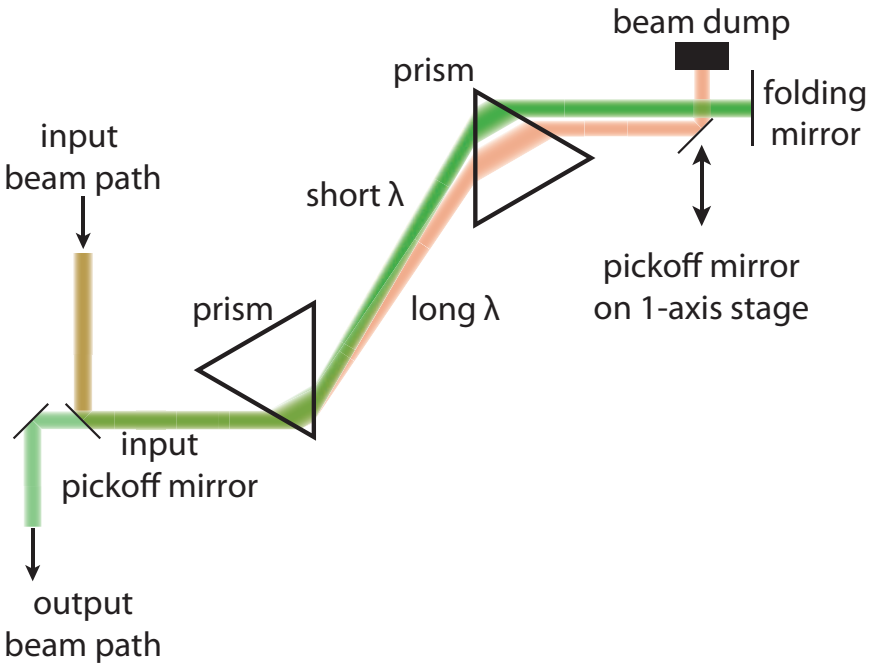

Figure 7.4: Spatial filtering provides a reliable method to remove broadband IR noise from the pump beam path. A pickoff mirror after the second prism sends long wavelengths into a beam dump. The pickoff mirror is placed on a translation stage to adjust the wavelengths that are allowed to pass. The folding mirror angles the output beam up to bypass the input pickoff mirror.

7.5 Defining maximum pump power

Two factors related to the TOSPDC source put a limit on the maximum pump power – the damage threshold of the device facet at the pump wavelength and ratio between the photon triplet generation efficiency and IR fluorescence photon generation rate in the device. The effect of exceeding the damage threshold is relatively straight-forward. As the damage threshold is exceeded, damage at the input facet reduces the efficiency of coupling light into the waveguide. This is measured as an increase in the total transmission loss across the device. The damage threshold is thus a hard upper limit on the pump power than can be used with a device. Fluo-

rescence generated by the waveguide core and cladding materials sets a cap on the pump power used based on the acceptable signal-to-noise ratio when operating the TOSPDC photon triplet source. Aside from generating noise in the detectors in the form of extra counts, fluorescence can also produce accidental photon triplet coincidences if three or more fluorescence photons arrive at the detectors simultaneously. In this section we derive a formula which defines the maximum pump power based on the acceptable ratio of real photon triplet generation to triplet coincidences produced by fluorescence noise.

Fluorescence is most-prevalent in materials with a direct bandgap, but can also arise from impurities and defects. TiO_2 (indirect bandgap) has low fluorescence compared to many other materials with sufficient transparency, high linear index, and high nonlinear index for efficient TOSPDC. However, due to the expected low efficiency of TOSPDC (on the order of 10^{-15}), even in comparatively efficient devices, fluorescence cannot be discounted. Fluorescence will produce photons at random times within the material. Based on the generation rate, the probability of detecting an accidental triplet coincidence due to three fluorescence photons arriving within a small time interval can be calculated.

Photon triplets are identified when three photons are detected within a given correlation time, $\tau_{correlation}$. The expected correlation time is determined by the timing jitter of the single photon counters used for the measurement, bandwidth of the photon triplets, dispersion within the waveguide, and dispersion in the optical fibers or beam path leading from the photon triplet source to the detectors. Typical timing jitter for state-of-the-art detectors is < 90 ps. The spread of photons in time due to

dispersion is given by:

$$\Delta\tau = GVD \times L \times \Delta\lambda_{\mathrm{S}} \tag{7.1}$$

where GVD is the group velocity dispersion of the medium through which the photon triplets propagate in units of ps/nm/km, L is the propagation distance within the medium, and $\Delta\lambda_{\mathrm{S}}$ is the bandwidth of the signal. For example, if a photon triplet signal with 100-nm bandwidth propagates through 10 m of fiber optic cable to the detectors, dispersion will add approximately 20 ps to the correlation time. Depending on the bandwidth of the signal photons and the experimental setup, we expect correlation times in experiments to range from approximately 100–1000 ps, with a theoretical minimum correlation time determined by the timing jitter of the detectors used in the experiment.

The fluorescence count rate increases linearly with increasing pump power; however, the rate of spurious photon triplet detections rises nonlinearly. At the same time, the rate of actual photon triplet generation rises linearly with pump power. Therefore, lower pump powers give better signal to noise. The rate at which photons generated via fluorescence reach the end of the waveguide, assuming the rate at which fluorescence photons are generated is linearly dependent on the number of pump photons in the waveguide, is given by:

$$R_{\mathrm{fl}} = \rho_{\mathrm{fl}} N_{\mathrm{P0}} = \frac{\zeta_{\mathrm{fl}}}{\alpha_{\mathrm{P}} - \alpha_{\mathrm{S}}} \left(e^{-\alpha_{\mathrm{S}} L} - e^{-\alpha_{\mathrm{P}} L} \right) N_{\mathrm{P0}} \tag{7.2}$$

Where ζ_{fl} is the efficiency with which pump photons generate fluorescence photons per unit length in the waveguide. The rate of spurious photon triplet coincidences at the waveguide end facet due to fluorescence is given by:

$$R_{\mathrm{falseT}} = R_{\mathrm{fl}}^3 \tau_{\mathrm{cor}}^2 \tag{7.3}$$

assuming that fluorescence photons are generated and arrive at the detectors randomly and are not inherently bunched.

We want to maintain a condition where $R_{\mathrm{T}} > R_{\mathrm{falseT}}$. We can write a simplified equation for the generation rate of "true" and "false" triplets:

$$R_{\mathrm{T}} = \rho_{\mathrm{T}} N_{\mathrm{P0}} = \frac{\zeta_{\mathrm{T}}}{\alpha_{\mathrm{P}} - 3\alpha_{\mathrm{S}}} \left(e^{-3\alpha_{\mathrm{S}} L} - e^{-\alpha_{\mathrm{P}} L} \right) N_{\mathrm{P0}} \tag{7.4}$$

$$R_{\mathrm{flT}} = \rho_{\mathrm{fl}}^3 N_{\mathrm{P0}}^3 \tau_{\mathrm{cor}}^2 = \left(\frac{\zeta_{\mathrm{fl}}}{\alpha_{\mathrm{P}} - \alpha_{\mathrm{S}}} \right)^3 \left(e^{-\alpha_{\mathrm{S}} L} - e^{-\alpha_{\mathrm{P}} L} \right)^3 N_{\mathrm{P0}}^3 \tau_{\mathrm{cor}}^2 \tag{7.5}$$

The efficiency with which pump photons are converted to photon triplets and fluorescence photons, respectively, is given by ρ_{T} and ρ_{fl}. The conversion efficiencies (ρ_{T} and ρ_{fl}) in Equations 7.4 and 7.5 above include the effects of photon loss. N_{P0} represents the rate at which pump photons are introduced at the start of the waveguide and is related to the pump power P_{P0} by the relationship $P_{\mathrm{P0}} = N_{\mathrm{P0}} \omega_{\mathrm{P}} \hbar$. Therefore, the pump power used in experiments must be below:

$$N_{\mathrm{P}} < \sqrt{\frac{\rho_{\mathrm{T}}}{\rho_{\mathrm{fl}}^3 \tau_{\mathrm{cor}}^2}} \tag{7.6}$$

We note that when we compare Equations 7.4 and 7.5, the rate at which true photon triplets reach the end of the waveguide and the rate at which false triplet coincidences reach the end of the waveguide scale differently with device length. This is the result of requiring that all 3 photons in a triplet must exit the device. However, fluorescence photons are generated randomly and the detection of false three photon correlations depends only on the total rate at which fluorescence photons exit the device. We can gain insight into the impact of this difference in scaling by comparing the optimal device length, $\mathrm{L_{opt}}$, at which the maximum number of photon triplets reaches the end

of a device and L_{flmax}, the device length at which the maximum number of fluorescence photons reaches the end of a device:

$$L_{opt} = \frac{1}{\alpha_P - 3\alpha_S} \ln\left(\frac{\alpha_P}{3\alpha_S}\right) \tag{7.7}$$

$$L_{flmax} = \frac{1}{\alpha_P - \alpha_S} \ln\left(\frac{\alpha_P}{3\alpha_S}\right) \tag{7.8}$$

$$\frac{L_{opt}}{L_{flmax}} = \frac{\alpha_P - \alpha_S}{\alpha_P - 3\alpha_S} \frac{\ln(\alpha_P/3\alpha_S)}{\ln(\alpha_P/\alpha_S)} = \frac{\alpha_P - \alpha_S}{\alpha_P - 3\alpha_S}\left(1 - \frac{\ln(3)}{\ln(\alpha_P/\alpha_S)}\right) \tag{7.9}$$

Equation 7.9 is < 1 for all combinations of pump and signal loss ($\alpha_P \neq \alpha_S$ and

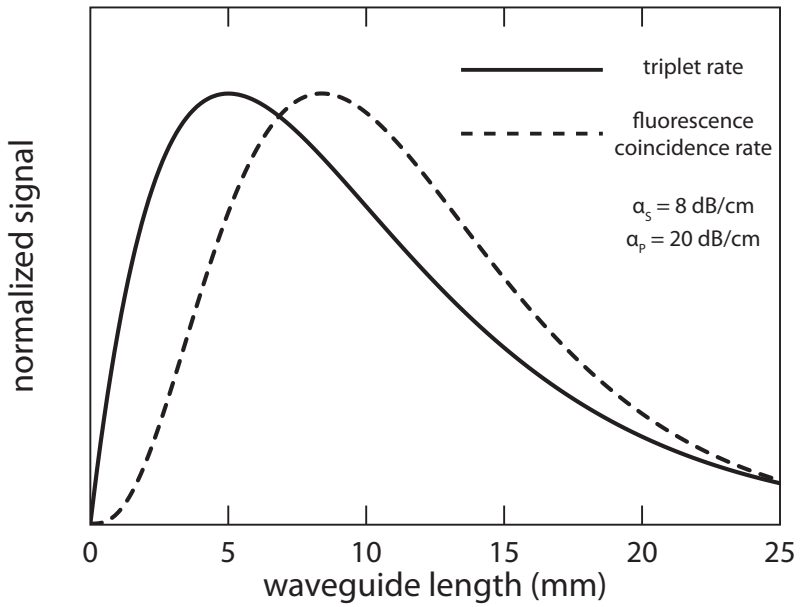

Figure 7.5: Plots of normalized photon triplet generation rate and fluorescence triplet coincidence rates as a function of device length. Notice that the true triplet generation rate rises and peaks before the fluorescence triplet coincidence rate does. The triplet and fluorescence coincidence rates are NOT normalized by the same value. Their relative magnitudes depend on the effective nonlinearity, fluorescence generation efficiency, and pump power used.

$\alpha_P \neq 3\alpha_S$). The rate at which true photon triplets are generated in a device rises

and peaks more quickly than the spurious photon triplet coincidence rate due to fluorescence (Figure 7.5). As the device length is increased, the signal-to-noise ratio, $R_{\mathrm{T}}/R_{\mathrm{flT}}$, decreases. This presents a trade-off between achieving high signal-to-noise by keeping the device short and achieving the maximum triplet generation rate by fabricating a device of length L_{opt} as defined by Equation 7.7. Furthermore, we can describe L_{opt} as the maximum desirable device length because a longer device length would reduce both the photon triplet generation rate and signal to noise ratio.

7.6 TOSPDC device measurement setup

In the following we will describe the setup used for TOSPDC measurements and discuss factors related to doing coincidence measurements of larger entangled states using single photon counters.

The setup used for TOSPDC measurements (Figure 7.6) closely resembles the device characterization setup, with several key changes. Light is launched into the input facet of the device using a 0.85 NA objective because both visible and infrared wavelengths need to be coupled in efficiently for initial device alignment purposes. A tapered-lens fiber is used to couple light out of the output facet because the goal is to efficiently couple out only the IR signal photons. We include the spatial filter described in Section 7.4 at the input to remove accidental IR signal present in the visible pump source. Additionally, we include a half wave plate and polarizer for the visible wavelengths in order to adjust the polarization of the input pump beam to achieve the optimal end-fire coupling efficiency for the desired higher order pump mode. The tapered-lens fiber at the output is connected to a fiber port collima-

tor to provide a short free-space beam path while introducing minimal losses. This free-space beam path allows us to introduce filters with a stop band in the visible to remove residual pump light from the output beam path, which could otherwise produce unwanted fluorescence signal through interactions with the fiber between the source and detector and within the detector itself. Additionally, band-pass filters may be used to allow only a narrow bandwidth about the center of the signal to pass to the detectors, enabling reduction of noise due to fluorescence photons generated in the device. Single photon counters used to measure the IR output from the device are directly connected using fibers.

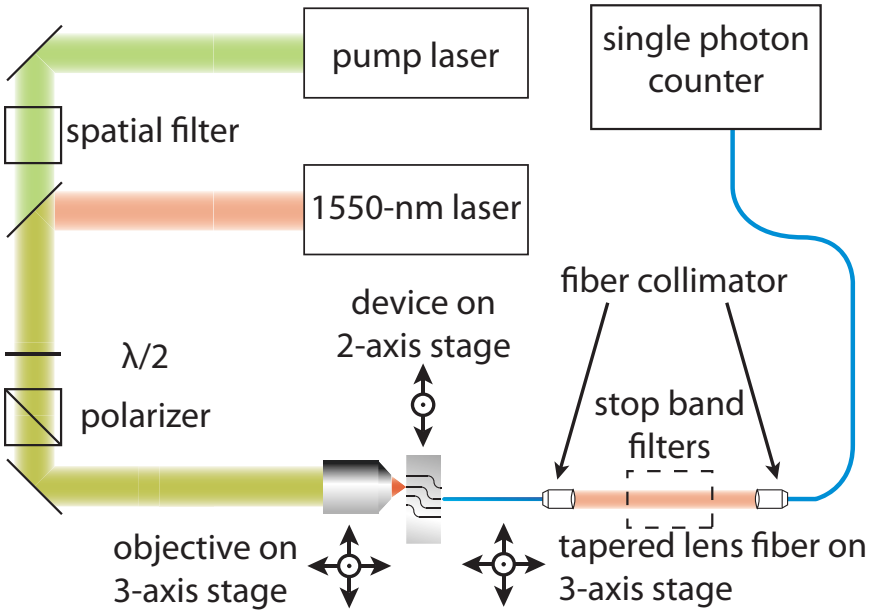

Figure 7.6: Schematic of the TOSPDC measurement setup. The spatial filter is added on the visible pump input beam path. Output coupling is achieved using a tapered lens fiber to avoid further losses which would be incurred by coupling into a fiber in a separate step. A pair of aligned fiber collimators provides a free space path for band pass filters to remove residual visible pump photons.

Successful detection of a photon triplet requires all three photons to reach the

detectors. As a result, losses in the output beam path must all be raised to the third power such that the probability of the complete triplet reaching the detectors is represented by $P_{\mathrm{T}} = e^{-3\alpha_{\mathrm{output}}}$ (shown schematically in Figure 7.7). Therefore, reducing losses at the output by optimizing output coupling, optimizing coupling in the fiber port collimator, choosing band pass filters with minimal loss in the IR, and minimizing losses in fiber-to-fiber connections between the source and detectors is critical.

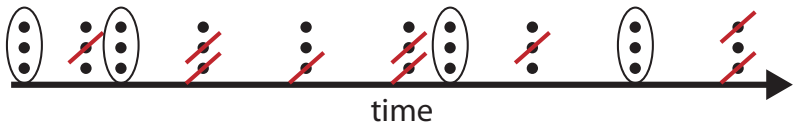

Figure 7.7: Schematic illustrating the impact of losses on successful detection of photon triplets. Losing approximately 30% of all signal photons leads to a loss of approximately 60% of complete photon triplets. Complete photon triplets are circled.

The field of single-photon detection in the infrared has advanced significantly. Superconducting nanowire single photon detectors (SNSPDs) [125, 126] provide high single photon detection efficiencies, >70% at telecommunications wavelengths. This is significantly higher than InGaAs single-photon avalanche diodes (SPADs), which achieve 5–30% efficiency. Though transition edge detectors can provide higher detection efficiencies, slow response times and low maximum count rates (on the order of 100 kHz [103]) make them a poor choice. As discussed above, fluorescence generated by materials in the device can be significant compared to the photon triplet generation rate. As a result, using detectors with a low maximum count rate would introduce an additional constraint on the pump power used and maximum achievable photon

triplet generation rate. Approaching the maximum detector count rate will lead to reduced detection efficiency because the detector will be operating with significant dead time.

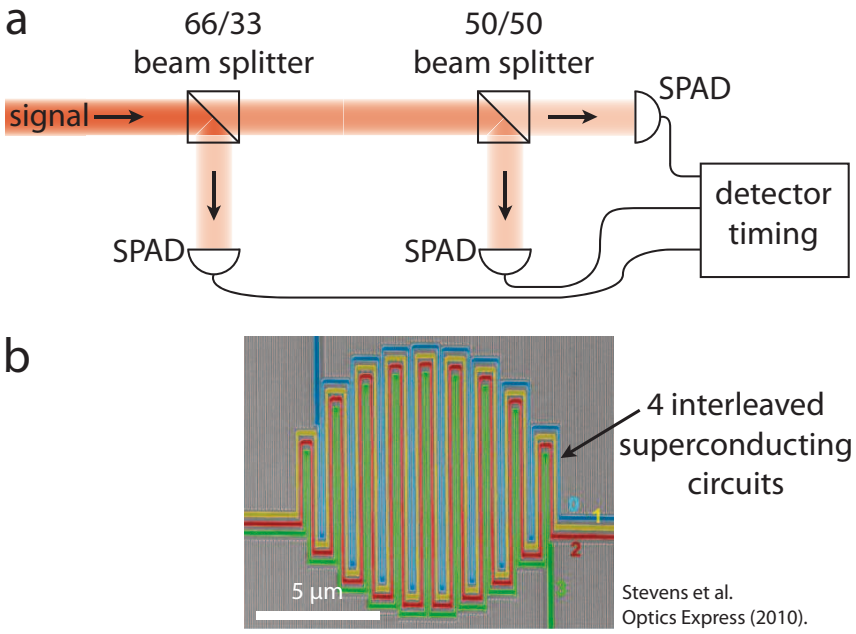

Figure 7.8: (a) Schematic of the detection scheme used when measuring coincidences of photon triplets using individual SPADs. Two beam splitters are used to route each photon in the triplet to a different SPAD. A timing card is used to precisely measure the time at which each SPAD detects photons. Corrections must be made to account for differences in path length that the photons take to each detector. (b) Image of an SNSPD array consisting of four interleaved detectors (color-coded) [125]. Signal photons are routed into the detector using a single-mode fiber and are incident on the detector from above. Each circuit covers roughly 25% of the detector area and can be read off independently, allowing coincidence detection of up to four photons with a single array. Assuming a total detection efficiency of 70% gives a detection efficiency of approximately 17.5% per individual superconducting circuit. These four circuits are also connected to a timing card, which enables calculation of correlation times for photon detections in all four superconducting circuits.

Detection efficiency is particularly important because all three photons in a

given triplet must be successfully detected in order to measure coincidences. However, coincidence measurements are further complicated when all three photons propagate in the same direction and are degenerate in frequency. Each of the photons in a triplet must be routed to a separate detector. This is most commonly done with a pair of beam splitters placed at the device output (Figure 7.8a). Assuming highly efficient SPADs (30% detection efficiency), the probability of detecting all three photons in a triplet is lower than 1% because the probability of each photon being directed to a different detector and each detector subsequently successfully picking up the photon must be taken into account. At the first beam splitter there is a 44% chance that one photon is directed to the first SPAD and two are directed toward the second beam splitter. There is a 50% chance that when two photons reach the second beam splitter, they are routed to separate SPADs. These probabilities must all be multiplied by one another:

$$P_{Tdetection} = P_{66/33\text{BS}} \times P_{50/50\text{BS}} \times P^3_{\text{SPADdetection}} = 0.44 \times 0.5 \times 0.3^3 = 0.006 \quad (7.10)$$

The combination of low detection efficiency of individual detectors and low probability of successfully routing individual photons in the triplet to different SPADs leads to vanishing probability of detecting a three-photon coincidence.

Many SNSPDs, on the other hand, are designed with a set of multiple interleaved superconducting circuits, making them ideal for detecting multi-photon coincidences. Each superconducting circuit can act as an independent detector (Figure 7.8b). As a result, multiple photons can be detected simultaneously by a single SNSPD array, eliminating the need for beam splitters at the device output. Using an SNSPD array consisting of four interleaved circuits, all three photons in a triplet can be detected.

The probability of detecting all three photons in a triplet drops to 13%, compared to a single photon detection efficiency of 70% because each photon that is detected by the SNSPD saturates one of the four superconducting circuits until it can reset, reducing the probability that the remaining photons in the triplet are successfully detected. The probability of successfully detecting all photons in a triplet is given by:

$$P_{\text{Tdetection}} = P_{\text{photon1}} \times P_{\text{photon2}} \times P_{\text{photon3}} = 0.7 \times 0.525 \times 0.35 = 0.13 \qquad (7.11)$$

This compares favorably to the probability of detecting three-photon coincidences using beam splitters and SPADs by over an order of magnitude.

7.7 Experimental results

In this section we summarize and discuss experimental results achieved thus far in the direction of producing photon triplets using polycrystalline anatase TiO_2 nanoscale waveguides. We will begin by describing details of linear loss and THG characterization of devices. We have completed some characterization of fluorescence in our devices and provide a summary of these results. Based on the results of these measurements, we will provide predictions of expected photon triplet conversion efficiencies, maximum pump powers, and maximum expected generation and detection rates of photon triplets. This expands on the theoretical results given in Chapter 6 and provides a comparison between predicted generation rates and expected photon triplet detection rates.

7.7.1 Results from device characterization

We have observed significant variation in waveguide propagation losses between fabricated devices and for different light polarizations. The lowest measured losses achieved to-date in polycrystalline anatase TiO_2 waveguides were measured by extracting losses from ring resonators, with a minimum loss value of 4 dB/cm and average loss of 5.8 dB/cm at 1550 nm [62]. These losses are comparable to those measured by top-view imaging of scattered light from waveguides [**?**] and those estimated from direct transmission measurements. However, these low losses are not consistent across all fabricated devices, with propagation losses typically ranging between 4–10 dB/cm, highlighting the importance of characterizing losses to select the best devices and before using polishing to define the waveguide length for TOSPDC measurements.

Additionally, we have observed that the loss for TM-polarized light in the infrared is more consistently low. In some devices the propagation loss for TE-polarized light is higher by approximately 3–6 dB/cm, which will significantly impact the efficiency of photon triplet generation. We hypothesize that this difference in propagation loss may be a result of sidewall roughness introduced by the etch process when defining waveguides. This is often the most unpredictable step during device fabrication. TE-polarized modes, with their E-field polarized in the plane of the device, have greater intensity at the sidewalls and thus will experience greater scattering as a result of sidewall roughness. TM-polarized modes have greater intensity near the top and bottom surfaces of the waveguide. The bottom surface is atomically smooth when the TiO_2 film is deposited on thermal oxide and the roughness of the top sur-

face is defined by film roughness. As a result, polarization-dependent measurements of propagation losses are important.

We presented THG results in Chapter 6, Section 6.5.2 and Figure 6.5. These results show strong agreement between the calculated THG wavelengths and intensities, based on the input IR pump spectrum and pump and signal mode dispersions, and measured THG signal. The key deviation between the calculated and measured values is a THG signal broadening of approximately 3 nm, which can be explained by width variations along the length of the waveguide of approximately ± 5 nm and thickness variations of ± 2 nm.

Based on the broadening of the THG signal spectrum, we can estimate the broadening of the TOSPDC spectrum we would expect when pumping the device with a visible pump. This can help us inform our decision of pump wavelength. The narrowest TOSPDC spectrum would be achieved by pumping with a laser at the center of the THG spectrum; however, due to variations in the phase-matching conditions along the waveguide, this would result in the pump being red-detuned from the phase-matched wavelength for part of the propagation length. As a result, the TOSPDC signal would be reduced by as much as half. Due to the width of the THG spectrum, a pump centered at the THG spectrum will be detuned from the phase-matching condition by approximately 1.5–2 nm at some points along the waveguide, which will broaden the signal spectrum by 200–300 nm. In order to maximize TOSPDC signal, a pump wavelength can be chosen at the blue edge of the THG spectrum. In this situation, the pump will always be blue-detuned from the PPM wavelength, allowing for generation of photon triplets. However, in this case

the pump will be detuned from the PPM wavelength by as much as 4–5 nm at some points in the waveguide, broadening the spectrum by 400–500 nm. These trade-offs must be considered when aiming to complete a measurement of TOSPDC and this highlights the need for improving fabrication to ensure uniform waveguide dimensions along millimeters of length.

7.7.2 Fluorescence characterization

Fluorescence in TiO_2 is low due to the indirect band gap of the material. As a result, attempted measurements of fluorescence from TiO_2 thin films using standard (non-single photon) detectors have yielded no signal above the detector noise. However, owing to the long interaction lengths in nanoscale waveguides and sensitivity of detectors used for attempted measurements of photon triplets, it becomes obvious that some fluorescence is generated in the TiO_2 waveguide core, thermal oxide bottom cladding, top cladding of the device, or through interactions of scattered pump photons with the silicon substrate.

During initial attempts at measuring TOSPDC, we used a combination of a high-sensitivity InGaAs camera to image the output mode from TiO_2 waveguides and a femtowatt detector to measure the output spectrum. A 532-nm laser was used to pump the waveguide. The output mode was imaged by collecting the waveguide output using a 0.85-NA objective and imaging the output with the InGaAs camera (Figure 7.9a). Based on the sensitivity of the camera, on the order of 10^4 IR photons per second must exit the waveguide for the signal to be measureable. The spectrum was measured by sending the output of the objective through a dispersive

prism and translating the femtowatt detector through the spectrally separated output (Figure 7.9b). A long integration time on the order of 10 hours was necessary to collect this spectrum due to the low generation rate of fluorescence photons. In the case of both measurements, detection rates were several orders of magnitude higher than what can feasibly be generated in our waveguides via TOSPDC. This leaves fluorescence as the likely source.

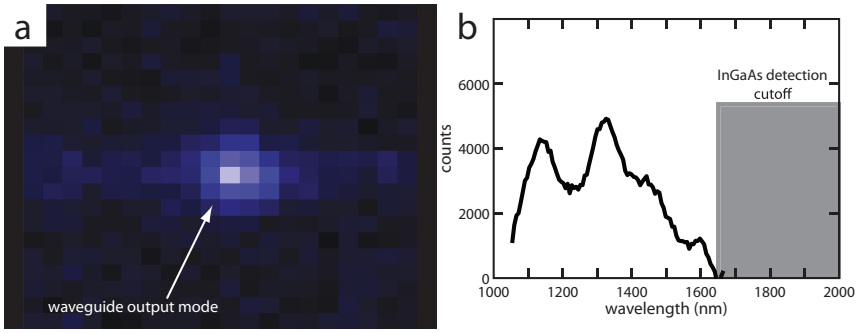

Figure 7.9: (a) Image of the output mode of a TiO_2 waveguide taken with a high-sensitivity InGaAs camera. (b) Spectrum of the infrared output. The output is spectrally separated using a dispersive prism and measured by translating a femtowatt detector along the spectrally separated output. The waveguide is pumped at 532 nm and a 650-nm shortpass filter is placed in the output beam path before the camera to filter out residual pump light. The source of the signal is likely fluorescence generated by the TiO_2 waveguide core or the top and bottom cladding materials (SiO_2). The peak near 1150 nm may be a result of fluorescence from the silicon substrate interacting with scattered pump light.

We use the TOSPDC measurement setup (Figure 7.6) to estimate the conversion efficiency from pump photons to fluorescence photons in devices with different top cladding materials. The top cladding is the material we can most easily replace in the device design and can thus be chosen to minimize noise due to fluorescence photons. Additionally, we test SU-8 waveguides for fluorescence because SU-8 coupling

Table 7.1: Fluorescence generation coefficient for different combinations of waveguide core and top cladding. The fluorescence coefficient ξ_{fl} gives the number of fluorescence photons produced per pump photon per cm propagation length within the waveguide.

	TiO_2 + Cytop	TiO_2 + $LfSiO_2$	TiO_2 + $HfSiO_2$	TiO_2 no cladding	SU-8 + Cytop
WG length (mm)	7	7	7	7	7
α_{P} (dB/cm)	30	30	30	50	2
α_{S} (db/cm)	8	8	8	30	1
α_{output} (dB)	6	6	6	6	5
ξ_{fl}	2×10^{-9}	1×10^{-9}	3×10^{-10}	4×10^{-9}	2×10^{-9}

pads can be used to reduce coupling losses in the infrared. Due to the low rate of fluorescence generation compared to the noise in the InGaAs camera and femtowatt detector used for the previous two measurements, switching to single photon counters provides greater accuracy for estimating the conversion efficiency to fluorescence photons. Additionally, we use a series of longpass filters with cut on wavelengths of 650, 1000, 1150, 1200, 1300, 1350, 1400, 1450, and 1500 nm and optical density > 5 in the stop band to estimate the spectral density of fluorescence photons in the IR. This information can be used to inform decisions of pump wavelength for TOSPDC, based on the center wavelength of the signal, signal bandwidth, and the wavelength of strong fluorescence signal from the device. Filters can then be introduced into the signal beam path during measurements to reduce noise from wavelength regimes with high fluorescence rates.

We compare fluorescence from devices clad in Cytop (a fluoropolymer), SiO_2 de-

posited using low frequency PECVD ($LfSiO_2$), SiO_2 deposited using high frequency PECVD ($HfSiO_2$), and no cladding. Additionally we measure fluorescence in SU-8 waveguides clad in Cytop. The bottom cladding in all cases is thermal oxide with thickness $>3\mu$m on silicon. We estimate the fluorescence coefficient from measured fluorescence rates, device length, and estimated pump and signal losses using a re-arranged version of Equation 7.2 which takes into account the photon losses at the device output and photon detection efficiency:

$$\zeta_{\mathrm{fl}} = \frac{R_{\mathrm{fl}}(\alpha_{\mathrm{P}} - \alpha_{\mathrm{S}})}{N_{\mathrm{P0}}(e^{-\alpha_{\mathrm{S}}L} - e^{-\alpha_{\mathrm{P}}L})} e^{\alpha_{\mathrm{output}}} e^{\alpha_{\mathrm{detection}}} \tag{7.12}$$

Estimated fluorescence coefficients for these devices are given in Table 7.1. We find the lowest fluorescence rates in TiO_2 waveguides clad in $HfSiO_2$ and propagation losses comparable to waveguides cladded in Cytop and $LfSiO_2$. SU-8 waveguides are found to produce significant fluorescence at wavelengths $<$1000 nm, which makes them useful for lowering coupling losses at the output end of the device, provided that efficient longpass filters are used to remove visible and near infrared fluorescence. Estimates of the fluorescence spectral density in TiO_2 waveguides clad with $HfSiO_2$ and SU-8 waveguides are given in Figure 7.10. If TOSPDC devices can be designed and fabricated to produce narrow-band signal centered at 1600 nm, filters can be used to remove a majority of the fluorescence produced in the device, significantly lowering the impact of fluorescence on photon triplet measurements.

7.7.3 Expected experimental device performance

Based on the measurements of fluorescence in TOSPDC devices presented in Section 7.7.2 and photon triplet generation efficiencies presented in Chapter 6, we

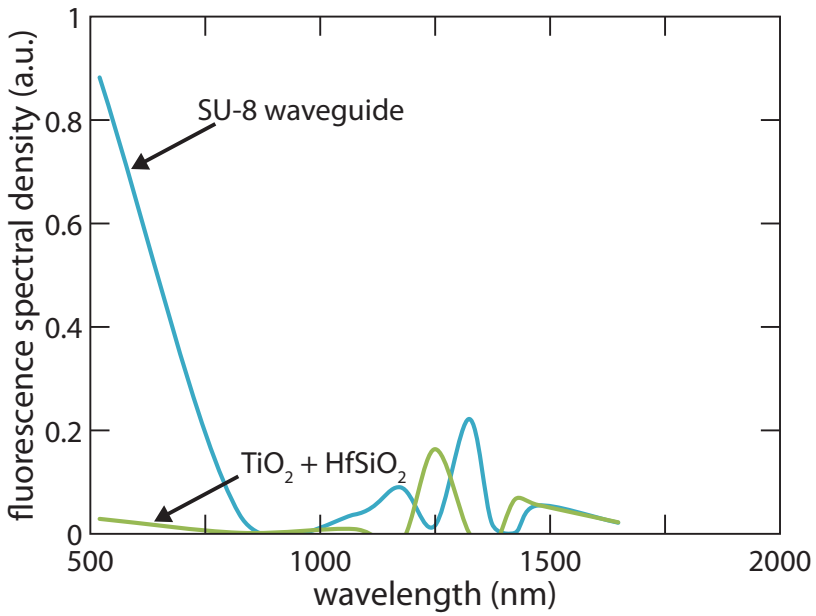

Figure 7.10: Estimated fluorescence spectral density in a TiO_2 waveguide clad in $HfSiO_2$ and an SU-8 waveguide clad in Cytop when pumped with a CW 520-nm laser at approximately 2 mW of power. Due to the size of the SU-8 waveguide, the visible pump is well confined and fluorescence is likely only from the waveguide core. We note that in both waveguides there is significant fluorescence signal between 1200–1400 nm and that fluorescence appears to trail off for wavelengths > 1500 nm.

can estimate the maximum pump power we can use in our devices and the maximum attainable rate of photon triplet generation. We can use these generation rates, estimate device output losses, and detection efficiencies described in Section 7.6 to estimate the expected detection rate of photon triplets. These values are important for planning experimental demonstrations of TOSPDC and determining which aspects of the experiment are in greatest need of improvement.

We estimated a fluorescence generation coefficient for TiO_2 waveguides with $HfSiO_2$ cladding of 3×10^{-10} photons/pump photon/cm. We can reduce this fluores-

cence coefficient to 1×10^{-10} photons/pump photon/cm by introducing a 1300 nm longpass filter to remove all fluorescence photons generated at shorter wavelengths. We can rearrange Equation 7.4:

$$\zeta_{\mathrm{T}} = \frac{R_{\mathrm{T}}(\alpha_{\mathrm{P}} - 3\alpha_{\mathrm{S}})}{N_{\mathrm{P0}}(e^{-3\alpha_{\mathrm{S}}L} - e^{-\alpha_{\mathrm{P}}L})} \tag{7.13}$$

Note that we do not include a factor for the output beam path losses or detector efficiency because the photon triplet generation rate is calculated at the end facet of the waveguide. Assuming a photon triplet generation efficiency of 0.1 triplets/s/mW of pump power, we estimate a photon triplet generation coefficient of 4×10^{-15}.

We defined Equation 7.6 to calculate the maximum pump power. For experimental systems, we need to include the effects of output losses and detector efficiency for the conversion efficiency terms, ρ_{T} and ρ_{fl}. The effects of output losses and detector efficiency will be more severe on photon triplet detection because all three photons must survive and be detected to measure a three-photon coincidence. We find $\rho_{\mathrm{T}} = 8 \times 10^{-20}$ and $\rho_{\mathrm{fl}} = 6 \times 10^{-12}$. Assuming a correlation time of 500 ps for photon triplet detection, we find a maximum pump rate of $N_{P0} = 4 \times 10^{16}$ per second or 16 mW at 532 nm.

Using a pump power of 16 mW, we would expect a photon triplet generation rate of 1.6 triplets/s. Assuming output beam path losses, including coupling losses, of 6 dB and a photon triplet detection efficiency of approximately 13% using SNSPDs, we expect to detect approximately 200 photon triplets per hour.

7.8 Conclusion and outlook for experimental demonstrations of TOSPDC

Although our photon triplet generation efficiencies are higher than previous theoretical predictions in silica fibers [104] and experimental demonstrations using SPDC in nonlinear crystals [97,99], our expected detection rates fall short of the highest rates demonstrated by Hamel et al. (2014) [99]. The reasons for this shortcoming include low maximum pump power due to fluorescence, high losses in the output beam path, and statistical detection of photon triplets. Without implementation of SU-8 coupling pads on our devices or anti-reflective coatings at the signal wavelength, we cannot achieve coupling losses lower than approximately 3 dB at the output. The beam path at the output adds an additional 3 dB of loss before the signal reaches the detectors.

Compounding these challenges, all three signal photons leave the device in the same mode and are frequency degenerate if the device is pumped at the PPM wavelength. That leads to the statistical limitations of detecting all three photons using a set of SNSPDs or other single photon counters, as described in Section 7.6. In experimental demonstrations based on cascaded SPDC [97, 99], the phase-matching conditions are set up such that the signal photons are generated at different frequencies, allowing for spectral separation of the signal photons and much more efficient detection schemes. Even if we pump a TOSPDC-based source of photon triplets non-degenerately, many combinations of photon frequencies satisfy phase-matching. Thus, photon triplets cannot be separated deterministically based on frequency.

Lowering losses in TOSPDC-based devices will be critical to enabling experi-

mental demonstrations and practical devices. This will require improving fabrication to reduce losses due to fabrication imperfections and ensure consistent phase-matching conditions along the length of multi-mm waveguides. Additionally, better film deposition techniques could drastically reduce losses and increase photon triplet generation and detection rates. Epitaxially grown films are the ideal candidate. Removing the presence of grain boundaries may also reduce the prevalence of fluorescence due to a reduced defect concentration in the material.

Further characterization of fluorescence in TiO_2 and other constituent materials of TOSPDC devices will be important to provide accurate information and estimate the device performance. This should include careful measurements of the fluorescence spectrum for wavelengths $>$1600 nm and a measurement of fluorescence rate with respect to incident pump power. We have assumed a linear dependence of fluorescence on incident pump power, but for higher pump power, fluorescence saturation may set in, limiting fluorescence rates. Measurements of fluorescence lifetime in the device may also be useful when considering the use of pulsed pump operation of TOSPDC devices. In this case, gating the detection of photon triplets could provide a method of rejecting a majority of the fluorescence signal.

Chapter 8

Conclusion and outlook

In this dissertation we have discussed applications of nonlinear optical interactions in two general areas: 1) 3D direct laser writing and modification of materials utilizing nonlinear optical interactions and 2) taking advantage of light propagation and nonlinear optical interactions in nano-scale waveguides integrated on-chip.

Our work in the field of direct laser writing has been focused on developing methods for 3D patterning new material platforms and enabling new types of structures for optical applications. 3D fabrication of disconnected metal structures within a dielectric matrix (Chapter 3) overcomes key limitations in both lithographic and multiphoton polymerization techniques. These types of structures could have immediate applications toward diffractive optical elements and metamaterials. Laser modification of hydrogenated amorphous silicon (Chapter 4) has the potential of enabling 3D patterning optical waveguides and devices in a CMOS compatible platform with high index contrast. Due the importance of silicon-based devices and the increasing value of device density in modern integrated devices, both characteristics

are important. Both projects seek to address limitations in current state-of-the-art fabrication techniques.

Further study and optimization of both methods is necessary. The quality of the laser-written metal structures is limited by their composition. They tend to be composed of agglomerations of metal nanoparticles held together by the polymer matrix. This leads to a finite opacity and limited efficiency in the case of diffractive optical elements. Additionally, the size of the nanoparticles imposed a minimum roughness on the structures, which will ultimately limit the optical quality of diffractive elements. This can impact imaging and wavelength selection applications. It is possible that these properties can be further tuned by optimizing laser writing conditions, such as repetition rate, pulse energy, pulse duration, and number of pulses per unit area. Changing the polymer and metal salt chemistry can also impact final structures.

The electrical properties will also be impacted by the structure composition. Limited contact points between metal nanoparticles will reduce the conductivity relative to bulk metal. These properties must still be accurately measured in order to enable design of metamaterials. Measurement of conductivity on embedded 3D metal structures, however, is difficult. 4-point probe measurements require fabrication of structures at the substrate-polymer interface and lithographic patterning of macroscale metal contacts. These structures may also not be fully representative of metal structures in the bulk of the polymer due to the impacts of writing near the substrate. Another option is to use direct laser writing to fabricate metamaterials in the infrared or THz regime, measure the optical response, and compare to simulations. Mixing rules can be used to determine the electrical properties based on metal content in the

structure for the simulations to iterate and achieve a match between experimental and theoretical results. This brute-force method could be used to attain an estimate of the electrical properties of metal structures in the polymer bulk. Some additional details on this research direction are given in Appendix A.

Our work in integrated nonlinear nanophotonic devices has been focused on developing a new source of entangled photon triplets. We seek to provide a direct method of generating entangled triplets using a single nonlinear event by third-order spontaneous parametric down-conversion. Previous research has focused on utilizing cascaded spontaneous parametric downconversion or entangling multiple sets of pairs at beam splitters and doing post-selection to identify larger entangled states. Both schemes are difficult to scale up and direct generation of larger entangled states would simplify the process of producing larger entangled states. Additionally, entangled states produced by a third-order nonlinear process, rather than a second order process, may be advantageous in some quantum communication applications.

We predict photon triplet generation efficiencies in integrated TiO_2 nanoscale waveguides approximately one order of magnitude higher than previous experimental and theoretical works involving optical fibers and phase-matched schemes in nonlinear crystals. Enhanced conversion efficiency is absolutely critical for realizing practical experiments and demonstrations of quantum information applications. We have developed and presented methods for optimizing waveguides for achieving phase-matching and high effective nonlinearities between the pump and signal (Chapter 6), both of which are necessary conditions for high photon triplet generation rates. These methods have been verified using the reverse process, third-harmonic generation.

Experimental demonstrations of photon triplet generation have not yet been successful. This is a result of various challenges in the fabrication and characterization of devices, as well as shortcomings in the measurement schemes for three-photon entangled states (Chapter 7). Losses resulting from fabrication imperfections and grain boundaries in the TiO_2 films we deposit by sputtering greatly reduce the interaction lengths we can achieve between the visible pump and infrared signal modes in our waveguides. Perfecting waveguide fabrication techniques and film deposition methods to achieve lower losses will be critical for experimental work. Fluorescence in devices also limits the maximum pump power we can use in our devices and therefore places a limit on the maximum generation rates we can achieve in our devices. Improving film deposition for lower losses may also reduce the defects and impurities which contribute to fluorescence. Another option would be to explore other materials with more mature deposition and fabrication techniques in order to take advantage of lower losses and more consistent fabrication of devices. Lithium niobate is the best potential candidate, although fluorescence in this material platform may limit pump powers even more significantly than in TiO_2. These trade-offs should be explored. Although we predict relatively high photon triplet generation efficiencies in our TiO_2-based devices, losses in the device output and limited detection efficiencies for three-photon coincidences greatly reduces the expected photon triplet detection rate. This greatly complicates experimental demonstrations and long integration time is necessary to ensure sufficient signal counts for statistically significant data. These factors outline why significant challenges must still be overcome in order to demonstrate a photon triplet source based on TOSPDC experimentally.

Nonlinear optical interactions have vast numbers of applications in optics and photonics. The topics covered in this dissertation touch on only a small subset of these directions. Nevertheless, the potential impact of the research presented could be far-reaching in the fields of 3D fabrication, diffraction optics, metamaterials, integrated optics, and quantum information technology.

Appendix A

Extracting material properties of laser-written structures from THz resonance measurements

In this appendix we provide an experimental plan for how to determine the electrical properties of the metal structures fabricated by direct laser writing. We will provide information on the simulation and fabrication methods that have been attempted so far, as well as information on what the current challenges are that will need to be addressed to make successful measurements.

The electrical properties of laser-written metal structures must be understood and determined properly in order enable efficient design and fabrication of meta-material structures. This is because the electrical response of the metal structures contained in the dielectric matrix is crucial to producing the desired optical response of the effective medium. The electrical properties will depend on the composition of

the metal structures. Based on TEM measurements of laser-fabricated silver structures, it is clear that the fabrication technique produces silver nanoparticles embedded within the polymer matrix (Figure A.1). The volume fraction of silver and the amount

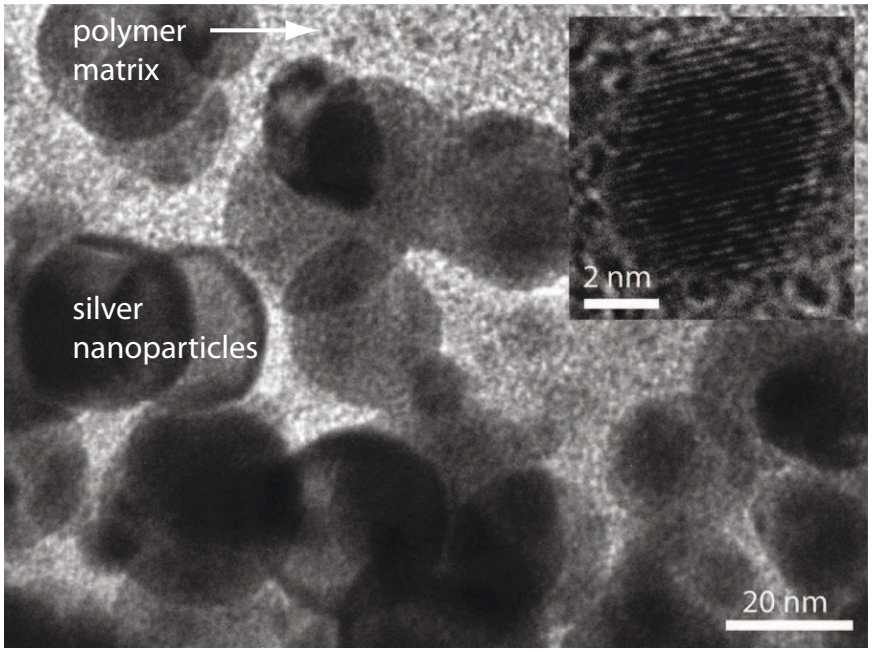

Figure A.1: TEM image of silver nanoparticles produced by direct laser writing. We see that the nanoparticle size ranges from 5–30 nm. This image is from Vora et al. 2012 [27].

and area of contact points between silver structures will strongly impact the electrical properties. However, direct measurements are not easy.

4-point probe measurements would be the go-to method for determining conductive properties of such structures. However, laser fabrication does not lend itself to producing large, connected regions of metal to make good contact points for this technique. Additionally, our structures are embedded within a bulk polymer layer. As a result, accessing the fabricated structure is not simple. One work-around would be to fabricate the metal structures at the interface between the substrate and polymer

layer and to remove the polymer after fabrication. Additionally, lithographic techniques could be employed to deposit contacts on top of the laser-fabricated structure and use these as the contact points for the 4-point probe measurement. This, however, may not give an accurate estimate of the electrical properties of structures fabricated in the bulk because fewer metal ions will be near the fabrication region because metal ions can only diffuse in to the focal region during laser writing from above. Additionally, fabrication at the substrate-polymer interface can shift the exposure parameters due to reflections and interactions with the substrate.

Instead we are pursuing the use of material property retrieval from optical transmission measurements. We have designed resonance structures in the THz range within the transparency window of the gelatin matrix material (Figure A.2). The

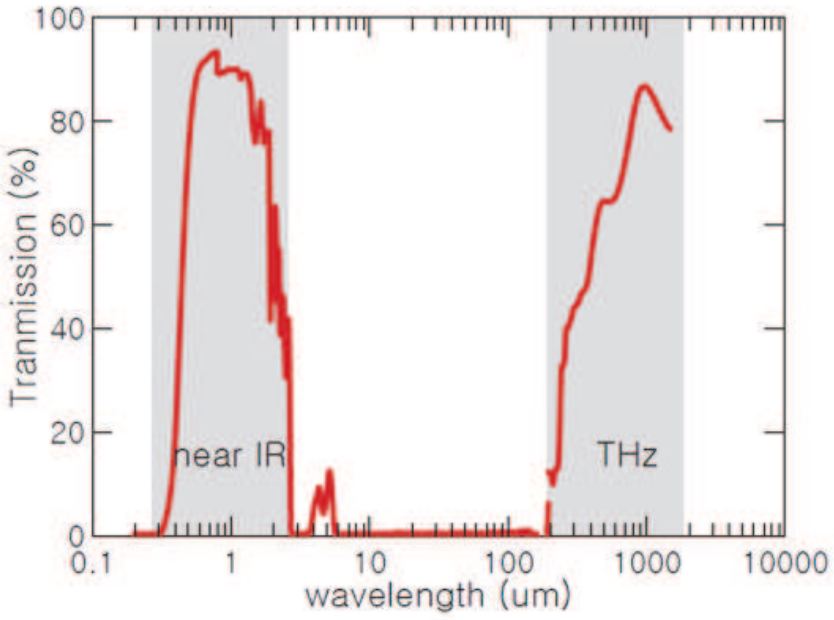

Figure A.2: Plot of the transparency window of gelatin. The material is reasonably transparent around 1 THz. This figure is from SeungYeon Kang's thesis [29].

transmission and reflection properties of these structures can then be calculated via FDTD simulations, assuming a given set of material properties for the fabricated silver structures. The material properties can be predicted based on mixing rules and the volume fraction of silver. Following fabrication of the structures, they can be measured with THz frequency time-domain spectroscopy [127–130]. The assumed volume fraction of silver for the calculation of the material properties of the fabricated structure can be adjusted until a match is found between the measured and predicted optical response. This is a brute force method, but can enable an estimate of the actual electrical properties of fabricated silver structures in the bulk of the polymer layer.

Figure A.3 shows the proposed geometry for the THz frequency measurements of laser-fabricated samples. We use z-cut quartz as the substrate in order to ensure high transmission in the THz regime. Because only a single layer of structures is necessary for this measurement, the thickness of the gelatin layer could be reduced below 100 μm in order to boost the transmission of the sample. The extent of the fabricated structures in the plane of incidence is determined by the minimum spot size attainable in the THz measurement. This is typically between 5 to 10 mm.

Simple resonant structures with a low filing fraction relative to the area of the sample are preferable because this reduces the fabrication time for the sample. We have chosen to design and fabricate ring resonator structures, as shown schematically in Figure A.4. The dimensions of individual rings are all on the micrometer scale, making them easy to fabricate via direct laser writing. Smaller structures could easily be fabricated with the minimum feature sizes ($<$ 100 nm) and resolutions (500 nm)

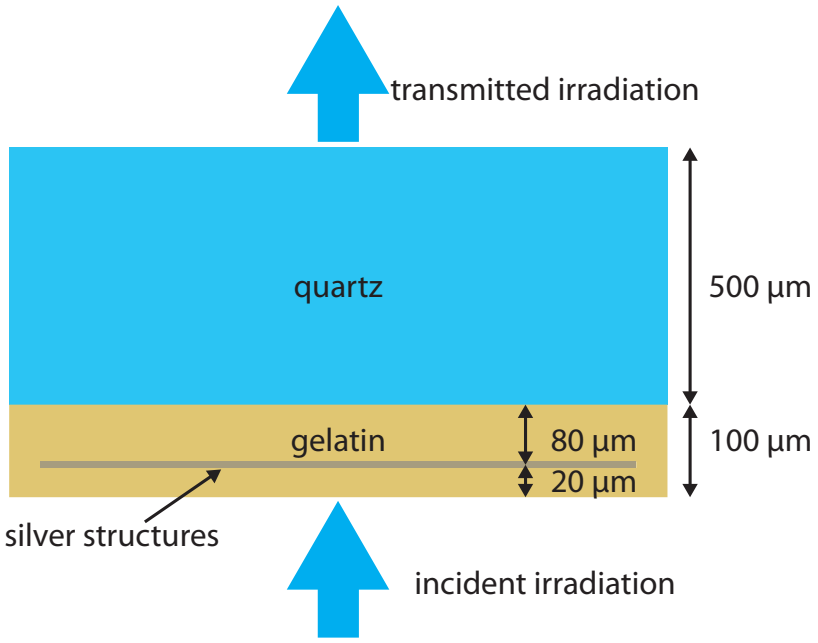

Figure A.3: Schematic of the geometry for measuring transmission of laser-fabricated samples in the THz regime. The sample size in the plane of incidence is between 5 × 5 and 10 × 10 mm.

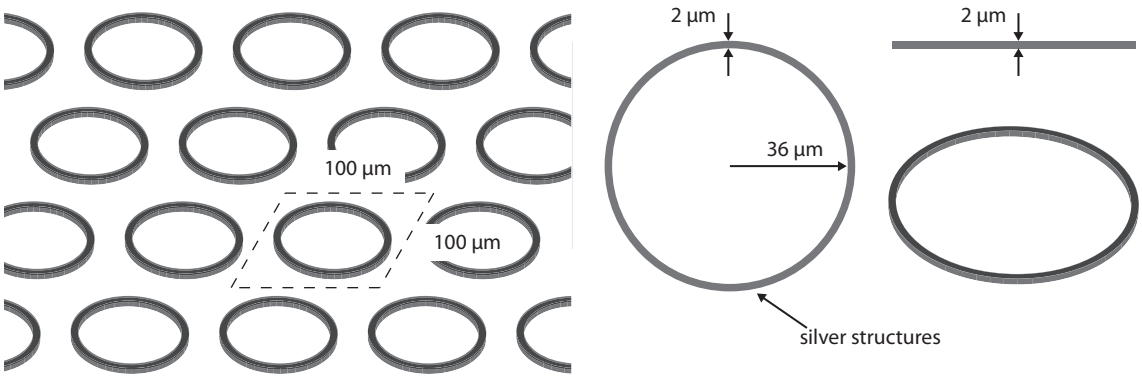

Figure A.4: Schematic *(left)* of an array of THz ring resonators and *(right)* a single resonator. The array is in the plane of incidence of the THz radiation shown in Figure A.3. The dimensions of the structures are well within the range of sizes that can easily be fabricated by direct laser writing.

demonstrated in previous experiments. Figure A.5 shows part of a fabricated array of resonators.

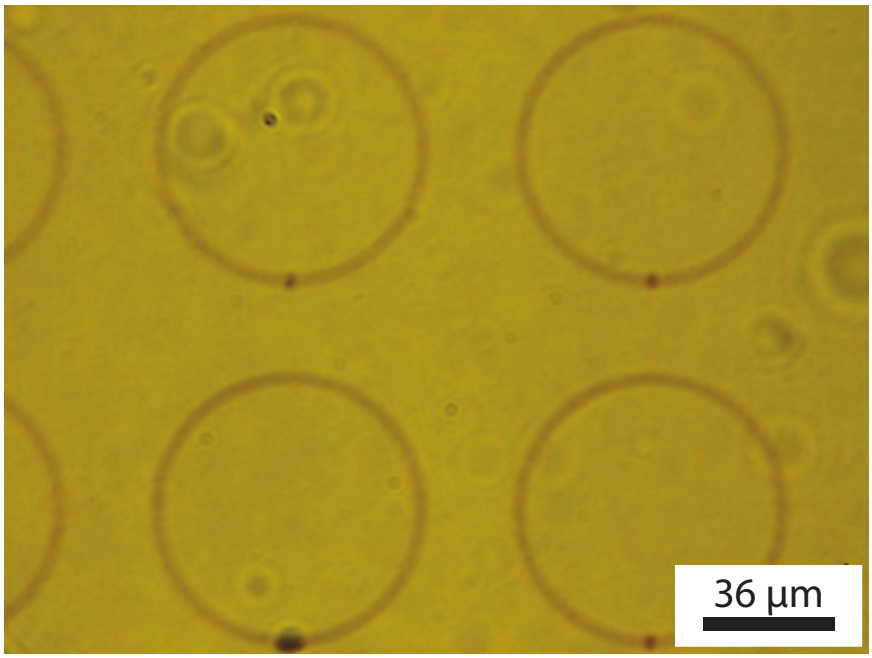

Figure A.5: Optical image of a small section of a fabricated array of THz ring resonators. Defects in the polymer matrix and fabricated structures are visible. As long as these defects remain much smaller than the incident THz radiation and are relatively evenly distributed across the sample, they should not significantly impact the measurement.

The calculated transmission of the structures shown above is given in Figure A.6. The Q-factor for this structure is relatively low. Because the transmission dip will be lower if the conductivity of the fabricated silver structures is significantly lower than bulk silver, this could pose a problem for measurements of the structure. As the conductivity of the fabricated silver becomes lower with respect to bulk silver, the transmission dip will become less pronounced and will become more difficult to measure.

Although THz resonant structures have been successfully fabricated in large

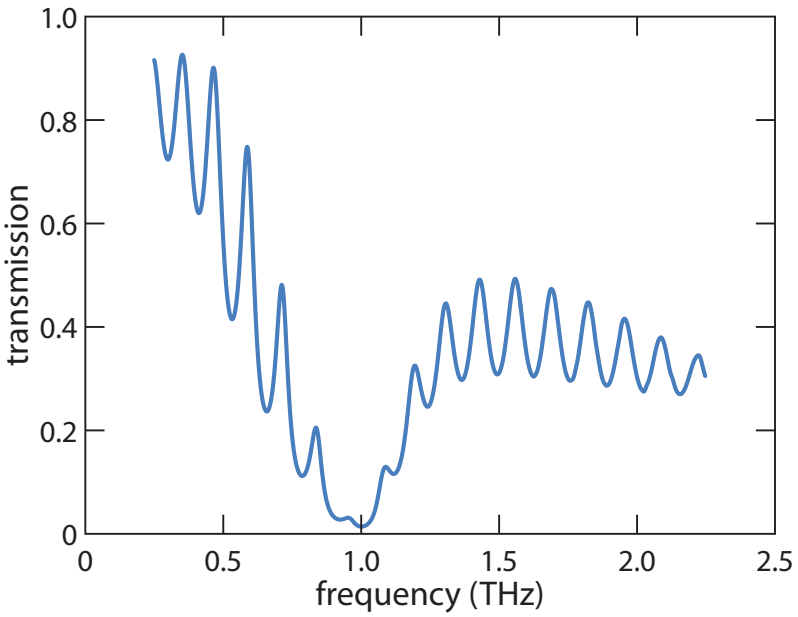

Figure A.6: Calculated transmission spectrum for the resonant structures shown in Figures A.4 and A.5. The oscillations in the calculated transmission spectrum are a result of interference within the gelatin and substrate layers.

enough areas to measure, measurements have not been conclusive to-date. One of the biggest issues revolves around sample packaging. The gelatin layer will dry out if exposed to a very dry outside environment. THz radiation is strongly absorbed by moisture. As a result, doing THz measurements in air is difficult and subject to significant noise, which makes it difficult to extract a transmission dip in the measured data. Nitrogen purging the measurement chamber does greatly reduce the noise, however, the gelatin quickly dries and cracks under these conditions, making measurements impossible. For future measurements, the sample will need to be packaged within a coating that prevents the escape of water moisture from the gelatin.

The substrate poses additional issues. Z-cut quartz does absorb some THz radiation. As a result, thinner substrates would be preferable. However, the stress

exerted by the gelatin layer as it cures can lead to bending of the substrate and failure if it is too thin. Flexing of the substrate during the laser fabrication process can lead to misalignment of the laser-fabricated structures. This effect is most pronounced in the z-direction (on the order of several micrometers) and could cause a problem for more complex resonant structures. As a result, we have found that the quartz layer must be at least 0.5–1 mm thick to ensure stability of the sample.

Lastly, the mixing rules used to predict conductivity of the fabricated silver structures must be chosen carefully. The Maxwell-Garnett mixing rules are generally applicable for low volume fractions [131], but are not well-suited for large variations in volume fraction of silver. Adjusting the formulation of the Maxwell-Garnett mixing rules may be one method of addressing this shortcoming [132]. Alternatively, a different model may need to be chosen for these structures which properly takes into account relatively large volume fractions of silver and can account for the effects of point contact between the silver structures on the calculated conductivity of the structures on the micrometer scale.

Acknowledgements

Several individuals contributed to this work. Yang Li designed and simulated the THz metamaterial structures and investigated the mixing rules related to calculating electronic properties using material mixing rules. Michael Moebius advised the design, simulation, and material modeling process and completed sample preparation and laser fabrication of the structures. Renee Sher completed measurements of samples at SLAC and advised on sample packaging methods for future work.

Bibliography

[1] R A Shelby, D R Smith, and S Schultz, Science **292**, 77 (2001).

[2] D R Smith, J B Pendry, and M C Wiltshire, Science **305**, 788 (2004).

[3] Vladimir M. Shalaev, Nature Photonics **1**, 41 (2007).

[4] Costas M Soukoulis and Martin Wegener, Nature Photonics **5**, 1 (2011).

[5] Christopher N. LaFratta, John T. Fourkas, Tommaso Baldacchini, and Richard A. Farrer, Angewandte Chemie - International Edition **46**, 6238 (2007).

[6] R Gattass and E Mazur, Nature Photonics **2**, 219 (2008).

[7] Georg von Freymann, Alexandra Ledermann, Michael Thiel, Isabelle Staude, Sabine Essig, Kurt Busch, and Martin Wegener, Advanced Functional Materials **20**, 1038 (2010).

[8] L Li, R. R. Gattass, E Gershgoren, H Hwang, and J. T. Fourkas, Science **324**, 910 (2009).

[9] Wojciech Haske, Vincent W Chen, Joel M Hales, Wenting Dong, Stephen Barlow, Seth R Marder, and Joseph W Perry, Optics express **15**, 3426 (2007).

[10] Jin Feng Xing, Xian Zi Dong, Wei Qiang Chen, Xuan Ming Duan, Nobuyuki Takeyasu, Takuo Tanaka, and Satoshi Kawata, Applied Physics Letters **90**, 31 (2007).

[11] Dengfeng Tan, Yan Li, Fengjie Qi, Hong Yang, Qihuang Gong, Xianzi Dong, and Xuanming Duan, Applied Physics Letters **90**, 071106 (2007).

[12] Robert W Boyd, *Nonlinear Optics*, 3rd ed. (Elsevier, Burlington, MA USA, 2008).

[13] Chris B Schaffer, André Brodeur, and Eric Mazur, Measurement Science and Technology **12**, 1784 (2001).

[14] L. V. Keldysh, Journal of Experimental and Theoretical Physics **20**, 1307 (1965).

[15] Peter Y. Yu and Manuel Cardona, *Fundamentals of Semiconductors* (Springer Berlin Heidelberg, Berlin, Heidelberg, 1996).

[16] B C Stuart, M D Feit, S Herman, A M Rubenchik, B W Shore, and M D Perry, Physical Review B **53**, 1749 (1996).

[17] D Du, X Liu, G Korn, J Squier, and G Mourou, Applied Physics Letters **64**, 3071 (1994).

[18] D. Du, X. Liu, and G. Mourou, Applied Physics B: Lasers and Optics **63**, 617 (1996).

[19] An-Chun Tien, Sterling Backus, Henry Kapteyn, Margaret Murnane, and Gérard Mourou, Physical Review Letters **82**, 3883 (1999).

[20] Chris B Schaffer, Alan O Jamison, and Eric Mazur, Applied Physics Letters **84**, 1441 (2004).

[21] Florian Formanek, Nobuyuki Takeyasu, Takuo Tanaka, Kenta Chiyoda, Atsushi Ishikawa, and Satoshi Kawata, Optics express **14**, 800 (2006).

[22] N. Takeyasu, T. Tanaka, and S. Kawata, Applied Physics A: Materials Science and Processing **90**, 205 (2008).

[23] Michael S. Rill, Christine Plet, Michael Thiel, Isabelle Staude, Georg von Freymann, Stefan Linden, and Martin Wegener, Nature Materials **7**, 543 (2008).

[24] Koshiro Kaneko, Kazuo Yamamoto, Satoshi Kawata, Hong Xia, Jun-feng Song, and Hong-bo Sun, Optics letters **33**, 1999 (2008).

[25] Justyna K Gansel, Michael Thiel, Michael S Rill, Manuel Decker, Klaus Bade, Volker Saile, Georg von Freymann, Stefan Linden, and Martin Wegener, Science **325**, 1513 (2009).

[26] T Baldacchini, A.-C. Pons, J Pons, C N LaFratta, J T Fourkas, Y Sun, and M J Naughton, Optics Express **14**, 1275 (2005).

[27] Kevin Vora, SeungYeon Kang, and Eric Mazur, Journal of Visualized Experiments (2012).

[28] Kevin Vora, SeungYeon Kang, Shobha Shukla, and Eric Mazur, Applied Physics Letters **100**, 063120 (2012).

[29] SeungYeon Kang, Ph.D. thesis, Harvard University, 2014.

[30] Kevin Vora, SeungYeon Kang, Michael Moebius, and Eric Mazur, Applied Physics Letters **105**, 141114 (2014).

[31] SeungYeon Kang, Kevin Vora, and Eric Mazur, Nanotechnology **26**, 121001 (2015).

[32] A H Nejadmalayeri, P R Herman, J Burghoff, M Will, S Nolte, and A Tunnermann, Optics Letters **30**, 964 (2005).

[33] C M Fortmann, Physical Review Letters **81**, 3683 (1998).

[34] Wataru Futako, Toshio Kamiya, Charles M Fortmann, and Isamu Shimizu, Journal of Non-Crystalline Solids **266-269**, 630 (2000).

[35] C.M Fortmann, E.L Jaen, N Hata, W.A Anderson, and A.H Mahan, Thin Solid Films **395**, 142 (2001).

[36] C.M. Fortmann, A.H. Mahan, Scott Ward, W.A. Anderson, R. Tonucci, and N. Hata, Thin Solid Films **430**, 278 (2003).

[37] C Fortmann, J Mawyin, R Tonucci, and A Mahan, Thin Solid Films **501**, 350 (2006).

[38] Ethan Schonbrun, Adam R Abate, Paul E Steinvurzel, David a Weitz, and Kenneth B Crozier, Lab on a chip **10**, 852 (2010).

[39] Toufic G Jabbour, Ph.D. thesis, University of Central Florida, 2009.

[40] M. C. Hutley and R. F. Stevens, J. Phys. E: Sci. Instrum. **21**, 1037 (1988).

[41] Henry I. Smith, Rajesh Menon, Amil Patel, David Chao, Michael Walsh, and G. Barbastathis, Microelectronic Engineering **83**, 956 (2006).

[42] P. L. Gourley, M. E. Warren, G. A. Vawter, T. M. Brennan, and B. E. Hammons, Applied Physics Letters **60**, 2714 (1992).

[43] C M Anderson and K P Giapis, Physical Review B **56**, 7313 (1997).

[44] S. Riechel, C. Kallinger, U. Lemmer, J. Feldmann, A. Gombert, V. Wittwer, and U. Scherf, Applied Physics Letters **77**, 2310 (2000).

[45] J. F. Galisteo-López and C. López, Physical Review B - Condensed Matter and Materials Physics **70**, 1 (2004).

[46] A. V. Baryshev, V. A. Kosobukin, K. B. Samusev, D. E. Usvyat, and M. F. Limonov, Physical Review B - Condensed Matter and Materials Physics **73**, 1 (2006).

[47] V. A. Bushuev, B. I. Mantsyzov, and A. A. Skorynin, Physical Review A - Atomic, Molecular, and Optical Physics **79**, 1 (2009).

[48] J. Manzanares-Martinez, P. Castro-Garay, E. Urrutia-Banuelos, D. Moctezuma-Enriquez, R. Archuleta-Garcia, and M. Velarde-Chong, A, Adv. Stu- dies Theor. Phys. **15**, 551 (2011).

[49] Björn Brüser, Isabelle Staude, Georg von Freymann, Martin Wegener, and Ullrich Pietsch, Appl. Opt. **51**, 6732 (2012).

[50] F. García-Santamaría, J. F. Galisteo-López, P. V. Braun, and C. López, Physical Review B **71**, 195112 (2005).

[51] Luis A Dorado, Ricardo A Depine, Daniel Schinca, Gabriel Lozano, and Hernán Míguez, Physical Review B **78**, 075102 (2008).

[52] Jigang Wu, Guoan Zheng, and Lap Man Lee, Lab on a Chip **12**, 3566 (2012).

[53] Zoltan Gorocs and Aydogan Ozcan, IEEE Reviews in Biomedical Engineering **6**, 29 (2013).

[54] Ethan Schonbrun, Charles Rinzler, and Kenneth B Crozier, Applied Physics Letters **92**, 071112 (2008).

[55] Mohammad J. Moghimi, Jayer Fernandes, Aditi Kanhere, and Hongrui Jiang, Scientific Reports **5**, 15861 (2015).

[56] Grégoire R. Chabrol, Adline Ciceron, Patrice Twardowski, Pierre Pfeiffer, Manuel Flury, Frédéric Mermet, and Sylvain Lecler, Applied Surface Science 8 (2016).

[57] Kevin Vora, Ph.D. thesis, Harvard University, 2014.

[58] M H Brodsky, M Cardona, and J J Cuomo, Physical Review B **16**, 3556 (1977).

[59] Jennifer T Choy, Jonathan D B Bradley, Parag B Deotare, Ian B Burgess, Christopher C Evans, Eric Mazur, and Marko Loncar, Optics Letters **37**, 539 (2012).

[60] Christopher C Evans, Katia Shtyrkova, Jonathan D B Bradley, Orad Reshef, Erich Ippen, and Eric Mazur, Optics Express **21**, 18582 (2013).

[61] Christopher C. Evans, Katia Shtyrkova, Orad Reshef, Michael Moebius, Jonathan D. B. Bradley, Sarah Griesse-Nascimento, Erich Ippen, and Eric Mazur, Optics Express **23**, 7832 (2015).

[62] Orad Reshef, Katia Shtyrkova, Michael G. Moebius, Sarah Griesse-Nascimento, Steven Spector, Christopher C. Evans, Erich Ippen, and Eric Mazur, Journal of the Optical Society of America B **32**, 2288 (2015).

[63] Hermann Haus, *Waves and Fields in Optoelectronics* (Prentiss Hall, ADDRESS, 1983).

[64] Amnon Yariv and Pochi Yeh, *Photonics: Optical Electronics in Modern Communications* (Oxford University Press, ADDRESS, 2007).

[65] C C Evans, Ph.D. thesis, Harvard University, 2014.

[66] Richard Soref, IEEE Journal of Selected Topics in Quantum Electronics **12**, 1678 (2006).

[67] Aleksandr Biberman, Michael J. Shaw, Erman Timurdogan, Jeremy B. Wright, and Michael R. Watts, Optics Letters **37**, 4236 (2012).

[68] Hansuek Lee, Tong Chen, Jiang Li, Oskar Painter, and Kerry J. Vahala, Nature Communications **3**, 867 (2012).

[69] Guoliang Li, Jin Yao, Hiren Thacker, Attila Mekis, Xuezhe Zheng, Ivan Shubin, Ying Luo, Jin-hyoung Lee, Kannan Raj, John E. Cunningham, and Ashok V. Krishnamoorthy, Optics Express **20**, 12035 (2012).

[70] Shankar Kumar Selvaraja, Wim Bogaerts, and Dries Van Thourhout, Optics Communications **284**, 2141 (2011).

[71] Surya Cheemalapati, Mikhail Ladanov, John Winskas, and Anna Pyayt, Applied Optics **53**, 5745 (2014).

[72] A B Seddon, Journal of Non-Crystalline Solids **184**, 44 (1995).

[73] A M Andriesh and M S Iovu, Moldavian Journal of the Physical Sciences **2**, 246 (2003).

[74] Vahid Ta'eed, Neil J Baker, Libin Fu, Klaus Finsterbusch, Michael R E Lamont, David J Moss, Hong C Nguyen, Benjamin J Eggleton, Duk-Yong Choi, Steven Madden, and Barry Luther-Davies, Optics Express **15**, 9205 (2007).

[75] C Xiong, L G Helt, A C Judge, G D Marshall, M J Steel, J E Sipe, and B J Eggleton, Optics Express **18**, 16206 (2010).

[76] C Xiong, G D Marshall, A Peruzzo, M Lobino, A S Clark, D Y Choi, S J Madden, C M Natarajan, M G Tanner, R H Hadfield, S N Dorenbos, T Zijlstra, V Zwiller, M G Thompson, J G Rarity, M J Steel, B Luther-Davies, B J Eggleton, and J L O'Brien, Applied Physics Letters **98**, 51101 (2011).

[77] K. T. Vu and S. J. Madden, Journal of Vacuum Science & Technology A: Vacuum, Surfaces, and Films **29**, 011023 (2011).

[78] Alexander Gondarenko, Jacob S. Levy, and Michal Lipson, Optics Express **17**, 11366 (2009).

[79] Jacob S Levy, Mark A Foster, Alexander L Gaeta, and Michal Lipson, Optics Express **19**, 11415 (2011).

[80] Sebastian Romero-García, Florian Merget, Frank Zhong, Hod Finkelstein, and Jeremy Witzens, Optics Express **21**, 14036 (2013).

[81] Thomas M Babinec, Birgit J M Hausmann, Mughees Khan, Yinan Zhang, Jeronimo R Maze, Philip R Hemmer, and Marko Lončar, Nature Nanotechnology **5**, 195 (2010).

[82] B. J M Hausmann, J. T. Choy, T. M. Babinec, B. J. Shields, I. Bulu, M. D. Lukin, and Marko Lončar, Physica Status Solidi (A) Applications and Materials Science **209**, 1619 (2012).

[83] B. J. M. Hausmann, I. Bulu, V. Venkataraman, P. Deotare, and M. Lončar, Nature Photonics **8**, 369 (2014).

[84] Michael J. Burek, Yiwen Chu, Madelaine S. Z. Liddy, Parth Patel, Jake Rochman, Srujan Meesala, Wooyoung Hong, Qimin Quan, Mikhail D. Lukin, and Marko Lončar, Nature Communications **5**, 5718 (2014).

[85] Jeremy L. O'Brien, Akira Furusawa, and Jelena Vučković, Nature Photonics **3**, 687 (2009).

[86] Zhen-Sheng Yuan, Xiao-Hui Bao, Chao-Yang Lu, Jun Zhang, Cheng-Zhi Peng, and Jian-Wei Pan, Physics Reports **497**, 1 (2010).

[87] Vittorio Giovannetti and Seth Lloyd, Nature Photonics **5**, 222 (2011).

[88] LA Lugiato, A Gatti, and E Brambilla, Journal of Optics B: Quantum and Semiclassical Optics **4**, S176 (2002).

[89] Michael A Taylor, Jiri Janousek, Vincent Daria, Joachim Knittel, Boris Hage, Hans-a Bachor, and Warwick P Bowen, Nature Photonics **7**, 229 (2013).

[90] M. G. Raymer, Andrew H. Marcus, Julia R. Widom, and Dashiell L. P. Vitullo, The Journal of Physical Chemistry B **117**, 15559 (2013).

[91] T D Ladd, F Jelezko, R Laflamme, Y Nakamura, C Monroe, and J L O'Brien, Nature **464**, 45 (2010).

[92] Yanhua Shih, Reports on Progress in Physics **66**, 1009 (2003).

[93] Adrien Dousse, Jan Suffczynski, Alexios Beveratos, Olivier Krebs, Aristide Lemaitre, Isabelle Sagnes, Jacqueline Bloch, Paul Voisin, and Pascale Senellart, Nature **466**, 217 (2010).

[94] Q. Lin, F. Yaman, and Govind P. Agrawal, Physical Review A **75**, 023803 (2007).

[95] Andrew M. Lance, Thomas Symul, Warwick P. Bowen, Barry C. Sanders, and Ping Koy Lam, Physical Review Letters **92**, 177903 (2004).

[96] Mercedes Gimeno-Segovia, Pete Shadbolt, Daniel E. Browne, and Terry Rudolph, Physical Review Letters **115**, 020502 (2015).

[97] H Hubel, D R Hamel, A Fedrizzi, S Ramelow, K J Resch, and T Jennewein, Nature **466**, 601 (2010).

[98] L. K. Shalm, D. R. Hamel, Z. Yan, C. Simon, K. J. Resch, and T. Jennewein, Nature Physics **9**, 19 (2012).

[99] Deny R. Hamel, Lynden K. Shalm, Hannes Hübel, Aaron J. Miller, Francesco Marsili, Varun B. Verma, Richard P. Mirin, Sae Woo Nam, Kevin J. Resch, and Thomas Jennewein, Nature Photonics **8**, 801 (2014).

[100] M. Chekhova, O. Ivanova, V. Berardi, and A. Garuccio, Physical Review A **72**, 023818 (2005).

[101] Kamel Bencheikh, Fabien Gravier, Julien Douady, Ariel Levenson, and Benoît Boulanger, Comptes Rendus Physique **8**, 206 (2007).

[102] Christopher C Evans, Jonathan D B Bradley, Erwin A Marti-Panameno, and Eric Mazur, Optics Express **20**, 3118 (2012).

[103] M D Eisaman, J Fan, A Migdall, and S V Polyakov, Review of Scientific Instruments **82**, 71101 (2011).

[104] María Corona, Karina Garay-Palmett, and Alfred B. UâĂŹRen, Physical Review A **84**, 033823 (2011).

[105] S Richard, K Bencheikh, B Boulanger, and J A Levenson, Optics Letters **36**, 3000 (2011).

[106] Kyle Preston, Bradley Schmidt, and Michal Lipson, Optics Express **15**, 17283 (2007).

[107] I a Bufetov, M V Grekov, K M Golant, E M Dianov, and R R Khrapko, Optics Letters **22**, 1394 (1997).

[108] Zhaoming Zhu and Thomas Brown, Optics express **10**, 853 (2002).

[109] M Sheik-Bahae, DJ Hagan, and EW Van Stryland, Physical review letters **65**, 96 (1990).

[110] Timothy Lee, Neil G R Broderick, and Gilberto Brambilla, Journal of the Optical Society of America B **30**, 505 (2013).

[111] B. Corcoran, C. Monat, C. Grillet, D. J. Moss, B. J. Eggleton, T. P. White, L. O'Faolain, and T. F. Krauss, Nature Photonics **3**, 206 (2009).

[112] Stephan Krapick and Christine Silberhorn, arXiv:1506.07655 (2015).

[113] Nicolas Gisin and Rob Thew, Nat Photon **1**, 165 (2007).

[114] J. Brendel, N. Gisin, W. Tittel, and H. Zbinden, Physical Review Letters **82**, 2594 (1999).

[115] Irfan Ali-Khan, Curtis J. Broadbent, and John C. Howell, Physical Review Letters **98**, 1 (2007).

[116] Jianming Wen and Morton Rubin, Physical Review A **79**, 025802 (2009).

[117] Christopher C. Evans, Chengyu Liu, and Jin Suntivich, Optics Express **23**, 11160 (2015).

[118] Marin SoljaČiĆ and J D Joannopoulos, Nature Materials **3**, 211 (2004).

[119] Yuichi Watanabe, Masato Ohnishi, and Toshio Tsuchiya, Applied Physics Letters **66**, 3431 (1995).

[120] Susanta Kumar Das, Christoph Schwanke, Andreas Pfuch, Wolfgang Seeber, Martin Bock, Günter Steinmeyer, Thomas Elsaesser, and Ruediger Grunwald, Optics Express **19**, 16985 (2011).

[121] N a Borshchevskaya, K G Katamadze, S P Kulik, and M V Fedorov, Laser Physics Letters **12**, (2015).

[122] Matthew Borselli, Thomas Johnson, and Oskar Painter, Optics express **13**, 1515 (2005).

[123] Raji Shankar, Irfan Bulu, and Marko LoncÌŇar, Applied Physics Letters **102**, 051108 (2013).

[124] Markus Hayrinen, Matthieu Roussey, Vishal Gandhi, Petri Stenberg, Antti Saynatjoki, Lasse Karvonen, Markku Kuittinen, and Seppo Honkanen, Journal of Lightwave Technology **32**, 208 (2014).

[125] M J Stevens, B Baek, E A Dauler, A J Kerman, R J Molnar, S A Hamilton, K K Berggren, R P Mirin, and S W Nam, Optics Express **18**, 1430 (2010).

[126] D Rosenberg, A J Kerman, R J Molnar, and E A Dauler, Optics Express **21**, 1440 (2013).

[127] Joseph Nuss, Martin; Orenstein, in *Millimeter and Submillimeter Wave Spectroscopy of Solids*, edited by George Grüner (Springer Berlin Heidelberg, ADDRESS, 1998), Vol. 74, pp. 7–50.

[128] L Duvillaret, F Garet, and J L Coutaz, Applied optics **38**, 409 (1999).

[129] T D Dorney, R G Baraniuk, and D M Mittleman, Journal of the Optical Society of America. A, Optics, image science, and vision **18**, 1562 (2001).

[130] Seizi Nishizawa, Kiyomi Sakai, Masanoi Hangyo, Takeschi Nagashima, Mitsuo Wada Takeda, Keisuke Tominaga, Asako Oka, Koichiro Tanaka, and Osamu Morikawa, in *Terahertz Optoelectronics*, edited by Kiyomi Sakai (Springer Berlin Heidelberg, ADDRESS, 2005), Vol. 97, pp. 203–271.

[131] Ari Sihvola and Reena Sharma, Microwave and Optical Technology Letters **22**, 229 (1999).

[132] Pierre Mallet, C. A. Guérin, and Anne Sentenac, Physical Review B - Condensed Matter and Materials Physics **72**, 1 (2005).